

Experimental Realization of a Simple Entangling Optical Gate for Quantum Computation

Diplomarbeit zur Erlangung des Grades eines
"Magister der Naturwissenschaften"

eingereicht von

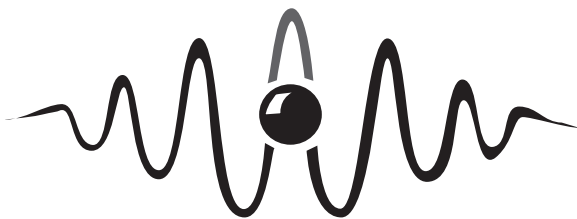
Robert Prevedel

im November 2005

durchgeführt bei

o. Prof. Dr. Anton Zeilinger

Gruppe Quantum Experiments and the Foundations of Physics
Institut für Experimentalphysik
Universität Wien



Wer einen Pfau braucht, muss eine Reise nach Indien auf sich nehmen.

Persisches Sprichwort

Abstract

We present and demonstrate an all-optical, non-deterministic **CSIGN**-gate for quantum computation. The **CSIGN**-gate is capable of entangling previously unentangled qubits and therefore represents an elementary operation relevant for universal quantum computing. It can also be employed for the generation of novel multi-particle entangled states, among them the so-called *cluster states*. The operation of the quantum gate is completely characterized by performing quantum state and process tomography. Reconstructing the process matrix of the **CSIGN**-gate, we find an average gate fidelity of $F_{avg} = 0.84 \pm 0.1$. The realized optical **CSIGN**-circuit is based on the two-photon scheme of References [14, 15], and since it requires only a *single* optical mode-matching condition, its construction is drastically facilitated compared to previous schemes. This circuit indeed presents the simplest entangling optical gate realized to date. This thesis is written in a fully self-contained manner, introducing and establishing the required theoretical background and giving a full description of the experimental setup and procedure as well as a thorough discussion of the results and occurring problems. We propose the extension of the above scheme to generate a genuine 3-photon cluster state, which is equivalent to a Greenberger-Horne-Zeilinger-state (GHZ-state) [16], and give a short outlook on future experiments. In additional experiments the effects of temporal mode-mismatch has been studied. This was achieved with an adapted quantum teleportation experiment, showing that the fidelity of such a quantum communication protocol declines in a Gaussian fashion as a function of the temporal mode-mismatch. A simple theoretical model is developed that explains this behaviour, consistent with the experimental data.

Contents

Abstract	i
Preface	1
1. Introduction	3
1.1. Quantum Mechanics	3
1.1.1. The Qubit	3
1.1.2. Poincaré-Sphere	4
1.1.3. Measurements	5
1.1.4. Multiple-Qubits and Entanglement	5
1.2. Linear Optics Gates	8
1.2.1. Single-Qubit Gates	8
1.2.2. Multiple-Qubit Gates	10
1.3. Quantum Computation	12
1.3.1. Universal Quantum Gates	12
1.3.2. Algorithms for Quantum Computers	13
1.3.3. Quantum Computing with Cluster States	14
2. Basics of the Experiment	17
2.1. Spontaneous Parametric Down-Conversion	17
2.1.1. A Source for Entangled Photons	19
2.1.2. Gaussian Beam Propagation	20
2.2. Linear Optics Devices	23
2.2.1. Beamsplitter	23
2.2.2. Half- and Quarter-waveplates	25
2.3. Creation of a 3-Photon Cluster State	26
2.3.1. The Simplified CSIGN-Gate	27
2.3.2. Coherent State Input	28
2.4. Gate-Tomography	30
2.4.1. State-Tomography	30
2.4.2. Process-Tomography	32

3. Description of the Setup	35
3.1. Lasers	35
3.2. Optical Setup	36
3.3. Detectors	37
3.4. Coincidence Logic	37
4. Experimental Procedure	39
4.1. Pre-experimental Alignment	39
4.1.1. Waveplate Calibration	40
4.1.2. PPBS-Characterization	41
4.1.3. HOM-Dip	41
4.2. Quantum Process Tomography of the Gate	43
5. Results & Discussion	45
5.1. CNOT Truth Table	45
5.2. Single-Qubit Tomography	48
5.3. Two-Qubit State Tomography	49
5.4. Process Tomography	51
5.5. Discussion	53
6. Problems & Possible Solutions	57
6.1. Adding in that 3 rd Photon	57
6.2. Coincidence Rate Improvement	58
7. Outlook	61
7.1. 3-Photon CSIGN-gate	61
7.1.1. Test of Svetlichny's Inequality	62
7.2. 4-Photon Source	62
7.2.1. Implementation of Shor's Algorithm	63
7.2.2. Quantum Control	63
8. Further Investigation	65
8.1. Motivation	65
8.2. Quantum Teleportation	66
8.2.1. The Teleportation Protocol	67
8.2.2. Experimental Bell State Analysis	68
9. The Teleportation Setup	71
9.1. Laser	71
9.2. Entanglement Source	72
9.3. More Complete Bell-State Analyzer	72
9.3.1. Prerequisites for Quantum Interference	73
9.4. Detection and Coincidence Logic	75

10. The Mode-Mismatch Experiment	77
10.1. Experimental Procedure	77
10.1.1. Optimizing the Entanglement Source	77
10.1.2. HOM-Dip	79
10.2. Results	80
10.3. Discussion	83
10.3.1. A Simple Theoretical Model	84
11. Conclusion	87
A. Published Work of this Thesis	89
Bibliography	99
Acknowledgements	101

Preface

Whenever we talk about Quantum Computation or, in a more general form, of Quantum Information, we are speaking of information processing tasks that can (only) be accomplished using quantum mechanical systems [1, 2].

Much of the effort in quantum information is directed toward the experimental realization of a quantum computer. It has been shown that a quantum computer can perform certain tasks, like factoring large numbers and searching databases, much more efficiently than a regular “classical” computer [4, 5].

It is very interesting and well worth noting, that a quantum system of 500 qubits already requires 2^{500} amplitudes to fully describe its quantum state. This number is larger than the estimated number of atoms in the universe and this enormous potential computational power is well worth harvesting!

M.A. Nielsen and I.L. Chuang

Quantum information certainly offers plenty of challenges to physicists and there exist many different experimental approaches. Photons are very good contenders for qubits to realize such quantum computing systems, as they can be produced and manipulated very easily and have low decoherence, since they tend not to interact with the environment. However, photons also have a very small interaction cross-section and since photon-photon interaction is required for two- or multiple-qubit gates, they have long been thought to be inappropriate for quantum computation. But in 2001, Knill, LaFlamme and Milburn (KLM) introduced a scheme [6] for optical quantum computation which depends on measurement-induced non-linearities. The KLM scheme is suitable and, furthermore, scalable for efficient quantum computation. In the subsequent years, the scheme has been improved and simplified [7, 8] and in the last few years a number of two-qubit gates have been demonstrated experimentally [9, 10, 11].

A very elegant and beautifully alternate model to the KLM scheme was suggested by Raussendorf and Briegel [12] in 2001, which is a “measurement based” computation scheme that is independent of any specific physical realization. It is based on so-called *cluster states*, which are highly entangled networks of qubits, and the computation is performed by a sequence of single qubit measurements, where the order and choices of measurements determine the algorithm that is computed. The outcomes of the single measurements can be classically fedforward, resulting in *deterministic* quantum computation, in contrast to the probabilistic KLM scheme. All in all, cluster states are

very promising for future implementations of quantum computers and the creation of such a cluster state is also the main goal of the experiment which is investigated in this thesis. To effectively create such a cluster state, one has to entangle individual qubits by applying **CSIGN**-gates between them. A **CSIGN**-gate introduces a controlled phase shift between individual qubits, such that $|i\rangle|j\rangle \rightarrow (-1)^{ij}|i\rangle|j\rangle$, with $(i, j \in \{0, 1\})$. This two-qubit gate together with single-qubit rotations, is universal for quantum computation, i.e. any arbitrary unitary operation can be performed by these gates alone. It is therefore of utmost importance in the current research field of quantum computation to realize such gates and to use them for the creation of cluster states. Although cluster states have been demonstrated experimentally before [13], this, if successful, would be the first generation of a genuine cluster state of previously unentangled photons. The scheme which we tried to realize was first suggested independently by T.C. Ralph *et al.* [14] as well as by Hofmann and Takeuchi [15], and can in principle be easily extended to create a N-photon cluster state. Even though the experiment to create these cluster states is still under way, the basic component for the generation of the cluster state, the **CSIGN**-gate, has been realized and characterized using quantum state and process tomography. This thesis mainly focuses on this recent results but at the same time gives an outlook and proper explanation of the generation of a 3-photon cluster state, which is equivalent to a GHZ-state [16].

Since it turns out that mode-mismatch is the prime delimiter to the performance of the gate, further investigation with respect to temporal mode-mismatch has been undertaken. Employing a quantum teleportation configuration [52], we study the effects of temporal mode mismatch on the fidelity of the teleportation process and give a proper explanation in form of a simple theoretical model. The achievement of perfect mode-matching presents a major challenge in almost every “real world” application of quantum communication (QC) schemes, such as quantum dense coding [50], quantum teleportation [45], and a quantum repeater [47, 46, 49], which is at the heart of long distance QC.

The experimental work presented in this diploma thesis was performed at two universities: In the Quantum Optics Group of Prof. Dr. Anton Zeilinger at the University of Vienna, Austria, (Chapters 8 to 10) and at the University of Queensland, Australia, in the Quantum Technology Laboratory of Prof. Dr. Andrew White (Chapters 3 to 7).

This thesis is structured as follows: I will first of all briefly examine some key ideas underlying quantum computation and quantum information in Chapter 1, before theory concerning the experiment is discussed in more detail in Chapter 2. A (technical) description of the setup and of the experimental procedure follows (Chapters 3 and 4) before I present and discuss the results in Chapter 5. Occurring problems and possible solutions are outlined in Chapter 6. A short outlook for future experiments is given and their realization briefly discussed (Chapter 7) before further investigation on mode-mismatch effects is presented in Chapter 8. This experiment employs quantum teleportation and after a short theoretical introduction into quantum teleportation, I will proceed to the description of the setup (Chapter 9) and present and discuss the results in the concluding Chapter 10.

1. Introduction

The fundamental concept of a classical computer is the *bit*. Quantum information and especially quantum computation rely on a similar concept, the quantum bit, or *qubit*. In this section I will give a short introduction in the properties of qubits, their representation on the so-called Bloch- or Poincaré-Sphere and explain the - according to Schrödinger [3] - most interesting and puzzling property in quantum information, *entanglement*.

1.1. Quantum Mechanics

1.1.1. The Qubit

Just as a classical bit has a state, either 0 or 1, a qubit also has a state, which can be thought of as a vector in a two-dimensional *Hilbert*-space and will be denoted as $|0\rangle$ and $|1\rangle$ from now on. The main and important difference between bits and qubits is that the latter can also be in a linear combination of states, i.e. a coherent *superposition*:

$$|\Psi\rangle = \alpha|0\rangle + \beta|1\rangle, \quad (1.1)$$

where α and β are complex numbers (often called *amplitudes*). The states $|0\rangle$ and $|1\rangle$ are also known as *computational basis states* and form an orthonormal basis for this vector space. In contrast to a classical bit the qubit can exist in a continuum of states between $|0\rangle$ and $|1\rangle$, until we observe, i.e. measure it. Whenever we measure a qubit we get a probabilistic result, either '0' or '1', with probability $|\alpha|^2$ and $|\beta|^2$, respectively. Since the

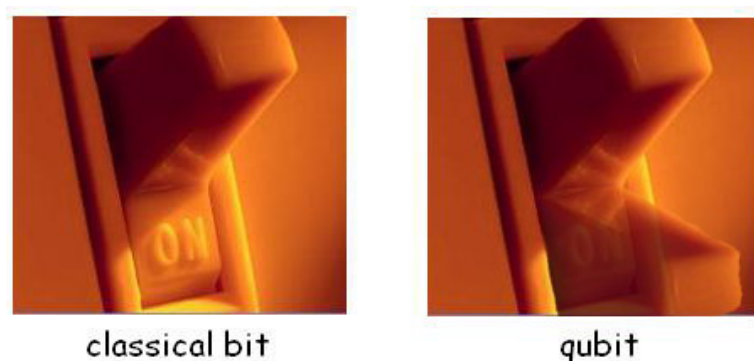


Figure 1.1.: The difference between classical bits and qubits. The classical bit is always in a defined state while qubits can also exist in a superposition of states.

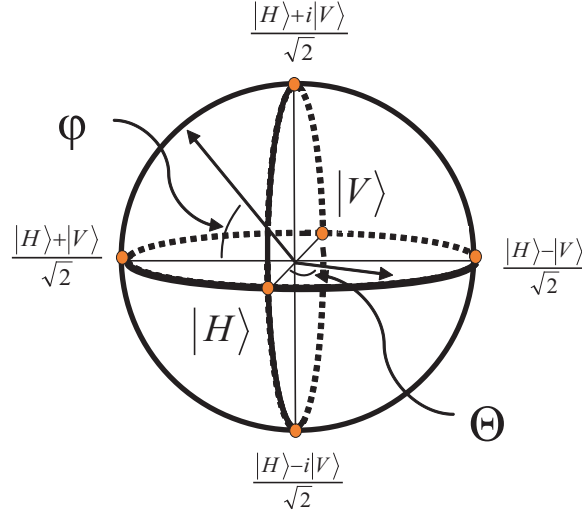


Figure 1.2.: Poincaré-Sphere representation of a single qubit. $|R\rangle$ and $|L\rangle$ lie on the poles of the sphere while $|H\rangle, |V\rangle$ and $|+\rangle$ and $|-\rangle$ are located on the equatorial plane, all those basis states being separated by $\frac{\pi}{2}$. θ represents an angle on the equatorial plane while φ is measured off the equator as indicated.

probabilities must sum up to one, i.e. $\langle\Psi|\Psi\rangle = 1$, a natural condition implies $|\alpha|^2 + |\beta|^2 = 1$ (normalization condition).

Qubits can be realized experimentally in many different physical quantum systems, e.g. as the alignment of the nuclear spin in a uniform magnetic field or as two different energy levels of a single atom or ion (‘ground’ and ‘excited’ state). In our experiment we realize the qubit as two different polarizations of a single photon (e.g. horizontal and vertical polarization, $|H\rangle$ and $|V\rangle$ for $|0\rangle$ and $|1\rangle$, respectively), since photons can easily be controlled and their states manipulated with rather simple linear optical devices.

1.1.2. Poincaré-Sphere

One very useful picture when thinking about qubits is the geometrical representation of polarization states on the so-called *Poincaré-Sphere*. Since $|\alpha|^2 + |\beta|^2 = 1$, one can rewrite the state in Eq. 1.1 as

$$|\Psi\rangle = \cos\frac{\theta}{2}|0\rangle + e^{i\varphi}\sin\frac{\theta}{2}|1\rangle, \quad (1.2)$$

where the angles θ and φ define a point on the three-dimensional unit sphere shown in Fig. 1.2. R (L) denotes right (left) circular polarized light $R(L) = \frac{1}{\sqrt{2}}(|H\rangle \pm i|V\rangle)$, while diagonal polarized light $|D\rangle$ ($|A\rangle$) is the coherent superposition of $|H\rangle$ and $|V\rangle$, $D(A) = \frac{1}{\sqrt{2}}(|H\rangle \pm |V\rangle)$ and also lies on the equatorial plane of the sphere. $|D\rangle$ and $|A\rangle$ are also often denoted as $|+\rangle$ and $|-\rangle$. Pure states lie on the surface of the sphere while mixed states are found inside the sphere. As we will see later on, many operations on single qubits can be neatly described within this picture.

1.1.3. Measurements

Measurements play a significant role in quantum mechanics and especially in quantum computation. It is usually described as an interaction of the quantum system with a (classical) measurement apparatus, and is also referred to as *projective* measurement. Such a projective measurement is characterized by an *observable*, M , which is a Hermitian operator in Hilbert space, and has a spectral decomposition,

$$M = \sum_m m P_m, \quad (1.3)$$

where P_m is the projector onto the eigenspace of M with eigenvalue m . The only possible results of the measurement are the eigenvalues m of the observable. The probability of obtaining result m upon measuring the state $|\Psi\rangle$ is given by

$$p(m) = \langle \Psi | P_m | \Psi \rangle, \quad (1.4)$$

and the state of the quantum system is projected onto the final state

$$|\Psi\rangle_f = \frac{P_m |\Psi\rangle}{\sqrt{p(m)}}. \quad (1.5)$$

Suppose we want to measure a qubit as given in Eq. 1.1 in the computational basis. If we measure a single qubit, then there are two possible outcomes, defined by two measurement operators, $M_0 = |0\rangle\langle 0|$ and $M_1 = |1\rangle\langle 1|$. Then, according to Eq. 1.4, the probability of obtaining measurement outcome 0 is given by

$$p(0) = \langle \Psi | M_0 | \Psi \rangle = |\alpha|^2, \quad (1.6)$$

i.e., the absolute amplitude squared. Similarly, the probability for outcome 1 is $p(1) = |\beta|^2$.

Another important mathematical tool associated with quantum measurements is the *POVM formalism*, which is very well adapted to the analysis of measurements. It basically states that one needs a sufficient (complete) set of operators P_m to determine all the different possibilities of measurement outcomes¹.

1.1.4. Multiple-Qubits and Entanglement

For two classical bits there are four possible states, 00, 01, 10 and 11, but a pair of qubits can also exist in a superposition of this states, therefore spanning a 4-dimensional Hilbert space. One important class of two-qubit states is the so-called *EPR pair* or *Bell-state*,

$$|\Phi^+\rangle = \frac{1}{\sqrt{2}}(|00\rangle + |11\rangle) \quad (1.7)$$

Entangled states play a crucial role in quantum computation and quantum information and are therefore of utmost importance. One remarkable feature of such states is that they

¹The interested reader is referred to [2] for a complete introduction into the POVM formalism.

cannot be built as single and separable qubit states $|a\rangle$ and $|b\rangle$ such that $|\Phi\rangle = |a\rangle|b\rangle$. Thus, they cannot be written as a product of states of their component systems, which is a very crucial property of entangled states. When measuring the first qubit, one obtains the result 0 (1) with probability 1/2 each, leaving the state $|00\rangle$ ($|11\rangle$). In either case, the measurement of the second qubit will yield the same result as the measurement of the first qubit. In other words, the measurement outcomes are *correlated*. Einstein, Podolsky and Rosen first pointed out these strange properties of such states [20] and they have been named *Bell-States* in honour of John Bell, who showed that correlations in such entangled states are stronger than could possibly exist between classical systems [21]. For a two-qubit system there are four distinct entangled states, the Bell-States,

$$\begin{aligned} |\Phi^\pm\rangle &= \frac{1}{\sqrt{2}}(|00\rangle \pm |11\rangle) \\ |\Psi^\pm\rangle &= \frac{1}{\sqrt{2}}(|01\rangle \pm |10\rangle), \end{aligned} \tag{1.8}$$

which form an orthonormal basis for the two-qubit state space, and can therefore be distinguished by appropriate quantum measurements.

But let us for now return to our quantum states, the most important resource in quantum computation, and try to quantify this term more precisely.

Purity

Before we can decide whether a quantum state is pure or mixed, we have to accustom ourselves with the *density operator* or *density matrix* formalism, a convenient way for describing quantum systems whose state is not completely known.

Suppose we have a quantum system that is in a superposition of states $|\Psi\rangle_i$ with respective probabilities p_i . Then the density operator for this system is defined by

$$\rho \equiv \sum_i p_i |\Psi\rangle_i \langle\Psi|_i. \tag{1.9}$$

It is worth noting that a density operator ρ is always a non-negative operator and always has trace equal to one.

A quantum system whose state $|\Psi\rangle$ is exactly known is said to be in a *pure state*, in which case the density operator is simply $\rho = |\Psi\rangle\langle\Psi|$. Otherwise it is in a *mixed state*. A simple criterion for determining whether a state is mixed or pure is to look at the trace of the corresponding density operator. A pure state satisfies

$$\text{tr}(\rho^2) = 1 \tag{1.10}$$

while for a mixed state $\text{tr}(\rho^2) < 1$.

Fidelity

The *fidelity* is a useful measure of *distance* between two quantum states, i.e. in which degree two states overlap and are therefore the same. The fidelity between a pure state $|\Psi\rangle\langle\Psi|$ and an arbitrary state ρ can be written as

$$\mathcal{F} = \langle\Psi|\rho|\Psi\rangle, \quad (1.11)$$

and is therefore equal to the overlap between $|\Psi\rangle\langle\Psi|$ and ρ . Another definition for the fidelity between two density matrices can be found in Section 5.4.

Tangle

The *tangle* [17] is a measure for the “amount” of entanglement between two entangled states and is straightforwardly only defined for a pair of qubits.

If ρ_{AB} is the density operator of two qubits A and B , then the tangle τ_{AB} of the density matrix ρ_{AB} is defined as

$$\tau_{AB} = [\max\{\lambda_1 - \lambda_2 - \lambda_3 - \lambda_4, 0\}]^2, \quad (1.12)$$

where λ_{1-4} are, in decreasing order, the square roots of the eigenvalues of the product $\rho_{AB} \tilde{\rho}_{AB}$.² A tangle of $\tau=0$ corresponds to an unentangled state, while $\tau=1$ corresponds to a maximally entangled state, and the entanglement of formation³ is a monotonically increasing function of τ . For the special case in which the state of AB is pure, the matrix $\rho_{AB} \tilde{\rho}_{AB}$ has only one non-zero eigenvalue, and one can show that $\tau_{AB} = 4 \det \rho_A$, where ρ_A is the reduced density matrix of qubit A , i.e., the trace of ρ_{AB} over qubit B .

Another often used term when speaking about the degree of entanglement is the “concurrency”, which is simply the square root of the tangle [18].

Entropy

In quantum mechanics, the entropy is a fundamental measure of information and therefore a key concept in quantum information theory. It is a measure for the uncertainty of a quantum state, i.e. its density operators. Von Neumann defined the entropy of a quantum state ρ by

$$S(\rho) \equiv -\text{tr}(\rho \log \rho), \quad (1.13)$$

where the logarithm is taken to the base two. If λ_x are eigenvalues of ρ then this definition can be rewritten as

$$S(\rho) = -\sum_x \lambda_x \log \lambda_x. \quad (1.14)$$

² $\tilde{\rho}_{AB}$ is defined by $\tilde{\rho}_{AB} = (\sigma_y \otimes \sigma_y) \rho_{AB}^* (\sigma_y \otimes \sigma_y)$, where the asterisk denotes complex conjugation and $\sigma_y = \begin{pmatrix} 0 & -i \\ i & 0 \end{pmatrix}$ is one of the Pauli matrices (Section 1.2.1).

³The entanglement of formation is given by $E = h(\frac{1}{2} + \frac{1}{2}\sqrt{1-\tau})$, where h is the binary entropy function $h(x) = -x \log x - (1-x) \log(1-x)$.

The entropy is always non-negative and is zero if and only if the state is pure and is at most $\log d$ in a d -dimensional Hilbert space if the the system is completely mixed. If a composite system AB is in a pure state then $S(A) = S(B)$. In this case the entropy of the entanglement ranges from 0 for completely separable states to 1 for maximally entangled states, although this definition should be taken with care.

If a measurement is performed on the system, then the state after the measurement can be written as

$$\rho' = \sum_i P_i \rho P_i \quad (1.15)$$

and the entropy is never decreased by this procedure and remains constant only if the state is not changed by the measurement. Since most measurements are projective, i.e. they effectively change the state of the system, in general $S(\rho') \geq S(\rho)$.

The “*linear entropy*” is simpler to calculate and is related to the von Neumann entropy. The linear entropy for a two-qubit system (4-dim. density operator) is defined by

$$S(\rho) = \frac{4}{3} (1 - \text{tr}(\rho^2)). \quad (1.16)$$

For a pure state $S = 0$ while for a maximally mixed state $S = 1$.

1.2. Linear Optics Gates

In order to perform quantum computation, we need the ability to fully control and manipulate single- and multiple-qubits, i.e. rotate them around specific axes, put them in superposition and effectively entangle two qubits. Fortunately, there exist a number of linear optical elements acting like computational “gates” and capable of performing these operations, as we will see in this section.

1.2.1. Single-Qubit Gates

Quantum gates acting on single qubits can be described by 2×2 matrices, with the constraint that the gate or matrix be *unitary*, therefore satisfying the normalization condition before and after the gate (i.e. particle conservation).

Hadamard Gate

The *Hadamard*-gate (denoted H) is one of the most useful single-qubit gates, since it turns $|0\rangle$ into $(|0\rangle + |1\rangle)/\sqrt{2}$ and $|1\rangle$ into $(|0\rangle - |1\rangle)/\sqrt{2}$, therefore creating superposition.

$$H \equiv \frac{1}{\sqrt{2}} \begin{pmatrix} 1 & 1 \\ 1 & -1 \end{pmatrix} \quad (1.17)$$

This gate is sometimes described to act like a “square-root of NOT” gate, because it performs “half” of the NOT operation, i.e it takes $|0\rangle$ to $(|0\rangle + |1\rangle)/\sqrt{2}$, which is “halfway”

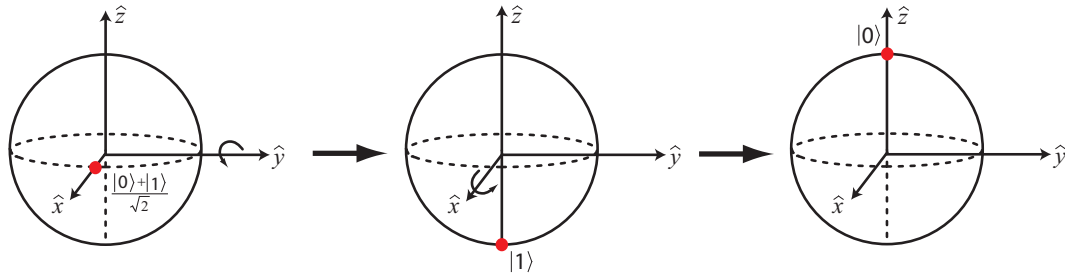


Figure 1.3.: Visualization of the Hadamard gate on the Poincaré-Sphere, acting on the input state $(|0\rangle + |1\rangle)/\sqrt{2}$.

in between $|0\rangle$ and $|1\rangle$. However, this description is misleading, since simple algebra shows that $H^2 = \mathbb{I}$, thus applying H twice to a state is just the identity operation. When visualizing the Hadamard operation on the Poincaré-sphere, it turns out that it is just a rotation of the sphere about the \hat{y} -axis by 90° , followed by a rotation about the \hat{x} -axis by 180° , as illustrated in Fig. 1.3.

X-,Y-,Z-Gates

Another important set of gates are the X -, Y -, Z -gates, corresponding to the Pauli matrices

$$X \equiv \begin{pmatrix} 0 & 1 \\ 1 & 0 \end{pmatrix}; \quad Y \equiv \begin{pmatrix} 0 & -i \\ i & 0 \end{pmatrix}; \quad Z \equiv \begin{pmatrix} 1 & 0 \\ 0 & -1 \end{pmatrix}. \quad (1.18)$$

The X -gate, for example, acts like a quantum NOT-gate, performing a bit flip on the input state $\alpha|0\rangle + \beta|1\rangle \rightarrow \alpha|1\rangle + \beta|0\rangle$, so that the roles of $|0\rangle$ and $|1\rangle$ are interchanged. The Z -gate, on the other hand, performs a sign flip, since it does nothing to $|0\rangle$, but flips the sign of $|1\rangle$ to give $-|1\rangle$, therefore $\alpha|0\rangle + \beta|1\rangle \rightarrow \alpha|0\rangle - \beta|1\rangle$. And last but not least, a Hadamard-gate can be constructed out of X - and Z -gates, such that $H = (X + Z)/\sqrt{2}$.

Pauli matrices, when exponentiated, give rise to *rotation operators* about the \hat{x} -, \hat{y} -, \hat{z} -axes, and can be defined by

$$R_x(\theta) \equiv \exp^{-i\theta X/2} = \mathbb{I} \cos \frac{\theta}{2} - iX \sin \frac{\theta}{2} = \begin{pmatrix} \cos \frac{\theta}{2} & -i \sin \frac{\theta}{2} \\ -i \sin \frac{\theta}{2} & \cos \frac{\theta}{2} \end{pmatrix}, \quad (1.19)$$

and similarly for the other rotation operators $R_y(\Theta)$, $R_z(\Theta)$.

For the sake of completeness, other frequently used single-qubit gates are the phase gate (denoted S) and the $\pi/8$ gate (denoted T), whose corresponding matrices read as

$$S = \begin{pmatrix} 1 & 0 \\ 0 & i \end{pmatrix}; \quad T = \begin{pmatrix} 1 & 0 \\ 0 & e^{i\pi/4} \end{pmatrix}. \quad (1.20)$$

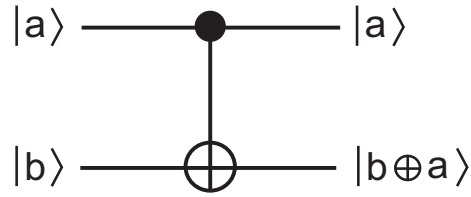


Figure 1.4.: Circuit representation of the controlled-NOT-gate.

1.2.2. Multiple-Qubit Gates

Multiple-qubit gates are very essential for quantum computational tasks, since they allow individual qubits to interact with one another, conditional on the state of one or more qubit(s). We will see in this section, that two-qubit gates can be employed to create entanglement between two previously unentangled qubits, and since entanglement is such an important resource in quantum information, such gates deserve appropriate attention.

Controlled-NOT Gate

One of the typical multi-qubit quantum logic gates is the *controlled-NOT* or **CNOT**-gate. It consists of two input qubits, known as the *control* and *target qubit*, respectively. A circuit representation is shown in Fig. 1.4. The top line represents the control qubit, while the bottom line denotes the target qubit. The gate itself works as follows. If the control qubit is set to 0, then the target qubit is left alone. If the control qubit is set to 1, then the target qubit is flipped, thus resulting in the following, so-called truth table:

$$\begin{aligned} |00\rangle &\rightarrow |00\rangle \\ |01\rangle &\rightarrow |01\rangle \\ |10\rangle &\rightarrow |11\rangle \\ |11\rangle &\rightarrow |10\rangle \end{aligned} \tag{1.21}$$

Another way of summarizing the action of the gate is $|a, b\rangle \rightarrow |a, b \oplus a\rangle$, where \oplus denotes addition modulo two, as can be seen in the circuit representation. Yet it is also possible to give a matrix representation of the **CNOT**, with respect to the amplitudes $|00\rangle$, $|01\rangle$, $|10\rangle$ and $|11\rangle$, in that order.

$$CNOT = \begin{pmatrix} 1 & 0 & 0 & 0 \\ 0 & 1 & 0 & 0 \\ 0 & 0 & 0 & 1 \\ 0 & 0 & 1 & 0 \end{pmatrix} \tag{1.22}$$

As we have shortly mentioned before, a **CNOT**-gate can be employed to create entanglement between two initially independent particles, as we will now see. Suppose we have the control qubit in a superposition state, i.e. $|+\rangle = \frac{1}{\sqrt{2}}(|0\rangle + |1\rangle)$, while the target qubit is in

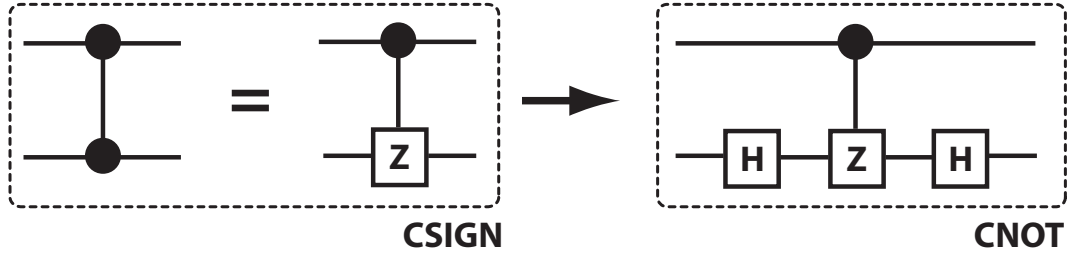


Figure 1.5.: Circuit representation of the controlled-SIGN-gate. With additional Hadamard gates acting on the target qubit, the whole circuit is equal to the CNOT-gate.

the state $|0\rangle$. According to the CNOT truth table of Eq. 1.21, we end up with the state

$$|\Phi^+\rangle = \frac{1}{\sqrt{2}}(|00\rangle + |11\rangle), \quad (1.23)$$

which is one of the maximally entangled Bell-states, as in Eq. 1.8. Thus, such a gate can effectively entangle, but also disentangle any two qubits. It is therefore of utmost importance in quantum computation to experimentally realize such a gate, as has been achieved by various research groups [9, 10, 24].

Controlled-SIGN Gate

Further inspection reveals that the CNOT-gate is not the only two-qubit gate capable of entangling two particles. Another very useful gate in quantum computations turns out to be the *controlled-SIGN*-gate, or CSIGN-gate for short. The gate's action in the computational basis is specified by the following unitary matrix

$$CSIGN = \begin{pmatrix} 1 & 0 & 0 & 0 \\ 0 & 1 & 0 & 0 \\ 0 & 0 & 1 & 0 \\ 0 & 0 & 0 & -1 \end{pmatrix}, \quad (1.24)$$

it therefore changes the sign on the $|11\rangle$ element to $-|11\rangle$. It turns out that applying additional Hadamard gates acting on the target qubit before and after the CSIGN-gate, results in the same action as the CNOT (see Fig. 1.5). Therefore we can write

$$\begin{aligned} (I \otimes H) \cdot CSIGN \cdot (I \otimes H) &= \begin{pmatrix} 1 & 1 & 0 & 0 \\ 1 & -1 & 0 & 0 \\ 0 & 0 & 1 & 1 \\ 0 & 0 & 1 & -1 \end{pmatrix} \cdot \begin{pmatrix} 1 & 0 & 0 & 0 \\ 0 & 1 & 0 & 0 \\ 0 & 0 & 1 & 0 \\ 0 & 0 & 0 & -1 \end{pmatrix} \cdot \begin{pmatrix} 1 & 1 & 0 & 0 \\ 1 & -1 & 0 & 0 \\ 0 & 0 & 1 & 1 \\ 0 & 0 & 1 & -1 \end{pmatrix} = \\ &= \begin{pmatrix} 1 & 0 & 0 & 0 \\ 0 & 1 & 0 & 0 \\ 0 & 0 & 0 & 1 \\ 0 & 0 & 1 & 0 \end{pmatrix} = CNOT \end{aligned} \quad (1.25)$$

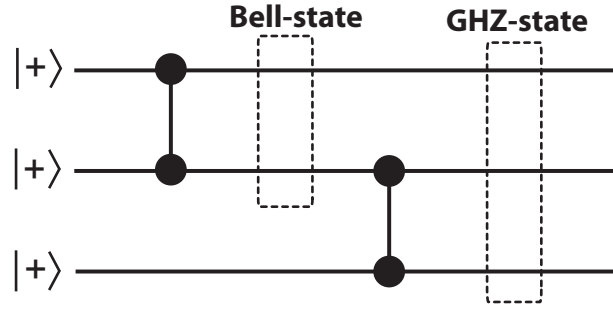


Figure 1.6.: Circuit representation to generate Bell- and GHZ-states by employing CSIGN-gates. Note that, initially, the qubits are required to be in the superposition state $|+\rangle$ (see Eq. 1.26 and 1.27).

and a circuit representation can be seen in Fig. 1.5. So, in order to create entanglement between two qubits, both the control and the target qubit have to be in a superposition state $|+\rangle$,

$$|+\rangle \xrightarrow{\text{CSIGN}} |+\rangle \longrightarrow \frac{1}{\sqrt{2}}(|00\rangle + |11\rangle) = |\Phi^+\rangle. \quad (1.26)$$

Similar, if we connect three qubits, again all in the superposition state, then we end up with an entangled three-particle GHZ-state [16], which is also a so-called 3-photon cluster state (see Fig. 1.6).

$$|+\rangle \xrightarrow{\text{CSIGN}} |+\rangle \xrightarrow{\text{CSIGN}} |+\rangle \longrightarrow \frac{1}{\sqrt{2}}(|000\rangle + |111\rangle) = |\Psi\rangle_{GHZ} \quad (1.27)$$

If four (or more qubits) are entangled in the same manner as described above employing concatenated CSIGN-gates, the resulting entangled state is the first cluster state to exhibit a different kind of entanglement as it can not be written as a four-particle generalization of the GHZ-state. Even further differences arise for the persistency of the entanglement, i.e. reminders of such a cluster state can still be entangled after loss of particles or projective measurements [12]. All in all, cluster states turn out to be a very efficient resource for quantum computational tasks as will be discussed in the following section.

1.3. Quantum Computation

Since we have made ourselves familiar with the basic “rules” and “ingredients” of quantum information, and by now have explained the most important and fundamental gates of the quantum circuit model, we can now proceed a step further and investigate the power and possibilities of quantum computation.

1.3.1. Universal Quantum Gates

In the theory of quantum computational networks, a gate is considered to be universal if instances of it are the only computational components required to build a universal

quantum computer. A set of gates is said to be universal, if any arbitrary unitary operation can be performed by these gates alone.

It turns out that in theory, any unitary operation can be expressed exactly using single qubit and CNOT-gates. Single-qubit gates on the other hand can be constructed out of Hadamard, phase and $\pi/8$ gates. These four gates are therefore universal for quantum computation and the interested reader is referred to Chapter 4.5 of Ref. [2] for a mathematical proof.

1.3.2. Algorithms for Quantum Computers

The quantum computer is a very powerful application of the laws of quantum physics. It is far more efficient at searching databases, factoring numbers and performing calculations than any classical computer [4, 5].

Many quantum algorithms rely on a fundamental feature called *quantum parallelism*, and in fact this is one of the main reasons why quantum computers so significantly outperform their classical counterparts. Quantum parallelism allows, e.g. to evaluate a function $f(x)$ for many different values of x at the same time. By exploiting the feature of superposition, a single circuit can be employed to evaluate the function, unlike in the classical case, where multiple circuits have to be built. As one can probably guess by now, the Hadamard operation plays an important role in most of these quantum algorithms, which shall be introduced briefly in the following.

Grover's Search Algorithm

Grover's algorithm [4] is very important, both from a practical point of view, since it allows fast database searching and is therefore critical for solving difficult problems, as well as from a fundamental standpoint, since it is proven to be more efficient than the best known classical algorithm. The goal of the algorithm is to identify one out of N elements of an unsorted database. Classically, on average, one has to search (randomly) $N/2$ times, while quantum parallelism boosts the probability of finding the desired element in only $O(\sqrt{N})$ trials. In the case of $N=4$, the speedup is even more drastic, as Grover's algorithm needs only one trial, whereas classically three evaluations are needed in the worst case, and 2.25 on average [13].

Shor's Algorithm

In 1994, Peter Shor demonstrated that one of the most important problems, namely finding the prime factors of an integer, can be solved on a quantum computer, providing a spectacular speedup over classical, inefficient algorithms [5]. This kind of algorithm has not yet been implemented with linear optics⁴, and since most of today's cryptography

⁴However, Shor's algorithm has been successfully implemented in a nuclear magnetic resonance experiment, see Ref. [23].

relies on the technique of encoding messages and data with the help of prime factors of large integers, it is well worth mentioning.

Deutsch-Jozsa Algorithm

Although the Deutsch-Jozsa algorithm is of no particular practical use, it is still a neat example of quantum parallelism. Suppose one is presented with a banknote, but is only allowed to have a look at one of the faces. How can one, without touching (i.e. turning) the banknote, determine with certainty whether it is legitimate or forged (i.e. both faces are the same)? Classically the task seems impossible, but it turns out that one can solve this problem by applying Deutsch's algorithm. In other words, it allows to determine the feature of a function (balanced or constant) with only one evaluation, as has been demonstrated experimentally with ion-traps [22].

1.3.3. Quantum Computing with Cluster States

Usual or standard quantum computation is based on sequences of unitary quantum logic gates that process the input qubits. A different and beautiful alternate way of performing quantum computation is based on so-called *cluster states*, which are highly entangled networks of qubits. The quantum computation is performed by a sequence of single-qubit measurements, whose outcomes can be classically *fedforward*. One of the advantages of this model is that errors, created by the intrinsic randomness of quantum measurement results, can be corrected by classical feedforward. This feedforward makes cluster state quantum computation deterministic. The order and choices of measurements determine the algorithm which is computed, so the cluster state model may be regarded as a truly measurement-only model of quantum computation that employs entanglement as the sole resource. This idea was first put forward by Raussendorf and Briegel [12], and recently experimental progress has been made with the first demonstration of a “*einweg*” quantum computer with cluster states [13].

Every cluster state computation starts with the preparation of the cluster state, which consists of highly entangled qubits. Such a cluster state can be built by preparing a sufficient number of qubits, each in the superposition state $|+\rangle = \frac{1}{\sqrt{2}}(|0\rangle + |1\rangle)$. A CSIGN-gate operation is then applied between neighboring qubits, effectively generating entanglement between them. This way, a number of different cluster states can be created, each representing and implementing a specific quantum circuit. Very importantly, theoretical work has shown that any quantum circuit can be implemented by a suitable cluster state, thus making cluster state quantum computation universal [12].

Once the cluster state is prepared⁵, the computation is performed by consecutive single-qubit measurements on this state. Any quantum logic operation can be carried out by the correct choice of the measurement basis, which results in single-qubit rotations,

⁵If measurements are made in the computational basis, they effectively disentangle and therefore remove the qubits from the cluster, therefore allowing the preparation of any arbitrary cluster state.

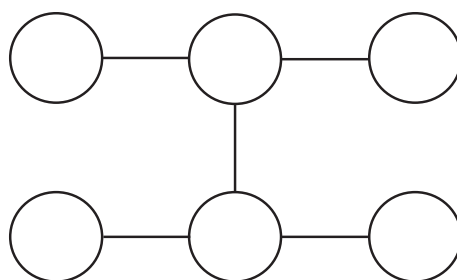


Figure 1.7.: Graphical example of a six-qubit cluster state. *CSIGN*-gate operations have to be applied between qubits which are connected in the graph.

together with a Hadamard operation⁶. An arbitrary single qubit unitary transformation can be simulated using a four qubit cluster state and three measurements [13].

Also very interestingly, even small cluster states are capable of demonstrating quantum computation, e.g. a four-particle “box”-cluster state is already sufficient to perform Grover’s search algorithm. It seems that cluster states are very promising for future implementations of quantum computers and the creation of such a cluster state is also the main motivation of the experiment which is investigated in this thesis.

⁶Each qubit measurement simulates the unitary evolution $HR_z(\Theta)$, where H is the Hadamard transformation and $R_z(\Theta)$ is a z -rotation defined by $R_z(\Theta)|0\rangle \rightarrow |0\rangle$ and $R_z(\Theta)|1\rangle \rightarrow e^{i\Theta}|1\rangle$.

2. Basics of the Experiment

Now that we are familiar with the basic concepts of quantum computation and quantum information, we will turn our attention to the experiment. In this chapter I will explain theoretically how basic instances of a quantum computer can be built in the lab. To be more precise, I will describe how to create suitable qubits (i.e. time correlated photons), how they can be controlled and manipulated using linear optics devices such as beamsplitters and waveplates and how quantum logic gates can be built out of that and in which way they can be characterized using quantum state and process tomography. At the end I will briefly show how a 3-photon cluster state can arise in our specific experiment.

2.1. Spontaneous Parametric Down-Conversion

As various experiments in quantum optics have to deal with single-photon states, a light source which produces discrete photon numbers is very important. Unfortunately, production and detection of such single photon states presents a major technological challenge. In addition, such photon sources tend to be spontaneous, i.e. they produce photons only randomly. Nevertheless, for the last twenty years, the choice for such single photon sources has been spontaneous parametric down-conversion, or SPDC for short [25].

Phase-matching

Parametric down-conversion and its reverse process, second-harmonic generation (SHG) typically takes place in non-linear optical materials, such as non-centrosymmetric crystals. In such a medium, the individual components of the induced dipole polarization inside the material can be written as a series expansion,

$$P_i = \chi_{ij}^{(1)} E_j + \chi_{ijk}^{(2)} E_j E_k + \chi_{ijkl}^{(3)} E_j E_k E_l \dots, \quad (2.1)$$

with E_i denoting the components of the electric field. At sufficiently high electric field strength, the non-linear higher-order term ($\chi^{(2)}$) in the expansion becomes significant. This eventually leads to oscillator terms which are driven by twice the frequency of the incident light, so that the reradiated waves have an energy of 2ω . This is called second-harmonic generation, while spontaneous parametric down-conversion describes the reverse process, in which light of energy 2ω is spontaneously *downconverted* into two photons of energy ω , where the probability for a photon to be down-converted is about 10^{-8} to 10^{-10} . As the initial wave of ω propagates through the crystal, it continues to produce second-harmonic waves which all add up constructively to form a single output beam if they maintain a proper phase relationship. In order to obtain this phase relationship

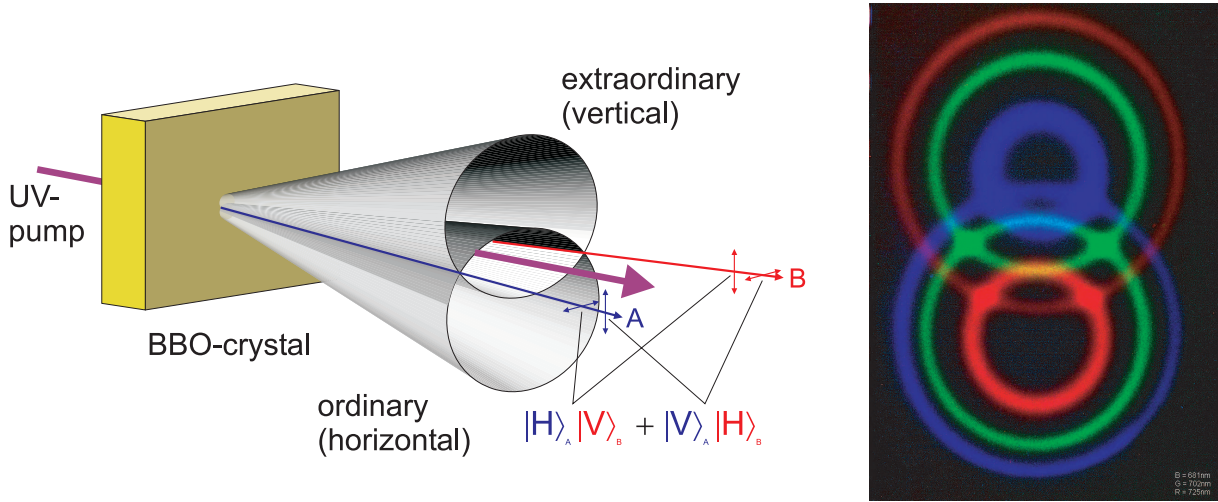


Figure 2.1.: Simplified scheme of type-II parametric downconversion and phase matching. On the right hand side, one can see the colour dependent opening cones and their intersections, where entangled photon pairs are emitted from the crystal. Picture courtesy of P.G. Kwiat.

and a good conversion efficiency, one must satisfy so-called phase matching conditions, i.e. the relations of the wavevectors and frequencies of the light involved have to satisfy momentum and energy conservation. In the process of parametric down-conversion, in which a pump photon decays into two photons, the conditions read like

$$\omega_p = \omega_s + \omega_i \quad (2.2)$$

$$\vec{k}_p \approx \vec{k}_s + \vec{k}_i, \quad (2.3)$$

where the subscripts p , s and i indicate the pump photon and the signal and idler photons, respectively and \vec{k} denotes the wave-vector in the non-linear medium. Most of the times, the crystal is cut in such a way that light impinging perpendicular to the crystal face forms an appropriate angle Θ with the optic axis so that the down-converted photons obey the momentum conservation, therefore allowing easy phase-matching in experiments.

The overall interaction of the crystal with the pump light can also be written as a quantum mechanical Hamiltonian

$$H = ga_p^\dagger a_s a_i + g^* a_p a_s^\dagger a_i^\dagger, \quad (2.4)$$

which has an elegant interpretation in the terms of photons¹ and where g is a coupling constant that contains the non-linear coefficient $\chi^{(2)}$. The first term represents SHG, while the second refers to SPDC, where a single “harmonic” photon is annihilated and two photons at ω are created.

¹ $a^{(\dagger)}$ is the annihilation (creation) operator in the Fock formalism, satisfying the conditions $a|n\rangle = \sqrt{n}|n-1\rangle$ and $a^\dagger|n\rangle = \sqrt{n+1}|n+1\rangle$, with n being the photon number.

Different types of phase matching

There exist different types of phase-matching and I will briefly explain their characteristics in the following. If the phase matching conditions are chosen such that all the created outgoing light is in one direction, then the phase matching or down-conversion is said to be *collinear*. In quantum optics experiments, the energies of both the signal and idler photons are usually chosen to be of the same wavelength and therefore degenerate, which implies $\omega_p = (\omega_s + \omega_i)/2$. For negative birefringent crystal, such as BBO (β -barium borate²), the ordinary (*o*-) constituent of the beam travels faster than the extraordinary (*e*-) one ($n_o > n_e$), allowing to satisfy above equation(s)³. There are two possible (polarization) combinations which correspond to two different types of phase matching. If we have an e-polarized pump creating two o-polarized down-conversion photons, then it is called *type-I*, while an e-polarized pump creating one e- and one o-polarized photon is known as *type-II* phase matching⁴. In our experiment, we are employing collinear, type-I phase matching for up-conversion (SHG), while exploiting non-collinear, type-II down-conversion for the production of correlated photon pairs. In the latter case, the phase matching angle Θ is chosen in such a way, that the down-converted, degenerate photons are emitted on two cones, representing the signal (*o*-) and idler (*e*-) beam, as shown schematically in Fig. 2.1.

2.1.1. A Source for Entangled Photons

The distinct emission geometry of non-collinear type-II SPDC is very interesting, since on the intersection of the cones it is impossible, in principle, to tell whether the photon was emitted by the *o*- or *e*-cone, and because they correspond to different polarization, the photons emerging along the intersections become polarization entangled. Note that in order to obtain genuine entangled photons, one has to compensate longitudinal (temporal) and transversal walk-off effects of the birefringent crystal due to group velocity mismatch, which, in principle, make the two photons distinguishable because of their different propagation behaviour. This is experimentally done by sending the photons through so-called compensation crystals, usually the same type of birefringent crystal (i.e. BBO in our case), but of just half the thickness. If we further exchange the roles of ordinary and extraordinary beam before the compensators by introducing HWP at 45° , the temporal and spatial walk-off will be canceled on average⁵. One might also argue that by employing this method the information about the arrival time of the photon is erased, as can be seen schematically in Fig. 2.2. However, at the end of the day, this leads to an entangled state of the form

$$\Psi = \frac{1}{\sqrt{2}} (|V\rangle_1 |H\rangle_2 + e^{i\varphi} |H\rangle_1 |V\rangle_2). \quad (2.5)$$

² β -BaB₂O₄

³There are many textbooks on this topic, so one may want to start out with Reference [27].

⁴Of course it is also possible for an *o*-polarized pump beam to generate either type of down-conversion.

⁵This can also be achieved by orienting the optical axis of the compensators perpendicular to the BBO's optical axis, in practice, however, the first method leads to better visibility, probably because of how the crystals are cut.

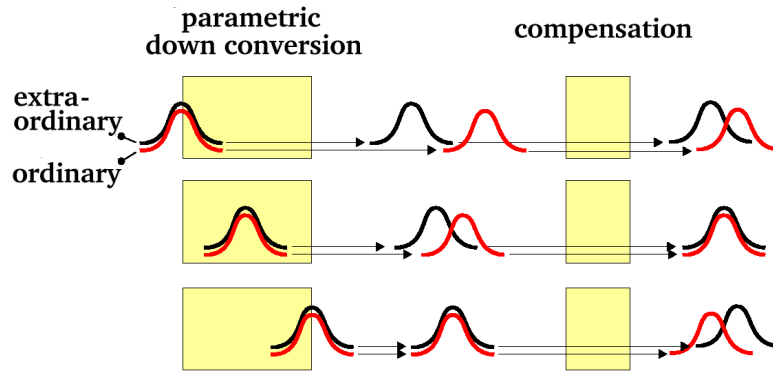


Figure 2.2.: Since PDC is a spontaneous process, the down-conversion of the pump photon is equally probable at any point within the crystal. Therefore, the temporal delay between a horizontally and a vertically polarized photon varies depending on the crystal thickness. By inserting compensators of half the thickness, one can, in average, delay the faster photon to erase the information which of the photons is first. The additional HWPs in front of the compensators are not shown for clarity. (Figure adapted from [26]).

The phase φ between the two coherent terms can be easily adjusted by introducing additional birefringent elements, or by slightly tilting one of the compensation crystals. In our teleportation experiments, we choose $\varphi = 0$ or $\varphi = \pi$ which results in the maximally entangled $|\Psi\rangle^+$ and $|\Psi\rangle^-$ state, respectively. For a more detailed description of an entangling type-II photon source, we refer the reader to [25, 26].

Collapsed Cones

The opening angle of the cones in Fig. 2.1 is a function of the wavelength and can be adjusted by a proper choice of Θ (i.e. slightly tilting the crystal in the experiment). In the extreme case, it is possible to shrink the cones to single point sources, in which case one obtains down-converted beams of higher intensity. This operation condition is also known as type-II “collapsed cones” [38] and since we only exploit the time correlation of our source and don’t need entangled photon pairs in the first instance, this is the phase matching condition of choice in our CSIGN-gate experiment. A photographic picture of the down-converted, collapsed cones can be seen in Fig. 2.3. Collapsed cones have a near-Gaussian beam profile, allowing for easy and efficient coupling into single mode fibers. As opposed to ring-like type-II downconversion, almost all of the down-converted light can be harvested (i.e. coupled), resulting in higher photon pair count rates in the experiment [38].

2.1.2. Gaussian Beam Propagation

Since the high intensity laser light, which is used to pump the nonlinear crystals, can be described by Gaussian beams it seems worth having a closer look at the properties of such beams and how their propagation can be simulated. This turns out to be very

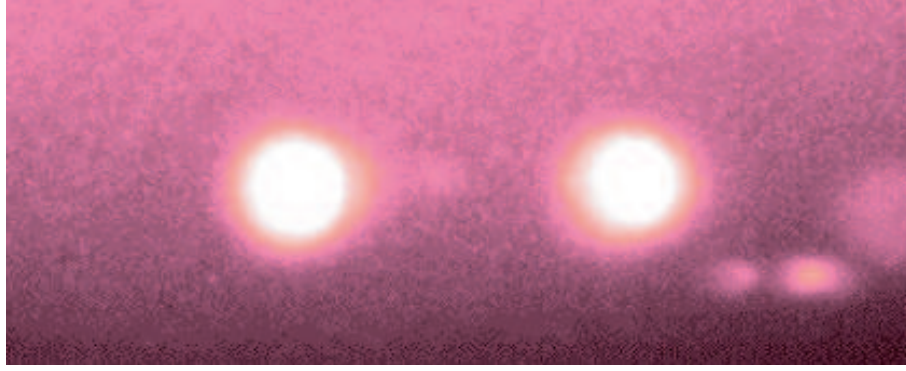


Figure 2.3.: *Photographic picture of collapsed cones type-II parametric down-conversion. The intensity of the beams is much higher compared to ring-like type-II phase-matching in Fig. 2.1. Picture courtesy of QT Lab.*

useful when trying to couple as much down-converted light as possible in optical fibers, as we will be doing in our experiment.

Gaussian beams are three-dimensional solutions of Maxwell's wave equations in free space. They are diffraction limited and characterized by the Gaussian shape of the transversal intensity profile and are completely determined by the position and waist for a given wavelength and refractive index, as can be seen in Fig. 2.4.

The beam radius $\omega(z)$ is usually defined as the radius where the intensity of the beam is decreased to its $1/e^2$ value. Within the diameter $2\omega(z)$, 86.5% of the whole beam power is contained. As the beam propagates, the beam radius increases as a function of the propagation distance z from the position of the waist ω_0 ,

$$\omega(z) = \omega_0 \sqrt{1 + \left(\frac{z \lambda}{\omega_0^2 n \pi} \right)^2}, \quad (2.6)$$

with ω_0 being the radius of the beam waist and n being the refractive index. Another helpful parameter is the *Rayleigh length* z_0 , which is defined by the distance where the beam radius $\omega(z) = \sqrt{2}\omega_0$,

$$z_0 = \frac{n \pi}{\lambda} \omega_0^2. \quad (2.7)$$

At this point, the wave front curvature is at its maximum, described by the curvature radius $R(z)$,

$$R(z) = z + \frac{1}{z} \left(\frac{\omega_0^2 n \pi}{\lambda} \right)^2, \quad (2.8)$$

and the divergence angle Θ for large distances from the waist can be determined by the equation

$$\Theta = \frac{\lambda}{n \pi \omega_0} = \frac{\omega_0}{z_0}. \quad (2.9)$$

All those parameters are indicated and shown in Fig. 2.4.

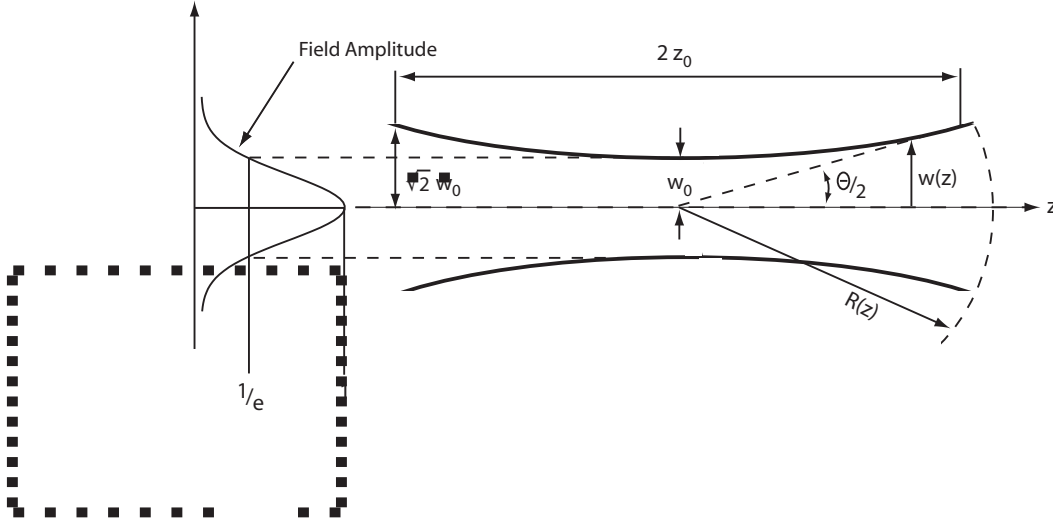


Figure 2.4.: Characterization and profile of a Gaussian beam. Beam waist ω_0 , Rayleigh length z_0 , wave front curvature $R(z)$ and divergence angle Θ are indicated.

ABCD-Matrices

A very helpful and elegant method for calculating the propagation of Gaussian beams is by defining a complex beam parameter $q(z)$:

$$\frac{1}{q(z)} = \frac{1}{R(z)} - \frac{i\lambda}{\omega(z)^2 n \pi} \quad (2.10)$$

With the help of this beam parameter, one can easily calculate the beam propagation using so-called *ABCD*-Matrices. The propagation formalism is based on the final matrix, which is obtained by including and considering all optical elements and paths in the range of the propagation. *ABCD*-Matrices for all kinds of optical elements and paths exist, but we will only be concerned by the matrices for free-space propagation L and converging lenses F , since those are the only elements employed in our setup.

$$D = \begin{pmatrix} 1 & d \\ 0 & 1 \end{pmatrix} ; \quad F = \begin{pmatrix} 1 & 0 \\ -\frac{1}{f} & 1 \end{pmatrix}, \quad (2.11)$$

where d is the length of the free space propagation and f is the focal length of the (converging) lens. By multiplying the respective matrices in the order of propagation, one obtains a final matrix M with elements A , B , C and D , hence the name *ABCD* matrix.

$$\begin{pmatrix} A & B \\ C & D \end{pmatrix} = M = D_1 \cdot F_1 \cdot D_2 \cdot F_2 \cdot \dots \quad (2.12)$$

Based on this matrix, the beam parameter of the emerging beam can be calculated from

$$q_{out} = \frac{q_{in} \cdot A + B}{q_{in} \cdot C + D}. \quad (2.13)$$

From this complex beam parameter, the physical relevant real values of the beam radius ω_{out} and wave front radius R_{out} can be obtained by

$$\frac{1}{\omega_{out}^2} = -\frac{n\pi}{\lambda} \operatorname{Im} \left\{ \frac{1}{q_{out}} \right\} \quad (2.14)$$

$$\frac{1}{R_{out}} = \operatorname{Re} \left\{ \frac{1}{q_{out}} \right\}. \quad (2.15)$$

2.2. Linear Optics Devices

2.2.1. Beamsplitter

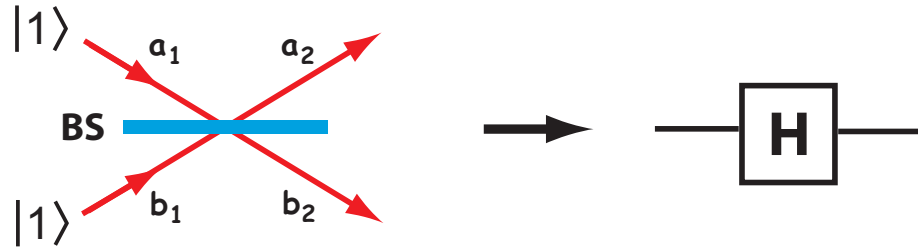


Figure 2.5.: The 50/50 beamsplitter acts like a Hadamard gate, creating superposition of the in- and outgoing particles.

This useful device is nothing more than a partially silvered piece of glass, which is made such that it reflects a fraction η of the incident light, and transmits $(1-\eta)$. It is usually made from two prisms with a thin metallic layer sandwiched in between. Most of the times the beamsplitter is chosen to split the incoming light 50/50 into the two outgoing modes, i.e. $\eta = 1/2$, so the action of the beamsplitter can be written as

$$\begin{aligned} a_1^\dagger &\rightarrow \frac{1}{\sqrt{2}}(a_2^\dagger + b_2^\dagger) \\ b_1^\dagger &\rightarrow \frac{1}{\sqrt{2}}(a_2^\dagger - b_2^\dagger), \end{aligned} \quad (2.16)$$

with a_1 (a_2) and b_1 (b_2) being the input (output) modes. It should be mentioned that, in this formulation, the phase shift convention of $\frac{\pi}{2}$ upon reflection for symmetric beamsplitters [28] has been incorporated into the second part of Eq. 2.16 (therefore the minus sign). A closer look reveals that the beamsplitter transformation is the same as for the Hadamard gate H (Eq. 1.17), as illustrated in Fig. 2.5.

Indistinguishability and HOM-Dip

Indistinguishability of quantum particles is a fundamental difference between classical and quantum physics. Due to the uncertainty principle, it is often not possible to label

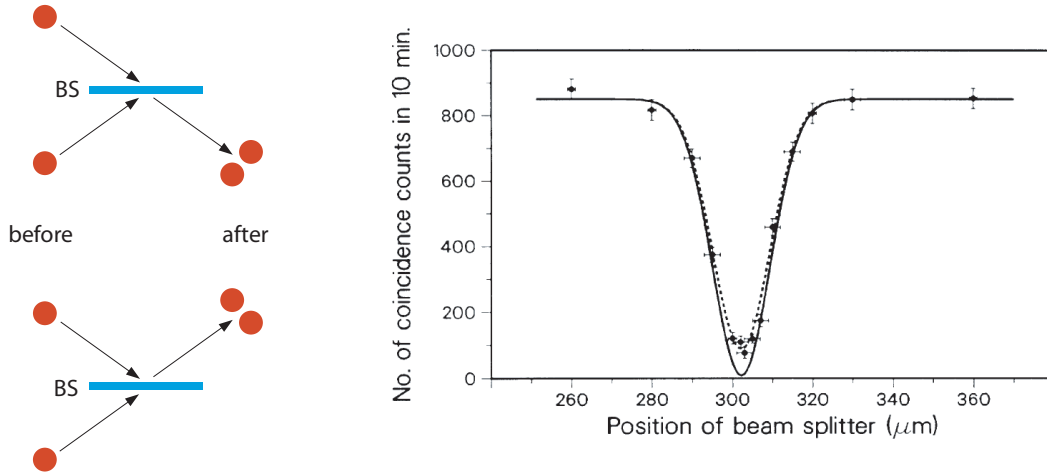


Figure 2.6.: Simplified scheme of photon bunching (left) and measured number of coincidences in the Hong-Ou-Mandel experiment as a function of the path length difference (right). The picture is taken from [29], where the dotted line represents the fit of the experimental data-points and the solid line shows the theoretical trace.

and keep track of particular particles, if they, for example, overlap on a beamsplitter as in Fig. 2.5. In other words, if there is no possibility, even in principle, to distinguish those particles by their spatial or spectral mode or by any other means like polarization and arrival time, then one cannot say whether both particles have been reflected or transmitted. This gives rise to quantum interference, and due to the bosonic nature of photons, the amplitude for these two events will cancel as we will see in the following.

Suppose both incoming modes of Fig. 2.5 are occupied with a single photon. Since the beamsplitter acts like a Hadamard gate we can describe the action at the beamsplitter as

$$H|1\rangle_a|1\rangle_b = \frac{1}{2} \left[(a_2^\dagger)^2 - (b_2^\dagger)^2 + b_2^\dagger a_2^\dagger - a_2^\dagger b_2^\dagger \right] |0\rangle. \quad (2.17)$$

If now the two photons in modes a , b are indistinguishable, then the last two term in Eq. 2.17 will cancel and we are left with the outgoing state of

$$|\Psi\rangle_{final} = \frac{1}{\sqrt{2}} (|2\rangle_a|0\rangle_b - |0\rangle_a|2\rangle_b), \quad (2.18)$$

where $a^\dagger|n\rangle = \sqrt{n+1}|n+1\rangle$. According to Eq. 2.18, all photon pairs will exit in the same output mode and no coincidences will be observed after the beamsplitter. Such an event is also called *photon-bunching*, and was first demonstrated experimentally by C.K. Hong, Z.Y. Ou and L. Mandel in 1987 [29]. By employing parametric downconversion as photon pair source and varying the photon path lengths in respect to each other, they could observe a significant dip in the coincidence rate as a function of the delay, as can be seen in Fig. 2.6.

This is also a nice method to measure time-intervals with sub-picosecond resolution, since

the full-width-half-maximum (FWHM) of the dip corresponds to the coherence-length of the wavepackets, which is usually in the order of 100-300 μm . The *visibility* or “depth” of the dip is governed by the degree of indistinguishability between the photons and therefore a good measure for the quality of the non-classical interference.

Polarizing Beamsplitters

Polarizing beamsplitters, or PBS for short, behave in almost the same way as ordinary beamsplitters, but with the important difference that they only reflect vertically polarized light, while transmitting horizontally polarized light. A number of different types of PBSs exist, and they can be used as polarizers in optical experiments. Adopting the nomenclature of Fig. 2.5, we can write the action of the PBS as

$$\begin{aligned} a_{1H}^\dagger &\rightarrow b_{2V}^\dagger \\ a_{1V}^\dagger &\rightarrow b_{1V}^\dagger \\ a_{2H}^\dagger &\rightarrow b_{1H}^\dagger \\ a_{2V}^\dagger &\rightarrow b_{2V}^\dagger \end{aligned} \tag{2.19}$$

PBSs play a significant role in our experiments as we will see later on, so it is well worth memorizing the action of those optical devices.

2.2.2. Half- and Quarter-waveplates

Half- and Quarter-waveplates, HWP and QWP for short, are very helpful optical elements which change the polarization of incident waves or photons. They belong to a class of optical elements known as *retarders* and are made of birefringent crystals, such as quartz or calcite. Upon incidence on such an uniaxial crystal, the light is divided in two coherent constituents of the beam, the ordinary and extraordinary (*o*- and *e*-) beam. If the optic axis is arranged to be parallel to the surfaces of the waveplate, the *e*-wave will have a higher propagation velocity than the *o*-wave if the waveplate is made of a medium with negative birefringence. So, after traversing the waveplate of thickness d , there is a relative phase difference of

$$\Delta\varphi = \frac{2\pi}{\lambda} d (|n_o - n_e|) \tag{2.20}$$

between the *o*- and *e*-waves, thus resulting in a different polarization, where n_o and n_e denote the refractive indices for the different beams.

HWP

The half-waveplate introduces a relative phase difference of π or 180° between the *o*- and *e*-waves if the thickness of the plate is chosen correctly. Suppose then that the polarization of incoming light makes some arbitrary angle Θ with the optic or fast axis, then the half-waveplate rotates the polarization through 2Θ . If Θ is chosen to be 45° , then the

polarization state of a photon will be flipped, i.e. $|H\rangle \rightarrow |V\rangle$ and $|V\rangle \rightarrow |H\rangle$. This rotation action can also be represented by a matrix, the so-called Jones matrix for HWPs,

$$R_{HWP}(\Theta) = \begin{pmatrix} \cos 2\Theta & \sin 2\Theta \\ -\sin 2\Theta & \cos 2\Theta \end{pmatrix}. \quad (2.21)$$

Expressed in terms of creation operators in the Fock picture, this can be written as

$$a_H^\dagger \rightarrow a_V^\dagger, \quad a_V^\dagger \rightarrow a_H^\dagger. \quad (2.22)$$

However, if the HWP is set to be at 22.5° , then it acts like Hadamard gate, creating superposition between the $|H\rangle$ and $|V\rangle$ polarization states, just like in Eq. 2.16.

$$\begin{aligned} a_H^\dagger &\rightarrow \frac{1}{\sqrt{2}}(a_H^\dagger + a_V^\dagger) \\ a_V^\dagger &\rightarrow \frac{1}{\sqrt{2}}(a_H^\dagger - a_V^\dagger) \end{aligned} \quad (2.23)$$

QWP

The quarter-waveplate is an optical element which introduces a relative phase shift of $\Delta\varphi = \pi/2$ between the constituent components of the beam. A phase shift of 90° converts linear polarized light into elliptical light and vice versa. When linear light at 45° to the principal axis is incident on a QWP, its o - and e -components have equal amplitude and therefore emerge as circular polarized light.

The corresponding Jones matrix for the quarter-waveplate oriented at 45° reads like

$$R_{QWP} = e^{i\pi/4} \begin{pmatrix} 1 & 0 \\ 0 & -i \end{pmatrix}, \quad (2.24)$$

while in the Fock formulation, the action of a QWP can be summarized as

$$a_H^\dagger \rightarrow a_H^\dagger + ia_V^\dagger, \quad a_V^\dagger \rightarrow a_H^\dagger - ia_V^\dagger. \quad (2.25)$$

2.3. Creation of a 3-Photon Cluster State

Now that we have finally got all the definitions straight, we can turn our attention to the experiment and see how a 3-photon cluster state (i.e. a GHZ-state) can be realized using linear optics devices and postselection alone.

Remember from Section 1.3.3, that in order to obtain a cluster state, one has to apply an entangling two-qubit gate such as the CSIGN-gate between two individual qubits, each being prepared in the superposition state $|+\rangle$. As we will see in the following, there exists a new, elegant and simple method of implementing this gate with special polarizing beamsplitters and half-waveplates.

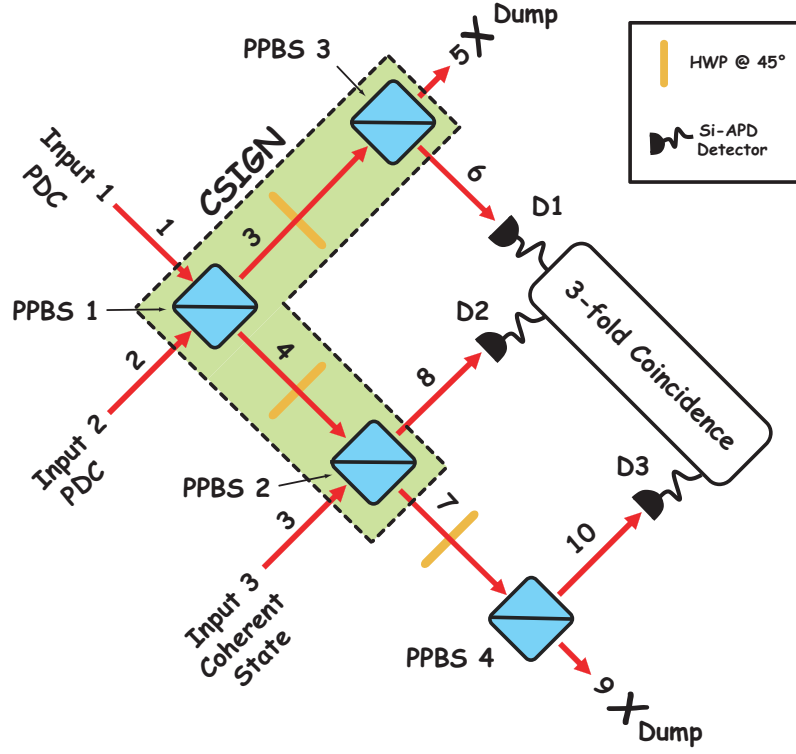


Figure 2.7.: Simplified scheme to generate a 3-photon cluster state (i.e. a GHZ-state). It consists of two concatenated CSIGN-gates, where the input photons for the first gate (dotted box) originate from PDC events while the third input photon consists of a weak coherent state. The cluster state is observed conditioned on a 3-fold coincidence detection of the photons, which occurs with probability $1/27$.

2.3.1. The Simplified CSIGN-Gate

The heart of our simplified linear-optics CSIGN-gate is a special partial polarizing beam-splitter, PPBS for short. It has the distinctive feature of perfectly reflecting vertical polarized photons (i.e. $R_V=1$), while only transmitting $2/3$ of the incident horizontal polarized photons, reflecting the remaining $1/3$ ($R_H = \sqrt{1/3}$). If we adopt the nomenclature of Fig. 2.7, where a_1, a_2 denote in incoming modes and a_3, a_4 the outgoing modes, then we can write the action of the first and central PPBS as

$$\begin{aligned} a_{1V}^\dagger &\rightarrow ia_{3V}^\dagger ; & a_{1H}^\dagger &\rightarrow i\sqrt{\frac{1}{3}}a_{3H}^\dagger + \sqrt{\frac{2}{3}}a_{4H}^\dagger \\ a_{2V}^\dagger &\rightarrow ia_{4V}^\dagger ; & a_{2H}^\dagger &\rightarrow \sqrt{\frac{2}{3}}a_{3H}^\dagger + i\sqrt{\frac{1}{3}}a_{4H}^\dagger, \end{aligned} \quad (2.26)$$

where we adopted the convention that reflection off a beamsplitter results in a phase shift of $\frac{\pi}{2}$. Similar transformations can be written for all the other PPBSs shown in Fig. 2.7. If we now choose input modes 1 & 2 to be occupied by qubits $\alpha|0\rangle + \beta|1\rangle$ (see Eq. 1.1), both

in a coherent superposition state (i.e. $\alpha = \beta = \sqrt{\frac{1}{2}}$), then according to our argument of Section 1.2.2, the CSIGN-gate should have an entangling action on the two qubits. Said that, after the first central PPBS we are left with the state :

$$|\Psi\rangle_{34} = \frac{1}{2} \left(\frac{2}{3} a_{3H}^\dagger a_{4H}^\dagger - \sqrt{\frac{1}{3}} a_{3H}^\dagger a_{4V}^\dagger - \sqrt{\frac{1}{3}} a_{3V}^\dagger a_{4H}^\dagger - a_{3V}^\dagger a_{4V}^\dagger \right) \quad (2.27)$$

Since we *postselect* on coincidence basis, all terms with two photons occupying the same mode (e.g. $a_{3H}^\dagger a_{3H}^\dagger$) have been discarded from the state description.

After the first PPBS, two half-waveplates, both set at 45° to the optic axis, swap the state of the qubit, so that we can relabel the subscripts of the state in Eq. 2.27 with $H \rightarrow V$ and $V \rightarrow H$. After traversing the second PPBS in Fig. 2.7, we end up with the state

$$|\Psi\rangle_{68} = \frac{1}{3} \left(a_{6H}^\dagger a_{8H}^\dagger + a_{6H}^\dagger a_{8V}^\dagger + a_{6V}^\dagger a_{8H}^\dagger - a_{6V}^\dagger a_{8V}^\dagger \right), \quad (2.28)$$

after postselecting coincidences in modes 6 and 8 only. Obviously, the $|V\rangle|V\rangle$ component got a sign-shift due to the gate operation⁶. The amplitudes for the four different terms are now all the same, therefore we say that the gate is *balanced* and the probability of a successful gate operation is $1/9$. Rewriting the output state in Eq. 2.28 gives

$$|\Psi\rangle_{68} \propto |H\rangle_6(|H\rangle_8 + |V\rangle_8) + |V\rangle_6(|H\rangle_8 - |V\rangle_8) = |H\rangle_6|+\rangle_8 + |V\rangle_6|-\rangle_8, \quad (2.29)$$

which is equivalent to the maximal entangled Bell-state $|\Phi\rangle^+$.⁷ The success probability of $1/9$ for our new CSIGN-gate architecture is as high as previous realizations of entangling gates [9, 30]. However, the construction of the gate is drastically simplified, as only one non-classical interference condition (at PPBS 1) is required for successful gate operation.

2.3.2. Coherent State Input

In order to generate a 3-photon cluster state we have to concatenate two CSIGN-gates, as is schematically shown in Fig. 2.7 and 7.1. As a third input, we choose an attenuated laser beam, which can mathematically be described by so-called *coherent states*.

The coherent state $|\alpha\rangle$ is the closest approximation to the quantum field generated by a laser and has properties similar to those of classical coherent light. But unlike a classical field which contains a definite amount of energy (and therefore a definite number of photons), a coherent state is made up of a superposition of photons

$$|\alpha\rangle = \sum_{n=0}^{\infty} |n\rangle \langle n|\alpha\rangle, \quad (2.30)$$

⁶Compare this to the CSIGN matrix of Eq. 1.24, where $|0\rangle$ is now encoded as $|H\rangle$ and $|1\rangle$ as $|V\rangle$.

⁷One can check this by letting a halfwave-plate at 22.5° act on the second qubit, transforming $|+\rangle \rightarrow |H\rangle$ and $|-\rangle \rightarrow |V\rangle$, therefore resulting in $|\Psi\rangle_{68} \propto |H\rangle_6|H\rangle_8 + |V\rangle_6|V\rangle_8$.

where $|n\rangle$ is the number state in the Fock formalism, i.e. photons are generated by a successive application of the creation operator

$$|n\rangle = \frac{(a^\dagger)^n}{\sqrt{n!}}|0\rangle. \quad (2.31)$$

So, by combining Eq. 2.30 and 2.31 and bearing in mind the completeness of the number state basis, one obtains the mathematical description of the coherent state $|\alpha\rangle$,

$$|\alpha\rangle_c = e^{-\frac{|\alpha|^2}{2}} \sum_{n=0}^{\infty} \frac{\alpha^n (a^\dagger)^n}{\sqrt{n!}} |0\rangle. \quad (2.32)$$

In fact, coherent states are experimentally produced by properly attenuating a laser beam, as will be done in our experiment later on, and in practice, α is chosen to be sufficiently small ($\alpha \ll 1$) so that the state

$$|\alpha\rangle_c \propto |0\rangle + \alpha|1\rangle + \frac{\alpha^2}{\sqrt{2}}|2\rangle + \dots \quad (2.33)$$

has main contributions of the first two terms only, with the vacuum state most of the times. With probability $|\alpha|^2$ the mode contains one photon, while the contribution of two photons in one mode is almost negligible.

The proper choice of α is very important for the outcome of the experiment, as the coherent state represents our third input photon for the creation of the 3-photon-cluster-state, as we can see in Fig. 2.7. However, for the sake of simplicity, let us assume that α is chosen in such a way that, ideally, one photon is released into the gate whenever there are two down-conversion photons exiting the first PPBS in our setup.

Then we can prepare the coherent state photon with a half-waveplate to be in the superposition state $|+\rangle$, so that we effectively have the state

$$|\alpha\rangle_c = \frac{\alpha}{\sqrt{2}}(a_{Hc}^\dagger + a_{Vc}^\dagger), \quad (2.34)$$

with $\alpha \ll 1$, entering the second PPBS. Applying the right transformation rules⁸ similar to those in Eq. 2.26, postselecting three-fold coincidences between output modes 6, 8 and 10 plus a little calculus then leave us with the three particle state

$$\begin{aligned} |\Psi\rangle_{6,8,10} \propto & |HHH\rangle + |HHV\rangle + |H VH\rangle - |HVV\rangle \\ & + |VHH\rangle + |VHV\rangle - |VVH\rangle + |VVV\rangle, \end{aligned} \quad (2.35)$$

which contains all eight possible computational state arrangements. This state is equivalent to a maximally entangled three-particle GHZ-state [16], as can be seen by rewriting $|\Psi\rangle_{6,8,10}$ as

$$|\Psi\rangle_{6,8,10} \propto | + H + \rangle + | - V - \rangle. \quad (2.36)$$

⁸i.e., interchange the subscripts of Eq. 2.26 as follows: 1→4, 2→c, 3→8, 4→7 and similar for PPBS 4.

By applying local rotations on qubits 1 and 3 this results in a 3-photon-linear cluster state, which is indeed equivalent to the better known GHZ-state

$$|\Psi\rangle_{GHZ} \propto |HHH\rangle + |VVV\rangle. \quad (2.37)$$

The probability of successful gate operation is $1/27$, which compares favourably with $(1/9)^2=1/81$, which would be achieved if two individual CSIGN-gates would be placed in succession. It is one of the main advantages of this circuit (setup), that gates can be concatenated this way with the successful operation scaling as $(1/3)^n$ rather than $(1/9)^{n-1}$, where n is the number of qubits in the circuit [19].

Applying this strategy, in principle, an arbitrary number of qubits can be connected (i.e. entangled), creating an N-qubit cluster state useful for quantum computation. Other useful applications of this circuit include the ability to disentangle and therefore distinguishing every GHZ-state (if the circuit is run in reverse) and the possibility to perform parity checking, i.e. identifying bit-flip errors while preserving the superposition of the qubits and can therefore be used to demonstrate bit-flip error correction [31].

2.4. Gate-Tomography

Now that we have examined how our CSIGN-gate creates entanglement between individual qubits we wish to characterize the dynamics of our gate experimentally, i.e. how and with which fidelity the gate transforms our given input states. Fortunately, there exist a mathematical model for doing this: *Quantum Process Tomography*, which reconstructs the evolution operator that completely describes the dynamics of our quantum gate. But to understand process tomography, we first need to explain quantum state tomography.

2.4.1. State-Tomography

In a nutshell, *quantum state tomography* is the procedure of experimentally determining an unknown quantum state, i.e. an exact measurement of all the components of the states. As Stokes [32] showed, the polarization state of a single photonic qubit can be determined by taking a set of four projective measurements which are represented by the operators

$$\begin{aligned} \mu_0 &= |H\rangle\langle H|, & \mu_3 &= |D\rangle\langle D|, \\ \mu_1 &= |V\rangle\langle V|, & \mu_4 &= |R\rangle\langle R|, \end{aligned} \quad (2.38)$$

and similarly the state of two qubits can be determined by a set of 16 measurements (represented in the following by $|\Psi\rangle_\nu$, $\nu = 1, 2, \dots, 16$), which are all possible permutations of the above operators $\mu_i \otimes \mu_j$, where $i, j=0,1,2,3$. In general, a n -qubit system requires 4^n measurements.

The average number of counts in the detector is given by the formula $n_i = \mathcal{N} \text{tr}(\rho \cdot \mu_i)$, where ρ is the density matrix representing the state of the qubit and \mathcal{N} is constant that can be determined from the experimental data (includes light intensity, detector efficiency). Since we want to characterize the output of a two-qubit gate, lets from now on only

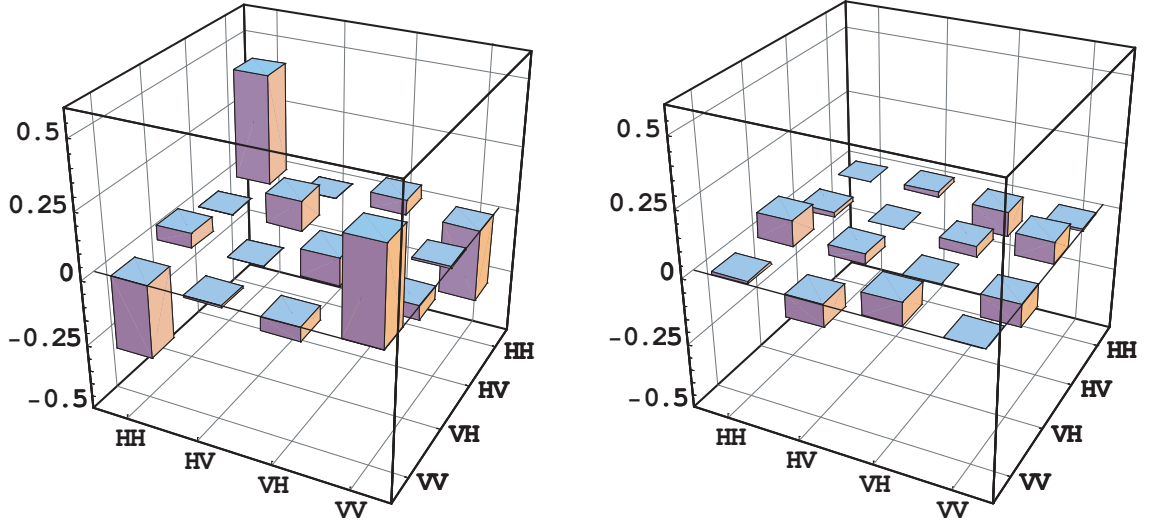


Figure 2.8.: An example for a two-qubit density matrix reconstructed by quantum state tomography employing maximum-likelihood estimation. The left plot shows the real part of ρ , the right plot the imaginary part. This plot shows a density matrix of an experimentally prepared and entangled state $|\Phi\rangle^- = \frac{1}{\sqrt{2}}(|HH\rangle - |VV\rangle)$.

worry about state tomography of a two-qubit system. The density operator representing this two-qubit state is a 4x4 density matrix with 16 real parameters (of which 15 are independent). For the density matrix to be physical, we want it to be:

- **hermitian**, i.e. $\rho = T^\dagger T$
- **non-negative**, i.e. $\langle \Psi | \rho | \Psi \rangle \geq 0$
- **normalized**, i.e. $\rho = \frac{T^\dagger T}{\text{tr}(T^\dagger T)}$

As mentioned above, the matrix is a function of 16 real variables, which we will denote as t_1, t_2, \dots, t_{16} . For various reasons [33], it is useful and convenient to choose a tridiagonal form for T :

$$T(t) = \begin{pmatrix} t_1 & 0 & 0 & 0 \\ t_5 + i t_6 & t_2 & 0 & 0 \\ t_{11} + i t_{12} & t_7 + i t_8 & t_3 & 0 \\ t_{15} + i t_{16} & t_{13} + i t_{14} & t_9 + i t_{10} & t_4 \end{pmatrix} \quad (2.39)$$

To quantify how good the density matrix $\rho(t_1, t_2, \dots, t_{16})$ is in agreement with the measured experimental data (i.e. coincidence rates), we introduce the so-called “likelihood-function”, which represents the deviation of the density matrix ρ from the measurement. Since the expected number of coincidence counts in a given experimental run is given by

$$n_\nu = \mathcal{N} \langle \Psi_\nu | \rho | \Psi_\nu \rangle, \quad (2.40)$$

the deviation from the observed ν th coincidence measurement is represented by

$$\Delta f = \sum_{\nu=1}^{16} \frac{(n_{\nu} - \mathcal{N}\langle\Psi_{\nu}|\rho|\Psi_{\nu}\rangle)^2}{2\mathcal{N}\langle\Psi_{\nu}|\rho|\Psi_{\nu}\rangle} \quad (2.41)$$

with Δf being the likelihood-function⁹, ρ being a function of t_1, t_2, \dots, t_{16} and $\mathcal{N} = \sum_{\nu=1}^4 n_{\nu}$ (see [33]). Fortunately, mathematic computer packages like `Mathematica 5.0` are able to execute an algorithm which finds the minimum of this functions and all corresponding values of t_1, t_2, \dots, t_{16} , and therefore the desired density matrix which represents our two-qubit system. An example can be seen in Fig. 2.8.

2.4.2. Process-Tomography

Although we now have determined the output quantum states via quantum state tomography (QST), we still do not know the dynamics of our gate, i.e. in which way it transforms our given input state. However, in a similar manner to QST, a set of output states enables the reconstruction of the gate operation. To determine this quantum transfer function, we have to determine the linear map \mathcal{E} , which completely describes the dynamics of the quantum system, in our case the CSIGN-gate, so that the state change experienced by the gate can be written as

$$\rho \rightarrow \mathcal{E}(\rho), \quad (2.42)$$

where we have to obey the condition that the trace $\text{tr}(\mathcal{E}(\rho))$ is always equal to one. Any quantum operation \mathcal{E} can also be written in the so-called *operator sum representation* for an arbitrary input state ρ

$$\mathcal{E}(\rho) = \sum_k E_k \rho E_k^{\dagger}, \quad (2.43)$$

where E_k are the *operation elements* and have to obey the completeness relation,

$$\sum_k E_k^{\dagger} E_k = 1, \quad (2.44)$$

to ensure that ρ remains hermitian with trace one. The set of operation elements $\{E_k\}$ completely describes the action of the gate and with process tomography we want to experimentally determine some of the E_k matrices. If one now chooses a fixed basis $\{\tilde{E}_m\}$ for the operators on the state space then we can express the operation elements in this basis as $E_i = \sum_m a_{im} \tilde{E}_m$ and Eq. 2.43 becomes

$$\mathcal{E}(\rho) = \sum_{mn} \chi_{mn} \tilde{E}_m \rho \tilde{E}_n^{\dagger}, \quad (2.45)$$

⁹Actually, this is not as straightforward as it seems. The likelihood P that ρ reproduces the data, given the coincidence measurements have a Gaussian probability distribution, is

$P = \prod_{\nu=1}^{16} \exp\left[-\frac{(n_{\nu} - \mathcal{N}\langle\Psi_{\nu}|\rho|\Psi_{\nu}\rangle)^2}{2\mathcal{N}\langle\Psi_{\nu}|\rho|\Psi_{\nu}\rangle}\right]$, where the standard deviation is given approximately by Poissonian noise, i.e. $\sqrt{n_{\nu}}$. But it is actually easier to find the minimum of the logarithm of this function P , which leads us eventually to Eq. 2.41.

where χ_{mn} is a positive hermitian matrix $\chi_{mn} = \sum_i a_{im} a_{in}^*$ that now completely describes the process in the chosen basis.

Usually the basis of input states is chosen such that the matrices $\rho^{(jk)}$ representing them all have a 1 in the j^{th} row and k^{th} column and zeros elsewhere. A suitable set for the experiment are the operators $|H\rangle\langle H|$, $|V\rangle\langle V|$, $|D\rangle\langle D|$, and $|R\rangle\langle R|$, which are related to some other basis $\rho^{(\alpha\beta)}$ by $\rho^{(jk)} = M^{-1}\rho^{(\alpha\beta)}$ and the 16x16 matrix M^{-1} can be found in [34].

The complete set $\{\rho^{(\alpha\beta)}\}$ of input states for two-qubit tomography consists of 16 two-qubit states given by all the tensor products of the single-qubit states¹⁰,

$$\{\rho^{(\alpha\beta)}\} = \{\rho^{(\alpha)} \otimes \rho^{(\beta)}\}, \quad \alpha, \beta \in \{H, V, D, R\}, \quad (2.46)$$

and performing tomography on each of them one obtains a set of output matrices $\{\mathcal{E}\rho^{(jk)}\}$ using the inverted M matrix of Reference [34]. It is then possible to reconstruct the 16x16 χ matrix in block form:

$$\chi = K^T \begin{pmatrix} \mathcal{E}\rho^{(11)} & \mathcal{E}\rho^{(12)} & \dots \\ \mathcal{E}\rho^{(21)} & \mathcal{E}\rho^{(22)} & \dots \\ \vdots & \vdots & \ddots \end{pmatrix} K, \quad (2.47)$$

where K is a particular matrix written as $K = P \cdot \Lambda$ with the permutation matrix $P = I \otimes [\rho^{(11)} + \rho^{(23)} + \rho^{(32)} + \rho^{(44)}] \otimes I$ and $\Lambda = [Z \otimes I + X \otimes X] \otimes [Z \otimes I + X \otimes X] / 4$. Unfortunately, this procedure does not allow the incorporation of experimental uncertainties for a full error analysis. But still there exists a measure which tells how much the obtained process matrix resembles the ideal gate, namely the *gate fidelity* F_g between the ideal, target unitary gate U and the actual process \mathcal{E}

$$F_g(U, \mathcal{E}) = \min \langle \Psi | U^\dagger \mathcal{E}(|\Psi\rangle\langle\Psi|) U | \Psi \rangle, \quad (2.48)$$

with U being, in our case, the ideal CSIGN matrix and the minimum is over all input states $|\Psi\rangle$.

However, similar to QST, the process matrix χ can give unphysical results in certain cases and numerical optimization methods have been developed which account for this, very much equal to the maximum-likelihood approach in QST¹¹.

¹⁰where, for the sake of completeness, the single qubit states are written as

$$\rho^{(H)} = \begin{pmatrix} 1 & 0 \\ 0 & 0 \end{pmatrix}, \rho^{(V)} = \begin{pmatrix} 0 & 0 \\ 0 & 1 \end{pmatrix}, \rho^{(D)} = \frac{1}{2} \begin{pmatrix} 1 & 1 \\ 1 & 1 \end{pmatrix} \text{ and } \rho^{(R)} = \frac{1}{2} \begin{pmatrix} 1 & -i \\ i & 1 \end{pmatrix}.$$

¹¹Since we don't want to confuse the reader more than necessary we refer to [34, 35, 36] for a detailed description of this numerical optimization method.

3. Description of the Setup

This chapter briefly describes the basic outline of the (optical) setup at the University of Queensland and of all the equipment that is being used, such as lasers, detectors, filters, etc. A simplified scheme of the setup can be seen in Fig. 3.2 and we will often refer to it in the following.

3.1. Lasers

The principal photon source for our experiment is a Titanium Sapphire Laser (Ti:Sapphire) from Spectra Physics called “Tsunami”. It is pumped by a Millennia X laser, which consists of a Neodymium Yttrium Vanadate (Nd:YVO₄) laser crystal and produces 10 W of infrared power which is subsequently frequency-doubled to 532 nm which is its output wavelength. The Millennia itself is pumped by two 20 W fiber-coupled diode laser bars located in the power supply.

The Millennia-pumped Tsunami is a mode-locked pulsed laser configured for a wavelength tuning range of 750-850 nm, where it produces an average power of 1.3 W at a repetition rate of 78 MHz. Wavelength selection is done with a birefringent filter, that consists of crystalline quartz plates placed in the laser cavity at Brewster’s angle. The plates are cut parallel to their optical axes, and due to their birefringence the linear polarization of the incident laser beam becomes elliptical. Only a narrow range of wavelengths makes a complete 180° (or multiple thereof) polarization flip and remains linearly polarized; all other wavelengths are transformed to elliptically polarized light and suffer losses at each Brewster-angle surface within the cavity and, therefore, fail to reach lasing threshold. Rotating the filter about an axis normal to the plates changes the wavelengths that remain linear polarized and therefore allow the output wavelength to be tuned. To change the pulse width, one can modify the net group velocity dispersion (GVD). The optical components in the laser cavity introduce positive GVD and cause pulse spreading. In order to obtain stable, short output pulses, these effects must be compensated with negative GVD, which can be achieved and controlled by a so-called Gires-Tournois Interferometer. It also allows alignment of the laser cavity and therefore optimization of output power and mode quality.

The Tsunami in this experiment is operated at 820 nm with a pulse length of approximately 65 fs, resulting in a FWHM of $\Delta\lambda=12-14$ nm. The spatial output mode is the TEM₀₀ mode (Gaussian beam profile) and the polarization is vertical with quality 500:1. A spectrometer is placed close to the output window of the Tsunami and facilitates wavelength tuning if laser light is scattered towards the measurement head.

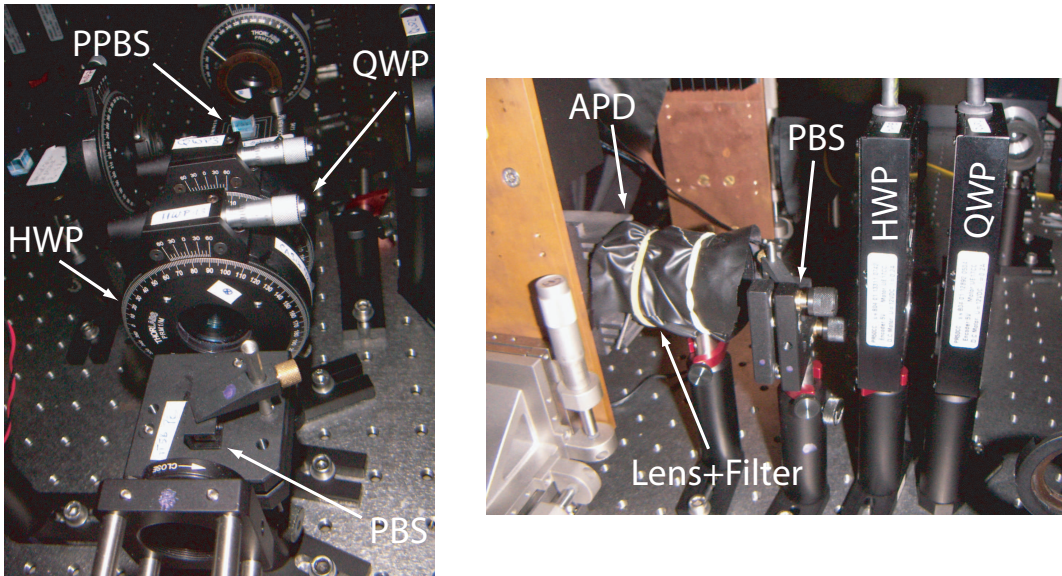


Figure 3.1.: *Left Picture: State preparation for the optical CSIGN-gate. The photons emitted by the single-mode fiber traverse a PBS, which only transmits horizontally polarized photons. Subsequently, a HWP and a QWP prepare the desired polarization state of the photon. Right Picture: Analyzer and detector. The automated analyzer consists of motor-driven HWP and QWP, and a PBS acting as a polarizer. To the left one can see the head of the detector and the filter/lens combination, hidden behind black cloth.*

3.2. Optical Setup

The infrared 820 nm laser light is focused on a birefringent BBO crystal with a planconvex lens¹ (35 mm focal length), where second-harmonic generation converts a small fraction of the incident light to blue 410 nm (see Section 2.1), resulting in a pump beam of approximately 200 mW power. A second lens collimates the light again and two fast prisms spatially separate the remaining red light from the desired blue laser light. Some of the red light is attenuated and coupled into single-mode fiber and used as the coherent state input in the setup, as we shall later see. The blue beam, however, continues and is focused by a 125 mm lens onto another BBO crystal, after traversing a HWP. This, second BBO, is cut for collapsed cones type-II parametric down-conversion (again, see Section 2.1 for details) and the HWP allows one to change the incident polarization at the crystal². After the crystal, a special high pass band filter blocks the remaining blue light and transmits the down-converted red light. A series of (flipable) mirrors directs the light to 2 Thorlabs Fiber-Couplers (FC), which collect and focus the beam with a 4 mm lens onto a 820 nm single-mode fiber of roughly 5 μm core diameter. The position and focal lengths of the lenses have been calculated by means of Gaussian beam propagation, as described in Sec-

¹both lenses and the crystal are antireflection (AR) coated for 410 and 820 nm.

²since the BBO is cut for type-II PDC, only horizontal light will be down-converted and by turning the waveplate, one can easily check whether detected light is due to down-conversion.

tion 2.1.2 to achieve the best fiber coupling efficiency possible [37]. The single-mode fibers only allow propagation of the Gaussian TEM_{00} mode and therefore serve as spatial mode filters. (Output-) Polarization can be controlled by twisting the fiber in a special mount, so-called Polarization Controllers³. After the beam is collimated again by another set of FCs, it enters the optical CSIGN-setup (Fig. 3.2) through a combination of PBS, HWP and QWPs each (see left picture in Fig. 3.1). These waveplates allow one to prepare any polarized light as input states for the CSIGN-gate, namely H-, V-, D- and R- polarized light. The two input states (i.e. polarized photons at that point) propagate through the gate as described in Section 2.3.1, and are afterwards detected by an automated polarization analyzer, which consists of HWP, QWP and a PBS acting as a polarizer, only transmitting H-polarized light to single photon detectors (see Fig. 3.1). Each input HWP and QWP is precision mounted, that means their angle can be adjusted with a resolution of 5 degree-minutes. Those waveplates making up the automated polarization analyzer are mounted in motordriven Newport Rotation Stages, and they can be turned with an angle resolution of 1 degree-minute with the help of a Newport Motion Controller. This Controller is part and parcel of the whole experiment, since it allows for automated quantum state (and process) tomography, as we will later see.

3.3. Detectors

Eventually, as in any quantum optics experiment, the light, i.e. the photons, has to be detected. In our experiment, we use Perkin Elmer Single Photon Detectors (SPCM-AQR-14 - Si APD Single Photon Counting Module) with less than 100 dark counts per second (cps). These are silicon avalanche photon detectors which have an overall detection efficiency of approximately 40-45 % on their imaging area of $175 \mu\text{m}$ diameter. The semiconductor silicon is operated with a reverse bias voltage in excess of its break down voltage, called the Geiger-mode, so that the energy of a single incident photon triggers a electron “avalanche”, that is further amplified and converted to a 35 ns wide TTL pulse of 2.5 Volts (minimum) high in a 50Ω load. There is a “dead time” of 50 ns in between pulses and the modules require a +5 Volt power supply. One has to take extreme care not to expose the detectors to excessive light intensities, and therefore narrow-banded interference filters (3 nm) are used in front of every detector, in conjunction with lenses which focus the beam onto the detection area. The space in between the detector and filter/lens mount is covered with black drapery (see right picture in Fig. 3.1).

3.4. Coincidence Logic

The scheme of the experiment requires us to detect photons simultaneously or “in coincidence”, because only then the gate operates as desired and outlined before (coincidence postselection). We employ an Ortec Time-to-Amplitude Converter/SCA Coincidence Logic (TAC-SCA) and a CCNIM Quad 100-MHz Counting device, as well as an

³For more details concerning Polarization Controllers, see Section 9.3.1.

3. Description of the Setup

Ortec Delay Generator to look for coincidence signals from the photon detectors. The coincidence window and the delay are set such that only photons detected within a time window of 1 ns are registered and counted. The counting module can be accessed via a IEEE-488 interface so that the single and coincidence counts can be observed on a computer. But more interestingly, it allows for automated measurements and data collection.

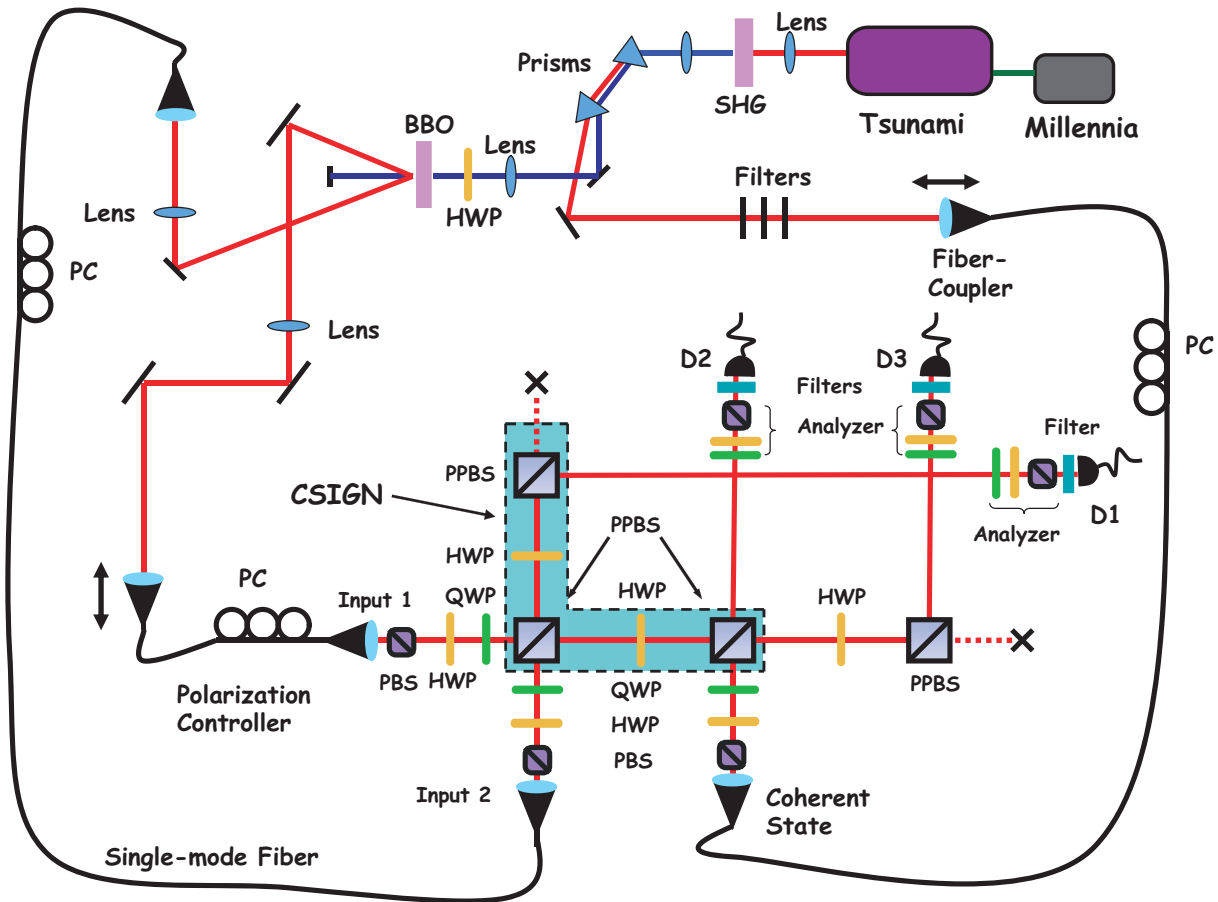


Figure 3.2.: Schematic scheme of the setup. Automated analyzers consist of HWP, QWP and PBS each and allow for easy and automated state/process tomography. The dashed box indicates the central CSIGN-gate, at whose heart are 3 partially PBS (PPBS), which perfectly reflect vertical polarized light but only transmit $\frac{2}{3}$ of the horizontal (see Section 2.3.1 for further explanation).

4. Experimental Procedure

Now that we have extensively discussed the prerequisites, let us now proceed to the more exciting part of this thesis, the experiment itself. After explaining shortly how to create time correlated photons via our parametric-down-conversion source, calibrate the waveplates and find the HOM Dip, I describe the procedure for the gate tomography, which we will need to perform in order to determine the action and fidelity of our CSIGN-gate.

4.1. Pre-experimental Alignment

In order to be able to carry out the experiment in a reasonable way, one needs a proper source of time correlated photons, or in other words, a decent down-conversion (DC) source with high coincidence rates. While tweaking up the output power of the laser (without changing the wavelength) is a rather straight-forward task, obtaining good conversion- and collection-efficiencies of the parametric down-conversion is not. In our setup, we are employing type-II “collapsed cones” PDC [37] as our phase matching condition of choice, as explained in Section 2.1.1. To check whether one is operating the crystal at the right conditions, a CCD camera was set up approximately 1 m after the BBO crystal, and two lenses were employed to focus both down-conversion beams onto the imaging area of the camera. By slightly tilting the crystal to adjust the phase matching condition, we aimed for down-conversion as depicted in Fig. 2.3. By turning the HWP in front of the BBO one can verify whether the detected light is really originating from down-conversion, since light due to fluorescence or background is in general unpolarized. Unfortunately, perfect phase matching as in Fig. 2.3 was never achieved with one of the two cones always being slightly less intense than the other.

We then proceeded and started to couple as much of this down-converted light into single-mode optical fibers, which I will describe briefly in the following:

Once reasonable DC is picked up by the CCD camera, the camera is removed together with the two lenses and free-space detectors are placed in the line of the emerging down-conversion beams, approximately 1.5 m after the BBO. As soon as they pick up a signal due to the DC, the coincidence rate is improved by tweaking up the singles rate in one of the two arms and subsequently following with the other detector by observing the coincidence rate. This way we achieved a photon pair rate of around 16000 per second, with a background of about 1000 per second due to accidental coincidence counting¹.

¹Accidentals occur due to high single photon count rates, which result in two random (i.e. not from DC) photons arriving at the logic within the coincidence window of 1 ns. In general, the accidental coincidence rate is calculated by $C_{acc} = \frac{S_1 S_2}{\tau}$, with $S_{1,2}$ being the singles rates and τ being the coincidence window.

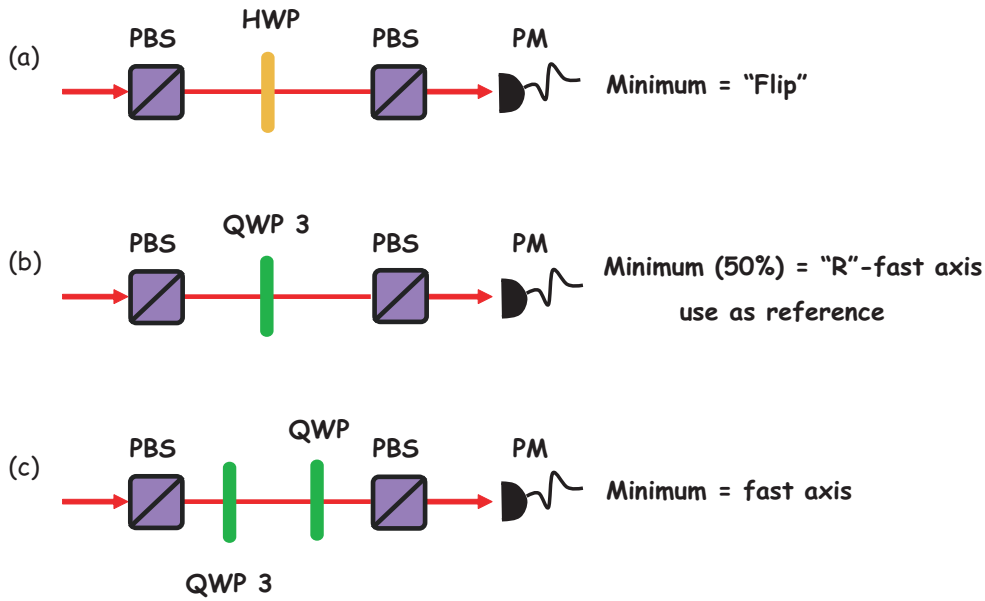


Figure 4.1.: Half-waveplate (a) and quarter-waveplate calibration (b,c). See text for further explanation.

Next we set up two irises in each DC arm, therefore fixing the line of the emitting DC light in space. This way, with the help of a visible diode laser at 670 nm and additional flipping mirrors, it was possible to pre-align the fiber-couplers to a sufficient degree so that fiber coupling the DC light was simplified. Once the polarization and the focus was readjusted for 820 nm DC photons, tweaking up the coincidence rates by “walking-in” the fiber couplers yielded around 300 coincidences a second between Detector 1 & 2 (see Fig. 3.2)².

4.1.1. Waveplate Calibration

Overall, nine half-waveplates and six quarter-waveplates are employed in the experimental setup, serving for input state preparation, output state analysis or for flipping the polarization in between beamsplitters. Waveplates have been discussed in detail in Section 2.2, so I will only describe their calibration in the following. Since accurate waveplate settings are of major importance for the precision of the experiment, their calibration has to be carried out with great care.

For calibration purposes, a 820 nm laser diode and two PBSs, both set to transmit horizontal polarization, are set up in front of a photometer (PM), as shown in Fig. 4.1.

²This was measured with vertically (V) polarized photons entering the CSIGN-gate, while the HWP in between the PPBS were set to “0”, i.e. they don’t change the polarization. This way both input photons were perfectly reflected at each PPBS and finally detected in coincidences without any major losses due to interference effects.

In succession, each of the half-waveplates was inserted between the two polarizing BS and rotated in steps of 5° , while the intensity was measured and recorded, eventually obtaining a full fringe pattern. By fitting this fringe with a Sine-function, the position (i.e. the actual angle on the precision-mount of the waveplate) of the optical axis could be calculated. In principle, whenever the optic axis subtends an angle of 45° with the horizontal polarized light, it will flip its polarization and therefore fails to transmit the second PBS, resulting in an intensity minimum at the photometer.

A similar approach has been taken for the calibration of the quarter-waveplates. When linear light at 45° to the principal axis is incident on a QWP it is transformed into circular polarized light, which eventual results in a 50% drop of intensity at the photometer. Once we had done this for one the QWPs we subsequently used it (QWP No. 3) as a reference for the calibration of the other QWPs. When inserted one after the other in between the PBSs the two QWPs will form an effective HWP if both principal axes (“fast axes”) line up in the right way. Therefore the polarization of the light is flipped at this position, again resulting in a minimum intensity at the photometer and by Sine-fitting the intensity fringes we could calculate the position of the optical axis with a precision of about $\pm 0.5^\circ$.

4.1.2. PPBS-Characterization

Since the PPBSs and their unique feature of reflecting 1/3 of the incident horizontally polarized light is so important for the proper action of our gate, we checked and characterized their behavior. By using both a laser diode at 820 nm and single photons from the PDC source (femtosecond pulse characteristic), we found the actual splitting ratio to be $28:72 \pm 0.01$ for PPBS 1 & 2 and $29:71 \pm 0.01$ for PPBS 3. Unfortunately this deviation from the ideal splitting ratio of $1/3 : 2/3$ can not be compensated and therefore perfect gate operation cannot be ensured. In addition this also hinders the perfect quantum interference at the PPBS (photon indistinguishability), leading to a HOM-Dip of lower visibility, as can be seen in the next section. While a splitting ratio of $1/3 : 2/3$ would allow an ideal visibility of 80%, the deviation from the ideal splitting ratio results in an ideal visibility of $V_{ideal}=67\%$, where the ideal visibility for general reflectivity η can be calculated³ as

$$V_{ideal} = 1 - \frac{|(1 - \eta) - \eta|^2}{|1 - \eta|^2 + |\eta|^2}. \quad (4.1)$$

4.1.3. HOM-Dip

Indistinguishability between quantum wavepackets gives rise to quantum interference and since this non-classical interference and its quality at the PPBSs is crucial to the performance of our CSIGN-gate, one has to make sure to meet all the requirements to make them indistinguishable. Photons, in principle, can be distinguished due to any differences in their spectral-, spatial- and polarization- as well as their temporal mode

³The HOM-Dip visibility is defined as $V = \frac{Max-Min}{Max}$, where *Max* denotes the countrate outside of the HOM-Dip, hence $|1 - \eta|^2 + |\eta|^2$ and *Min* is the low-point of the dip and given by $|(1 - \eta) - \eta|^2$.

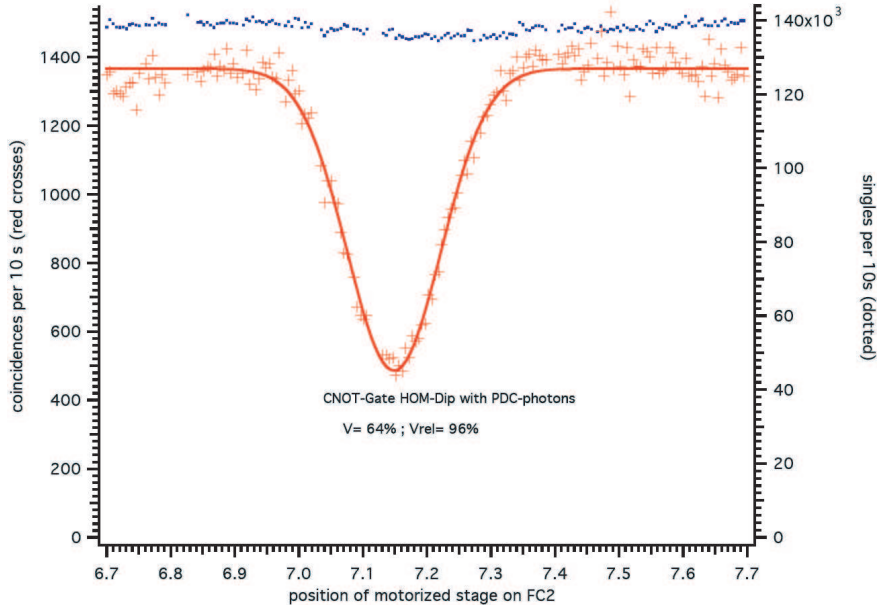


Figure 4.2.: Graphical representation of the HOM-Dip-Search. One clearly sees the Gaussian shape dip in coincidence count rates between Detector 1 & 2, indicating the position of ideal temporal overlap of the input photons. The observed HOM-Dip yields a visibility of 64 %, which corresponds to a visibility of 96 % relative to the ideal.

so the experimenter has to ensure their indistinguishability in every degree of freedom. To “erase” the identity of the photons due to different spectral modes, narrow-band interference filters with FWHM $\Delta\lambda=3$ nm, centered at 820 nm, were placed in front of the detectors, stretching the coherence length⁴ of the photons to $l_c \approx 150 \mu\text{m}$. Additionally, to ensure that both input photons perfectly interfere at the central PPBS, the preparation waveplates (see Fig. 3.2 and Table 4.1) were set to prepare horizontally polarized light⁵ and the input fiber couplers have been aligned so that both input beams spatially overlap at the PPBS to the highest degree possible⁶. One of the harder parts in the experiment is to guarantee that the input photons arrive at the beamsplitter at the same time so that there is no temporal mode-mismatch between them. As already outlined in Section 2.2.1, the observed coincidence rate after a beamsplitter is a function of the temporal delay between the two photons which manifests itself in the well-known **Hong-Ou-Mandel-Dip** (see Fig. 2.6). By slightly varying one of the two down-conversion path lengths, this dip can be reproduced, indicating the ideal path length at the low point of the dip. We realized

⁴This effect also facilitates the temporal mode-matching, as discussed below. Generally the coherence length l_c of pulsed laser light is roughly given as $l_c \approx \frac{\lambda^2}{\Delta\lambda}$

⁵This is important, since V-polarized light is perfectly reflected by the PPBS and therefore can’t interfere.

⁶To ensure perfect interference, the input beams have to perfectly overlap on the PPBS as well as after the beamsplitter. A visible diode laser at 670 nm coupled into the single mode fibers has been used to walk the input fiber-couplers in such a way, that, when their intensities were matched, classical interference could be observed at the output of the PPBS.

		$ H\rangle$	$ V\rangle$	$ D\rangle$	$ A\rangle$	$ R\rangle$	$ L\rangle$
Input 1	HWP 13	34° 17'	79° 17'	56° 47'	11° 47'	34° 17'	79° 17'
	QWP 3	96° 35'	96° 35'	141° 35'	141° 35'	141° 35'	141° 35'
Input 2	HWP 15	6° 59'	51° 59'	29° 29'	344° 29'	6° 59'	51° 59'
	QWP 2	14° 22'	14° 22'	59° 22'	59° 22'	59° 22'	59° 22'

Table 4.1.: Individual waveplate settings to obtain the input states for the tomography experiment according to the waveplate calibration.

this by placing one of the fiber couplers (FC2) onto a pico-motor-driven translation stage, which was controlled via the Newport motion controller. The outcome of the HOM-Dip search with H-polarized input photons can be seen in Fig. 4.2. The *visibility* or “depth” of the dip is governed by the degree of indistinguishability between the photons and is therefore a good measure for the quality of the non-classical interference. It is important to note at this stage that, since the PPBS have the feature of reflecting H-polarized light with probability 0.28, the maximum achievable visibility⁷ in our case is 67 %.

We achieved a total visibility of 64 %, corresponding to a visibility of 96 % relative to the ideal, indicating good indistinguishability of the input photons. To check whether the PPBSs are working accordingly, we also performed a HOM-Dip-Search in $|VV\rangle$, i.e. with V-polarized photons entering the CSIGN-gate. As expected, there was no noticeable HOM-Dip contribution in $|VV\rangle$, suggesting that the PPBSs really reflect all of the incident vertically polarized light.

4.2. Quantum Process Tomography of the Gate

Quantum process tomography that describes the action of a quantum system (in our case, the CSIGN-gate) consists of state tomography performed for a complete set of input states. To be able to reconstruct the process matrix χ , all possible permutations of the output states (i.e. $|HH\rangle$, $|HV\rangle$, ...) have to be measured for every input state. While a certain set of 16 measurements would already be sufficient to perform state tomography, all 36 permutations of the output states $|H\rangle$, $|V\rangle$, $|D\rangle$, $|A\rangle$, $|R\rangle$, $|L\rangle$ have been measured. This allows one to sort the collected data into complete sets of POVMs, which can be then normalized on a small scale (after 4 measurements, e.g. $|HH\rangle$, $|HV\rangle$, $|VH\rangle$, $|VV\rangle$). If one chose only 16 measurements instead, this normalization would run over the whole set, and fluctuations in count rates due to air-conditioning cycles⁸ (on the time-scale of

⁷In our case, the visibility is defined as $V = \frac{C_{out} - C_{dip}}{C_{out}}$, where C_{out} denotes the coincidence countrate outside of the dip and C_{dip} is the measured countrate at the low point of the HOM-Dip. The relative visibility V_{rel} is given by $V_{rel} = \frac{V}{V_{ideal}}$.

⁸Previous experiments have shown that temperature fluctuations due to the air-conditioning cycles influences the detectors, resulting in slight variations of the count rates.

Output	$ H\rangle$	$ V\rangle$	$ D\rangle$	$ A\rangle$	$ R\rangle$	$ L\rangle$
HWP	0°	45°	22.5°	67.5°	0°	45°
QWP	0°	0°	45°	45°	45°	45°

Table 4.2.: Waveplate settings (not incorporating the calibration) for preparing and measuring the states $|H\rangle$, $|V\rangle$, $|D\rangle$, $|A\rangle$, $|R\rangle$, $|L\rangle$. Note that due to the order of the waveplates (HWP before QWP), if the photon is prepared (measured) in the state $|D\rangle$ ($|A\rangle$), the QWP has to be rotated as well (to $\pm 45^\circ$), since otherwise circular polarized light would be created.

30 minutes) would affect the data. To facilitate the data collection (576 measurement settings correspond to 576 different waveplate settings!), a LabView routine was written and employed that would perform a complete state tomography (36 measurements). So only the 16 input states had to be set manually, therefore speeding up the data collection tremendously. The routine executes as follows: After the input states have been prepared manually according to Table 4.1, the routine automatically rotates the analyzer waveplates in front of Detector 1 & 2 to measure the output states according to Table 4.2, starts the counting module and records the coincidence counts for a prior specified integration time (between 10 and 30 seconds), before moving the waveplates to the next measurement setting and saving the collected data after a complete run. The thus obtained data was then evaluated with a MatLab program that performs state tomography with the maximum-likelihood technique as described in Section 2.4.1. This procedure was repeated for all 16 input states and the process matrix was reconstructed from the state tomography results again employing a MatLab code written by Alexei Gilchrist and Nathan Langford [35, 36].

5. Results & Discussion

This chapter is devoted to the results and contains a detailed discussion of the experimental tasks outlined in the previous chapter. To fully characterize the action of our CSIGN-gate, various measurements have been performed. I will start with the results for the so-called “truth table”, a very simple measure, followed by single and two-qubit state tomography, which finally allows us to reconstruct the process matrix of our gate by means of process tomography, the most complete method for characterizing the action of a quantum gate.

5.1. CNOT Truth Table

The simplest characterization of a two-qubit gate is based on its “truth table”. It is obtained by measuring the output states for every possible input state within a single basis. It provides a quick estimate whether the gate is working properly, although it is far from a comprehensive measure for the performance of a gate. Since the input states are qubits, they can also exist in arbitrary complex superpositions of the classical bit. Superposition states and thus the entangling properties of the CNOT-gate, however, may not be reflected by simply looking at its truth table.

Nevertheless, due to the simplicity of the measurement, we recorded a truth table for our gate operated as a CNOT. This can be achieved by inserting extra HWPs (at 22.5°) which perform Hadamard operations on the target qubits before and after the CSIGN-gate (input 2 in Fig. 3.2). A schematic depiction of the extension of our CSIGN-gate to a CNOT-gate can be seen in Fig. 5.1. The Hadamard operation was actually implemented using the preparation and analyzer waveplates, so physically, no additional waveplate was employed. Due to the architecture of the gate, only the horizontally polarized photons are able to interfere with each other and are therefore denoted as logic 1 state for the control mode (C_H) and logic 0 for the target mode (T_H). So the logic value compared to the polarization of the photons for the truth table read like: Control bit $\rightarrow |0\rangle = |V\rangle$, $|1\rangle = |H\rangle$; Target bit $\rightarrow |0\rangle = |H\rangle$, $|1\rangle = |V\rangle$.

The actual recorded truth table in terms of measured coincidence counts can be seen in Table 5.1. For the parts of the table that do not require any interference (control bit in logic 0), the so-called “transfer fidelity” is almost perfect (99%), while for the critical parts of the CNOT operation (control bit in logic 1) that relies on the non-classical interference, the transfer fidelity decreases to 75 and 79%, respectively. A graphical representation of the truth table can be seen in Fig. 5.2, with the population of the matrix elements denoting the transfer probability. While for a ideal CNOT gate this is

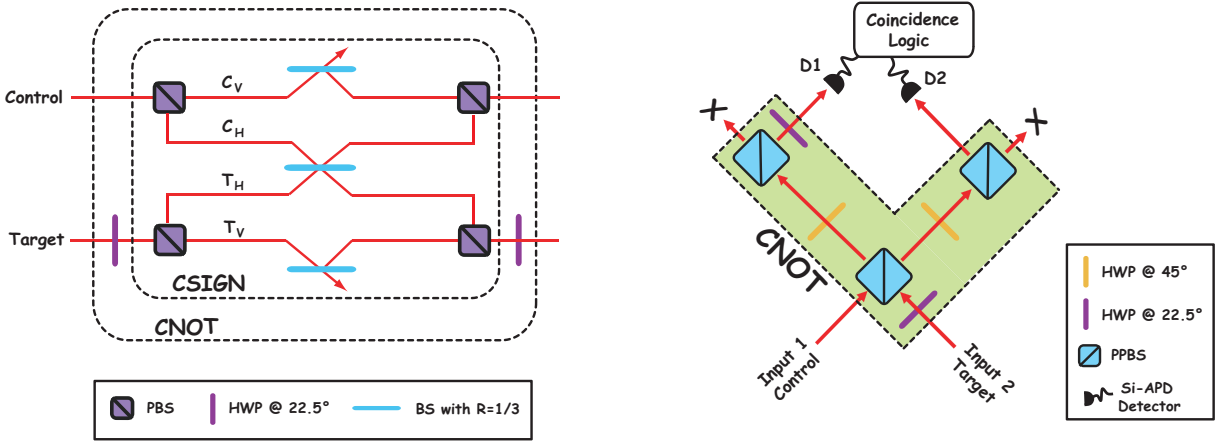


Figure 5.1.: Left: Schematic representation of the CSIGN-gate in the dual rail depiction and its extension to a CNOT-gate by applying Hadamard gates (HWPs at 22.5°) on the target qubit on either side of the gate.

Right: Experimental realization, where we do not show the preparation and analyzer waveplates.

straightforward, it is more complex to calculate the “optimal” CNOT truth table for the actual beamsplitter reflectivities. This has been done analogous to Section 2.3.1, but leaving the respective beamsplitter reflectivities as variables, so one arrives at the actual CSIGN matrix

$$CSIGN_{opt} = \begin{pmatrix} \sqrt{\eta_2\eta_3} & 0 & 0 & 0 \\ 0 & \sqrt{\eta_1\eta_3} & 0 & 0 \\ 0 & 0 & \sqrt{\eta_1\eta_2} & 0 \\ 0 & 0 & 0 & 2\eta_1 - 1 \end{pmatrix}. \quad (5.1)$$

By applying an Hadamard gate to the target qubit before and after the gate (Eq. 1.25), one can easily transform this into the appropriate CNOT matrix,

$$(I \otimes H) \cdot CSIGN_{opt} \cdot (I \otimes H) = CNOT_{opt}, \quad (5.2)$$

and when inserting the actual reflectivities, which were measured to be $\eta_1 = 0.28$, $\eta_2 = 0.28$ and $\eta_3 = 0.295$, one arrives at the following optimal CNOT truth table for our gate:

$$M_{opt} = \begin{pmatrix} 1 & 0 & 0 & 0 \\ 0 & 1 & 0 & 0 \\ 0 & 0 & 0.047 & 0.953 \\ 0 & 0 & 0.953 & 0.047 \end{pmatrix}, \quad (5.3)$$

where the individual entries of the truth table are calculated as $M_{opt}^{(jk)} = \langle k | CNOT_{opt} | j \rangle$, with $(j, k \in \{00, 01, 10, 11\})$. The optimal truth table together with the ideal and measured truth table is shown in Fig. 5.2. From this matrices, one can calculate the so-called “Inquisition” [34], which is the average of the logical basis fidelities.

IN ↓ OUT →	00⟩	01⟩	10⟩	11⟩	%
00⟩	299	0	1	1	99 ± 6
01⟩	2	278	2	0	99 ± 6
10⟩	1	4	129	514	79 ± 4
11⟩	3	1	492	161	75 ± 5

Table 5.1.: Experimentally measured truth table for the CNOT-gate. The furthest right column gives the “transfer fidelity” for every given input state. If the input control bit is in the logical |1⟩ state, the target bit gets flipped in 75 and 79 % of the cases. The coincidence counts were recorded for an integration time of 20 seconds and the background is already subtracted. The error has been calculated by propagating Poissonian count statistics.

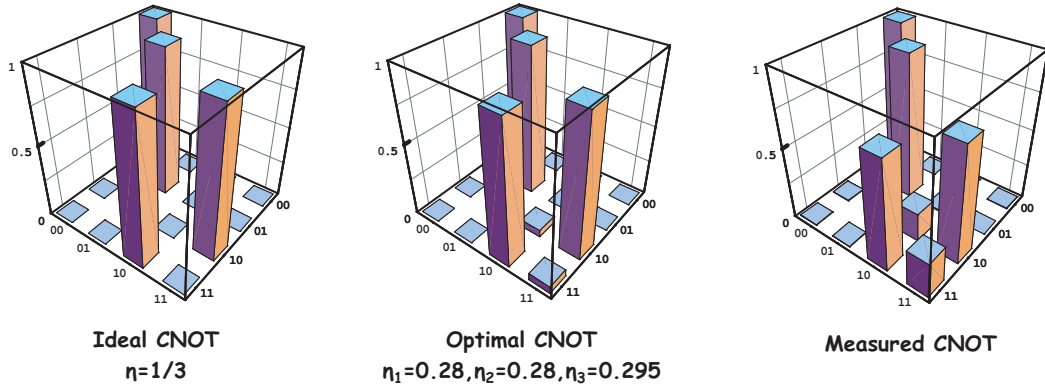


Figure 5.2.: Left: Ideal truth table for a CNOT-gate, where the whole population of the |10⟩ and |11⟩ input gets transferred in the |01⟩ and |10⟩ mode, respectively.

Middle: Best possible, or “optimal” truth table for our CNOT-gate, where due to the imperfect PPBS splitting ratios, only 95.3 % of the |10⟩ and |11⟩ inputs can get transferred in a perfectly aligned setup.

Right: The actually measured truth table for our CNOT-gate. If the input control bit is in the logical |1⟩ state, the target bit gets flipped in 75 and 79 % of the cases. Compared to the best achievable case (middle figure, 95.3 %), this is in excess of 90 % relative inquisition in between the optimal and measured CNOT truth table.

The inquisition is defined as $\mathcal{J} = \text{tr}(M_{exp} \cdot M_{ideal}^T)/4$ for the ideal case, where M_{exp} denotes the measured truth table. This changes to the general expression

$\mathcal{J} = \text{tr}(M_{exp} \cdot M_{opt}^T)/\text{tr}(M_{opt} \cdot M_{opt}^T)$ if one wants to calculate the overlap between the optimal and the experimentally measured truth table. While the inquisition of the measured data with the ideal CNOT-gate truth table is only 87.9%, this value is increased up to 90.6 % when taking into account the imperfect beamsplitter reflectivities. Theoretically, a inquisition of 97.7 % compared to the ideal is possible with the imperfect beamsplitter reflectivities.

OUT ↓ IN →	$ HH\rangle$	$ HV\rangle$	$ VH\rangle$	$ VV\rangle$
$ H\rangle$	681	155	4	0
$ V\rangle$	3	1	150	155
$ D\rangle$	343	77	75	68
$ A\rangle$	352	80	77	71
$ R\rangle$	371	76	76	70
$ L\rangle$	339	71	65	72

Table 5.2.: Count rates for the single qubit tomography of the first input photon, performed with PDC photons and 10 sec integration time. As expected, the state of the photon is well polarized, with the superposition state measurements $|D\rangle$, $|A\rangle$, $|R\rangle$, and $|L\rangle$ showing balanced count rates within Poisson distributed fluctuations. The increased count rates for the $|HH\rangle$ input is due to the setting of the HWP in between the PPBSs (set to 0° , therefore strongly attenuating vertically polarized photons).

5.2. Single-Qubit Tomography

State tomography, as has been explained before, is the process of reconstructing the quantum state of a system using a finite set of measurements. In our case, where the qubits are encoded in the polarization state of the photons, this simply reduces to a measurement of the polarization state. Even more straightforward, in the case of a single qubit, tomography is equivalent to measuring the polarization state of the photon via the four Stokes' parameters, which practically correspond to measurements in the H, V, D and R basis [32].

In our experiment, we performed single-qubit tomography for both input photons. This allowed us to check whether the gate induces some sort of polarization rotation from misaligned or incorrectly calibrated waveplates or beamsplitters. It also served as a first test for our LabView routine which automates the measurement procedure. When removing the polarizer (PBS) in front of the detector in the optical path not under consideration, the detector in that arm basically records every incident photon, regardless of its polarization, and we therefore expect the light to be strongly polarized. Additionally, by removing the polarizer, only coincidence post-selected photons are recorded, reducing the experimental counting errors due to noise and/or dark counts.

The single-qubit tomography has been performed for all permutations of H and V as input states, i.e. $|HH\rangle$, $|HV\rangle$, $|VH\rangle$, $|VV\rangle$. The results¹ can be seen in Table 5.2 and are within the expected error bars given by the Poisson statistics. As can be inferred from the data, the light is well polarized, with calculated fidelity and purity $\text{tr}(\rho^2)$ of almost 1. A similar result has been obtained for the other optical beam path (second qubit), which

¹Since the LabView routine performs 36 measurements, corresponding to all possible permutations of $|H\rangle$, $|V\rangle$, $|D\rangle$, $|A\rangle$, $|R\rangle$ and $|L\rangle$, we manually added and normalized the actual recorded count rates for a given state. For example, for the $|H\rangle$ measurement of the first qubit, this means adding up the $|HH\rangle$, $|HV\rangle$, $|HD\rangle$, $|HA\rangle$, $|HR\rangle$ and $|HL\rangle$ contributions from the tomography (due to the missing analyzing polarizer in the other optical beam path).

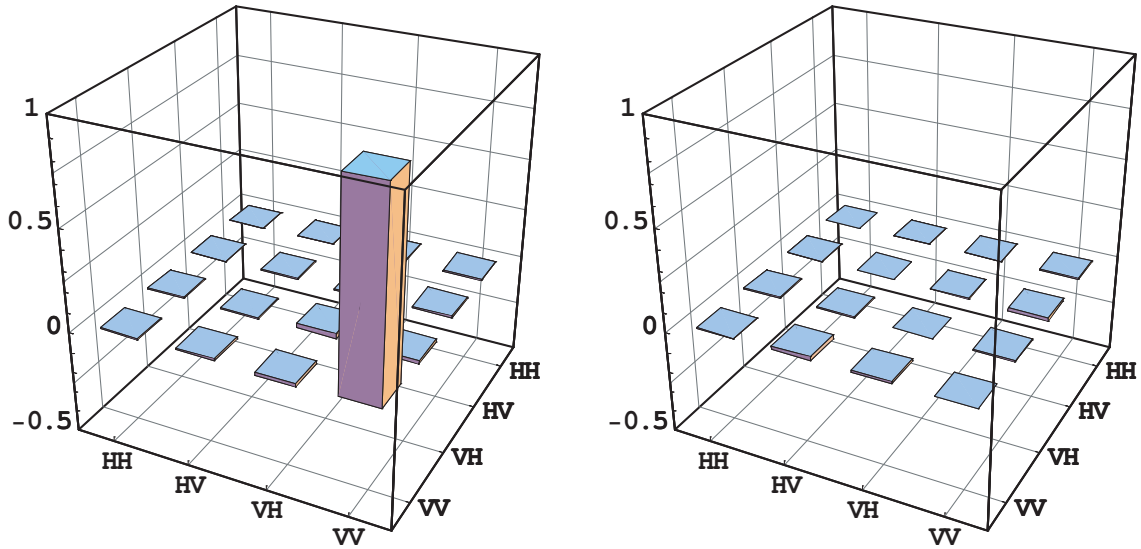


Figure 5.3.: Reconstructed density matrix from state tomography for $|VV\rangle$ input. The left graph represents the real part of the matrix while the right graph shows the imaginary part. Fidelity, purity, linear entropy and tangle of the reconstructed state are shown in Table 5.3.

Table 5.3.: State Tomography Parameters

Parameter	$ VV\rangle$ -Input	$ DD\rangle$ -Input
Fidelity	$0.973 \pm 1 \cdot 10^{-15}$	0.77 ± 0.01
Purity	0.949 ± 0.003	0.74 ± 0.01
Lin. Entropy	0.067 ± 0.004	0.36 ± 0.02
Tangle	$(3.6 \pm 3.4) \cdot 10^{-6}$	0.46 ± 0.03

demonstrates not only a working LabView routine and a proper alignment of the setup but also served as a controlled test before we finally perform quantum state and process tomography on our gate.

5.3. Two-Qubit State Tomography

Similar to the single-photon case, two-qubit state tomography is the measurement of the joint polarization state of a pair of photons. As outlined in detail in Section 2.4.1, this involves a series of at least 16 measurements, since the two-qubit Hilbert space is a four-dimensional space. We opted to perform “overcomplete” state tomography, using 36 instead of only 16 measurements for every one of the 16 input states, as explained in Section 4.2. Some of the results of the state tomography can be seen in Fig. 5.3 and 5.4, together with their respective parameters in Table 5.3. Those results have been chosen for publication here because they demonstrate very clearly the characteristics of our

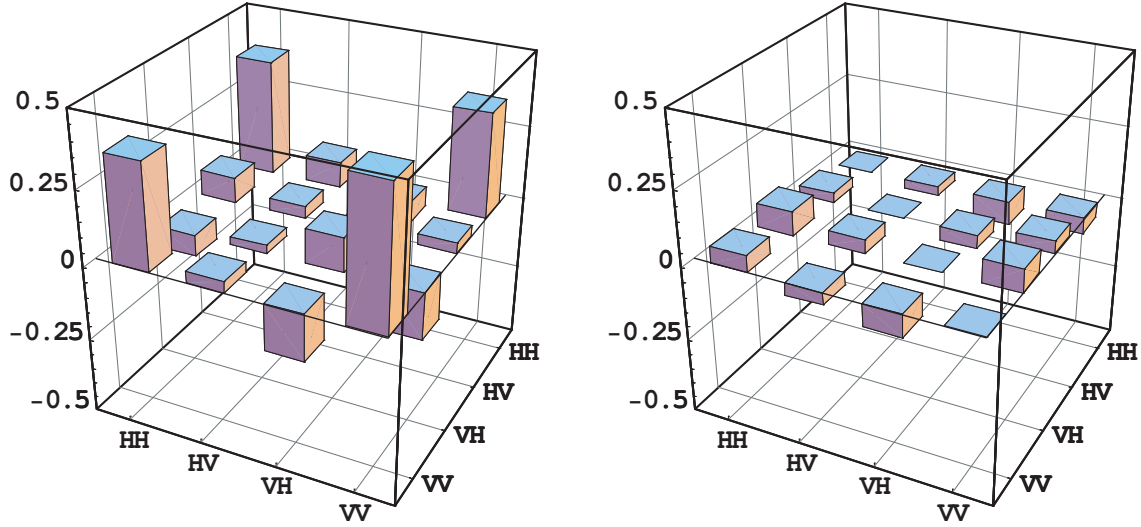


Figure 5.4.: Reconstructed density matrix from state tomography for $|DD\rangle$ input. The left graph represents the real part of the matrix while the right graph shows the imaginary part. Fidelity, purity, linear entropy and tangle of the reconstructed state can be inferred from Table 5.3. As expected, the $|DD\rangle$ input results in an entangled output state of the form $|HD\rangle + |VA\rangle$, which, after local unitary transformations ($I \otimes H$) is equal to the better known Bell-State $|\Phi^+\rangle = \frac{1}{\sqrt{2}}(|HH\rangle + |VV\rangle)$.

CSIGN-gate for the specific input states. For vertically polarized input states, $|VV\rangle$, the gate performs no transformation of the state, simply because the two photons do not interfere at the central PPBS, so one expects the output state to be of the form $|VV\rangle$ as well. This can be seen in Fig. 5.3 and Table 5.3. Purity² and tangle of the joint state are 0.949 ± 0.003 and effectively zero, respectively, indicating an unentangled and strongly polarized two-qubit state. The linear entropy is a measure for the mixture of a state and closely related to the purity (Eq. 1.16). All in all, the reconstructed density matrix shows a strongly vertically polarized output state of very high fidelity and no entanglement, as expected from theory (Section 1.2.2).

A more interesting input is the $|DD\rangle$ state, since we expect the gate to transform this input into a maximally entangled state, as desired for Bell-, GHZ- and cluster state preparation (Section 1.2.2 and 1.3.3). The reconstructed density matrix for the $|DD\rangle$ input is shown in Fig. 5.4 and the tangle has been calculated to be 0.46 ± 0.03 , which demonstrates the entangling action of our gate, albeit the entangled state is somewhat mixed with a linear entropy of 0.36 ± 0.02 . Unfortunately, the tangle is a very sensitive measure and to obtain a high figure, the quality of the optical setup (i.e. quality of

²The error has been calculated by performing a 100 run Monte-Carlo simulation of the state tomography, with Poissonian noise added to the count statistics in each run.

the mode match and optics elements) has to be extremely high. Apparently, since our crucial PPBSs fail to have this quality, the rather low tangle is not surprising and a more detailed discussion of this will follow at the end of this section. Nevertheless, the output state is sufficiently entangled to violate a Bell-inequality, with a maximum possible Bell-parameter [21] of $S = 2.39 \pm 0.02$, which is an encouraging result.

5.4. Process Tomography

To determine the action of our quantum gate we have to perform quantum process tomography, since state tomography only reconstructs the output state for a given input state, but doesn't allow one to predict the output state for any arbitrary input state, mixed or pure (Section 2.4.2).

Fortunately, the same set of data which was taken for the state tomography can readily be used to perform quantum process tomography. Since the usual approach, in some cases, gives unphysical process matrices, a new convex optimization method [36] has been developed, which can be thought of a constrained least-squares optimization that is similar to the maximum-likelihood estimation in QST [33]. Data evaluation was performed on a MatLab routine employing this new technique, and a graphical representation of the reconstructed process or χ -matrix in the Pauli basis can be seen in Fig. 5.5. An ideal CSIGN-gate can be written as a coherent sum of tensor products of Pauli operators acting on the control and target qubit respectively, leading to $U_{CSIGN} = \frac{1}{2}(I \otimes I + I \otimes Z + Z \otimes I - Z \otimes Z)$. The process matrix in Fig. 5.5 shows the populations and coherences between these Pauli operators which represent the action of the gate, where the sign of the coherences are related to the signs of the terms in U_{CSIGN} . One should keep in mind, that, due to the architecture of our gate, a bit flip is applied onto every qubit because of the HWPs between the PPBSs, which flip the polarization of every photon. This fact can be easily accounted for by applying the bit flip, $(X \otimes X)U_{CSIGN}(X \otimes X) = \frac{1}{2}(I \otimes I - I \otimes Z - Z \otimes I - Z \otimes Z)$, onto the Pauli operator representation, which then yields the correct basis for the process matrices shown in Fig. 5.5.

Given these results, we want to compare the experimentally obtained process matrix relative to the ideal matrix χ_{CSIGN} , which is the process matrix for U_{CSIGN} [34]. The *process fidelity*³ $F_P = \text{tr}(\chi_{CSIGN}\chi_{exp})$ between our measured and ideal CSIGN χ -matrix was calculated to be 0.77 ± 0.1 . The error was estimated by performing a 1,000 run Monte-Carlo simulation of the whole process tomography, with Poissonian noise added to the count statistics in each run. Unfortunately, to date, there exists no other, more straightforward technique to calculate the error bars. In Fig. 5.5 it is clear that the major deviation from ideal operation is the larger than expected II term (0.31 compared to 0.25 in the ideal case). This arises from imperfect mode matching at the

³A graphical representation of F_P can be obtained by acting U_{CSIGN} on all the Pauli basis elements (therefore expressing it in the CSIGN basis). In that case, F_P is the height of the corner element II.

5. Results & Discussion

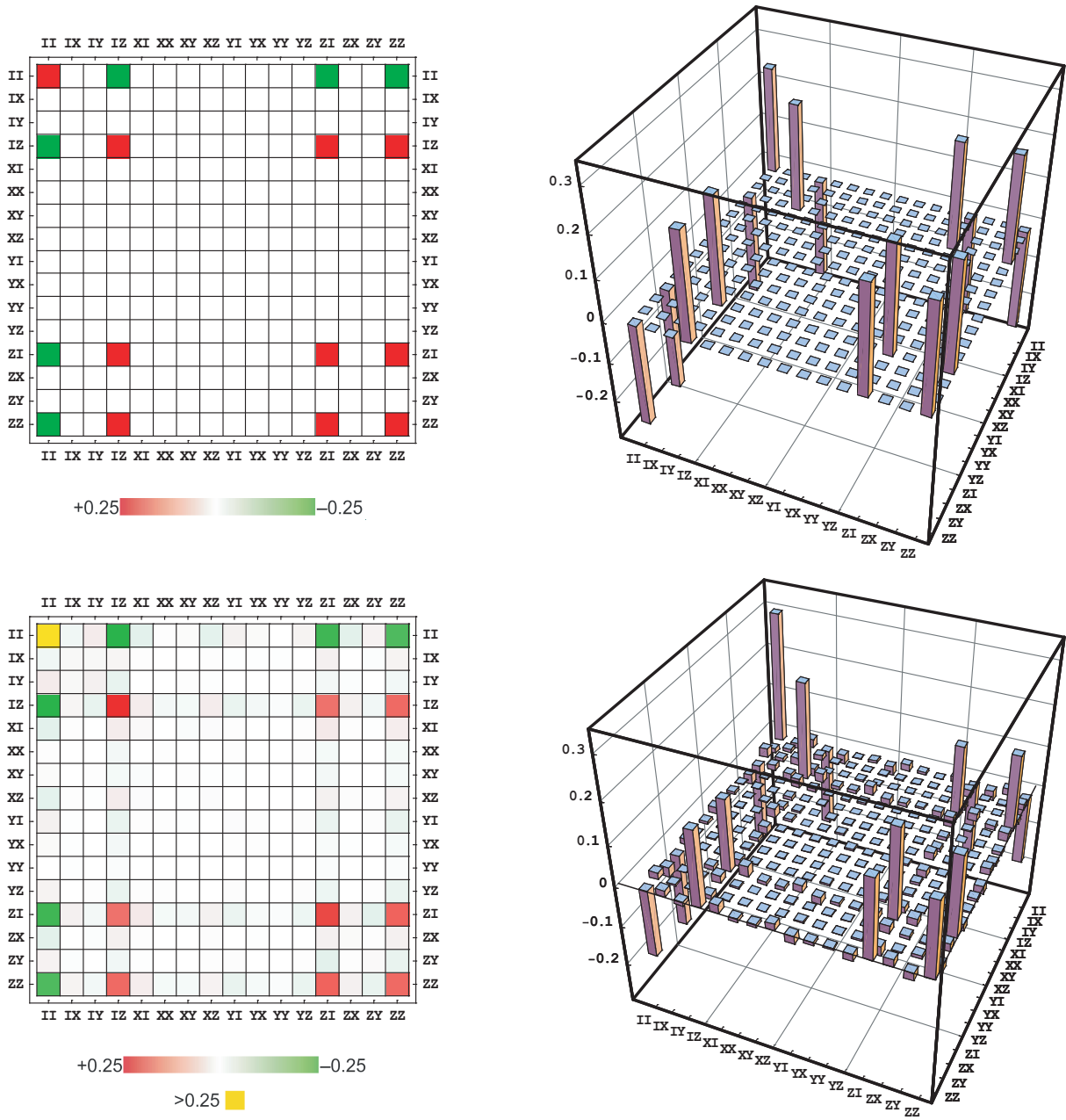


Figure 5.5.: The real part of the ideal (top) and measured (bottom) χ -matrix for the CSIGN-gate in the basis defined by tensor products of Pauli operators. The colour denotes the population of the matrix elements. The imaginary components of the experimental matrix are not shown: a few populations are on the order of 0.05, the majority is ~ 0.005 .

central PPBS, resulting in imperfect nonclassical interference, i.e., the control and target qubits do not see each other and are simply transmitted through the circuit unchanged.

An alternative approach to the process fidelity is to calculate the *average gate fidelity*, i.e. the average overlap of the predicted output states with the measured output states (from the individual state tomography results), which is the average of the usual state fidelity defined as $F(\rho, \sigma) = (\text{tr} \sqrt{\sqrt{\sigma} \rho \sqrt{\sigma}})^2$, where ρ, σ are the density matrices under consideration. This measure gives an overlap of 0.82 ± 0.1 for our gate. However, our experimental set-up systematically induces fixed rotations of the input and output polarizations⁴. For practical application of this gate, these rotations have no detrimental effect because they can be measured and compensated for by appropriate single-qubit rotations. By numerically modeling these local single-qubit unitary operations on both control and target input and outputs we could increase the process fidelity to 0.80 ± 0.2 and the average gate fidelity to 0.84 ± 0.1 . This represents the optimum fidelity that can be achieved with our CSIGN-gate. The fact that the fidelity is still less than 1 is most likely due to the non-ideal PPBSs reflectivity and the imperfect mode matching (spatial as well as temporal) at the central beamsplitter. This also leads to an imperfect “process purity”, which reflects the effects of decoherence on the gate. The process purity is defined as the purity of all output states averaged over all pure inputs, $\text{tr}(\rho^2) = [d \cdot \text{tr}(\chi_{exp}^2) + 1]/(d + 1) = 0.74 \pm 0.1$ (d is the dimension of the Hilbert space, hence 4 in our case). This is equivalent to an average normalized linear entropy of 0.35 ± 0.1 , which is a measure for how much mixture the gate introduces.

5.5. Discussion

As one can judge by the results of the state and process tomography, the CSIGN-gate shows the right characteristics. It is capable of entangling previously unentangled photons and the process matrix shows a qualitative resemblance with the ideal CSIGN-gate. Still, the calculated properties like the gate fidelity are imperfect. Since we know that our PPBS splitting ratios are not perfect, we raise the question how well the gate can possibly perform with these beamsplitter reflectivities, not considering other potential imperfect experimental conditions like mode-mismatch and inherent noise in the optical setup. To investigate this question, one can try to model the gate with the actual beamsplitter reflectivities and, ideally, calculate the “optimal” χ -matrix for this gate and compare it to the experimentally-reconstructed process matrix. This has been done by Alexei Gilchrist, who simulated count rates for the CSIGN circuit with the actual PPBS reflectivities and performing process tomography, eventually resulting in an “optimal” χ -matrix that yields a maximum achievable process fidelity of $F_p=0.957$, which corresponds to an average gate fidelity⁵ of 0.965.

An alternate method to obtain an estimation of the optimal performance of the CSIGN-gate with the wrong PPBS splitting ratios is to calculate, and average over, the transfer fidelities for all possible input states. This is equivalent to the average gate fidelity described above and in our case we define the transfer fidelity as the overlap between the ideal and “real”

⁴This is most likely due to birefringent effects in the non-ideal PPBSs.

⁵ $F_{avg} = \frac{d \cdot F_p + 1}{d + 1}$, where d is the dimension of the Hilbert space, hence 4 in our case.

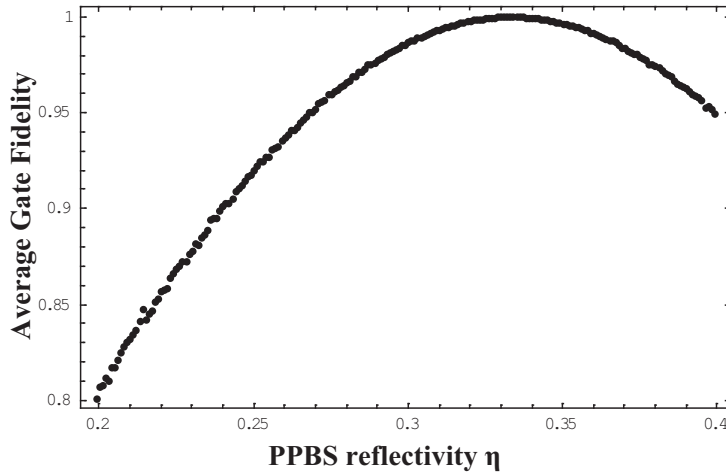


Figure 5.6.: The “average gate fidelity” $|\langle \Psi_{ideal} | \Psi_{real} \rangle|^2$ as a function of the general beamsplitter reflectivity η . As expected from theory, for $\eta=1/3$, the fidelity is 1. For our gate, the actual (average) beamsplitter reflectivity of $\eta=0.285$ gives an optimum average gate fidelity of 0.97.

output states of the gate, hence $F_{avg} = |\langle \Psi_{ideal} | \Psi_{real} \rangle|^2$, with $|\Psi_{ideal}\rangle = CSIGN|\Psi_{in}\rangle$ and $|\Psi_{real}\rangle = CSIGN_{real}|\Psi_{in}\rangle$ and the “real” CSIGN matrix is that of Eq. 5.1. One can then infer the average gate fidelity by calculating the transfer fidelity for all possible input states $|\Psi_{in}\rangle$, where $|\Psi_{in}\rangle = (a + ib)|HH\rangle + (c + id)|HV\rangle + (e + if)|VH\rangle + (g + ih)|VV\rangle$, which allows for mixed, pure and entangled input states. By repeatedly assigning normal distributed random values⁶ to the parameters $a-h$ and averaging over the results, one obtains the expected average gate fidelity. This simulates the gate performance for all possible input states. The calculation has been carried out on *Mathematica 5.0* and the result is plotted in Fig. 5.6, with the average gate fidelity being a function of the general beamsplitter reflectivity η . Following this approach we obtain an estimated optimum fidelity of about 0.97, better than originally expected, but in good agreement with the results of Alexei Gilchrist’s circuit simulation⁷.

Initially, we expected the wrong PPBS splitting ratio to be the main reason for the imperfect data. However, the results presented above suggests otherwise. Apart from the reflectivities of the beamsplitters, imperfect mode matching can be blamed for the non-ideal performance of the gate. Mode matching could, in principle, be improved with narrower spectral bandwidth filters and by ensuring better spatial as well as temporal overlap of the input photons at the central PPBS. The quality of the mode matching can be inferred by the interference visibility, i.e. the depth of the HOM Dip, which was in excess of 90% relative visibility (see Section 4.1.3). This can hardly be improved as

⁶In order to draw input states uniformly over the so-called Haar measure [39], we chose a normal distribution in *Mathematica 5.0*, with the mean equal to 0 and a standard deviation of 1.

⁷A more complete calculation considering the individual beamsplitter reflectivities has also been performed, yielding a result for the average gate fidelity of 0.969, essentially the same result as presented here.

it already presents a rather high figure compared to previous experiments, although we believe that during the (long) course of the tomography experiment the quality of the mode matching might have been declining due to sagging of the fiber couplers. Another possible explanation for the imperfect tomography data could be non-ideal waveplates, either slightly mis-aligned so that they cause beam-steering issues or not set correctly at the right angle (which can only be done to within ± 5 degree-minutes) as well as unusual phase-shifts occurring upon reflection of optical elements.

6. Problems & Possible Solutions

As every avid experimentalist knows, things tend to go wrong. This experiment is by far no exception from this tendency, but instead of whining and complaining, one has to tackle the obstacles encountered in the best way possible. Throughout the experiment we have been struggling with low coincidence count rates, so this section is mainly dedicated to the PDC-source and gives suggestion of how to improve its efficiency.

6.1. Adding in that 3rd Photon

To be able to create a 3-photon cluster state, we obviously have to incorporate a third photon, a weak coherent state in our case, into the optical setup. While coupling and aligning the coherent state, which is the remaining unconverted fundamental from the up-conversion process (see Section 3.2), in principle does not present major difficulties, matching the count rates of the PDC source and the coherent state would lead to unfeasible low 3-fold coincidence rates at the present time. Ideally, one only wants 3-fold coincidence contributions from 2 PDC photons and 1 coherent photon (i.e. “ $P_{CC} \cdot P_{1C}$ ”). However, the leading order background comes from the events where 2 coherent and 1 single PDC photon are detected after the gate ($P_{2C} \cdot P_{1S}$), so simply increasing the coherent state count rate to ensure high 3-fold probability is not enough. Since the probability for a coherent state containing two photons scales with the intensity squared $P_{2C} \propto I^2$, we have to keep the intensity of the coherent beam low enough to ensure a moderate and low background. This investigation shows that the probability¹ for a coherent state containing one photon, $P_{1C} \sim |\alpha|^2$, has to be much smaller than the so-called down-conversion-efficiency ε ,

$$\begin{aligned} P_{1S} &= \frac{P_{CC}}{\varepsilon} \quad , \quad P_{2C} = \frac{P_{1C}^2}{2} \\ P_{1S} \cdot P_{2C} &\ll P_{CC} \cdot P_{1C} \\ |\alpha|^2 &\ll \varepsilon \end{aligned} \tag{6.1}$$

where $\varepsilon = \frac{CC}{S}$, with CC and S are the measured coincidence and singles count rates after the gate, respectively.

Having said that, if one wants to achieve reasonable 3-fold count rates for the creation of the 3-photon cluster state, one has to improve the currently low rate of coincidences of our down-conversion source, which stands at a mere 300 s^{-1} ($\varepsilon \approx 0.025$)

¹Remember that a coherent state is defined as $|\alpha\rangle_c \propto |0\rangle + \alpha|1\rangle + \frac{\alpha^2}{\sqrt{2}}|2\rangle + \dots$, where $|\alpha|^2$ is the probability of the state containing one and only one photon.

after the gate. This figure has to be improved significantly to allow further progress of the experiment. Based on former experiments, it should in principle be possible to achieve $\varepsilon = 0.1$ with an improvement by a factor of 10 from the current value being the minimum. The next section will tackle this task and we will give some suggestions of how to upgrade the source therein.

6.2. Coincidence Rate Improvement

Different ways to improve the efficiency of a down-conversion source exist and it is in fact not straightforward to choose the appropriate one. However, in the following, I will try to briefly discuss the various approaches.

In order to obtain a decent down-conversion efficiency in the first place, one has to ensure a proper up-conversion at the SHG-crystal to achieve intensities as high as possible for the subsequent down-conversion process. Unfortunately, due to pulse broadening, the crystal length has to be kept below 2 mm to achieve sufficiently short pulses, so increasing the length of the doubling crystal beyond that value (and hence increasing the up-conversion probability) is not preferred. As a next step, different lenses with different focal lengths can be employed to focus the pump pulse onto the crystal. In theory, the Rayleigh length should be no shorter than the crystal length, but it certainly helps to test lenses in the region of $f=25-50$ mm for optimal focusing. However, there is a trade-off between the “acceptance-angle” within which down-conversion in the crystal occurs and optimal focusing to achieve high beam intensities (and therefore a high conversion probability). In principle, the tighter the focus, the larger the divergence angle, which under extreme circumstances can result in a worse up-conversion-efficiency because only parts of the beam satisfy the phase matching conditions.

Another possible solution is the use of higher quality lenses, so-called achromats, which are in fact a combination of multiple lenses and therefore do not lead to chromatic and spatial aberration effects, allowing for a better focus. In order to collimate the beam properly after the SHG-crystal, a combination of two cylindrical lenses could be employed to ensure a circular beam shape with Gaussian intensity distribution, which could be inspected and verified in-vivo with the help of the CCD camera.

Additionally, the fast prisms currently used to spatially separate the second harmonic from the fundamental frequency might also introduce the effect of temporally delaying the various pump pulse frequencies differently, therefore leading to pulse broadening. By utilizing a combination of multiple dichroic mirrors it should be possible to circumvent this problem.

During the alignment of the pump source we have also come aware of the following problem: Since the SHG-crystal is cut such that the incident pump beam has to be perpendicular to its surface for optimal phase matching, back reflection from the crystal

front face travels back into the laser cavity and forces the Tsunami Ti:Sapphire to jump out of its mode-lock operation whenever one tries to achieve better phase matching by tilting the crystal. To avoid this problem, SHG-crystals which are cut to an angle 5° of the ideal have been ordered, so that for perfect phase-matching conditions, the back reflected light will not be back-coupled into the laser cavity. Trials with such crystals already yielded conversion efficiencies of more than 40 %, a significant improvement over the current value of 26 %.

Last but not least, mode-matching calculations and expertise show that improved fiber coupling can be expected by rigorously shortening the arm lengths in between the fiber couplers and the PDC-crystal, so that no additional lenses have to be employed to focus the beam onto the fiber core, as currently done. Additionally, a new set of different fiber couplers have been ordered which are better mounted and less prone to long term drag and temperature fluctuations within the laboratory. In a last incentive, the single mode fibers will be extended to pieces of 2x2m in each arm, which allows to shine a visible laser light back through the fiber coupler onto the crystal, which then in turn ensures easy, quick and proper alignment of the fiber couplers.

7. Outlook

Once the down-conversion source has been improved, a range of possible experiments have been suggested, most notably the generation of a 3-photon cluster state. While the gate architecture therefore is already set up, a slight modification and an upgrade to a 4-photon source would enable fascinating new experiments such as an implementation of Shor’s algorithm or the possibility to perform feed-forward quantum computation (quantum control).

7.1. 3-Photon CSIGN-gate

As we have already seen theoretically in Section 2.3, it is possible to concatenate the basic CSIGN-gate to create a 3-photon cluster state. Even more interestingly, the unique scheme first suggested by Ralph [14] can be potentially scaled up to create a N-photon cluster state by concatenating (N-1) CSIGN-gates. Experimentally, this “upgrade” can be achieved by adding another PPBS¹ with the same reflectivity to the network for each additional photon, as depicted in Fig. 7.1. For every other photon, only two HWP, one QWP and one PPBS have to be added to the previous gate, which is one of the main advantages of this scheme².

For three photons, this has already been setup in the lab, and once path length matching and mode matching at the second PPBS has been achieved, the gate could be operational. To characterize its performance however, a 3-fold coincidence logic has to be installed, either by ordering programmable coincidence logic (Xilinx) or by simply concatenating two ordinary TAC-SCA’s, where the coincidence output of the first logic serves as a input signal for the second TAC-SCA, together with the signal for of the third photon. In addition, the current program for the automated state tomography would need to be adapted and expanded to incorporate the third photon, before the 3-photon CSIGN-gate can be characterized in the same way as has been done for the basic 2-photon CSIGN-gate. If successful, this would be the first generation of three-photon entanglement from previously unentangled photons.

¹This extra PPBS actually just serves the fact to balance the amplitudes for the additional qubit, so no non-classical interference is required there.

²One HWP and QWP are used for input state preparation. One HWP, set to swap the polarization, and the extra PPBS are required to balance the gate’s output amplitudes.

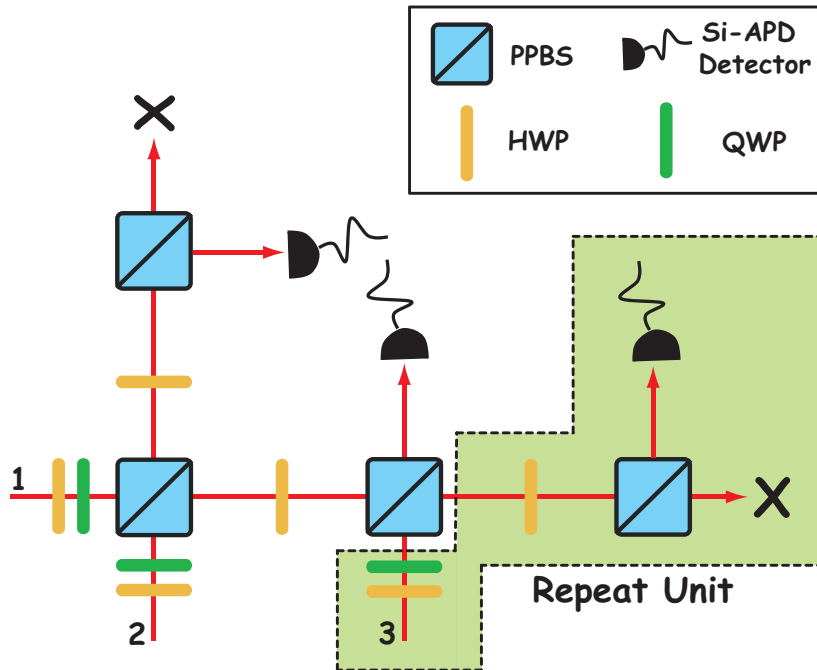


Figure 7.1.: Extension of the basic CSIGN-gate architecture to produce 3-photon cluster states. Potentially, a N -photon cluster state can be created by adding the repeat unit to the previous gate for each extra photon. The repeat unit consists of one PPBS, two half-waveplates, one quarter-waveplate and one detector.

7.1.1. Test of Svetlichny's Inequality

Svetlichny has developed a Bell like inequality which allows to distinguish between genuine three-particle non-locality and two-particle non-locality with a separable third particle [40]. Adapted to linear optics by Mitchell *et al.* [41], it has so far not been successfully implemented or tested, mainly due to the fact that a violation of this inequality requires a high level of three-particle entanglement. However, once the 3-photon CSIGN-gate is characterized and optimized past the required critical fidelity, the test of Svetlichny's inequality is very straightforward as the measurements can be performed analogous to the measurements for the state tomography³.

7.2. 4-Photon Source

Ultimately, in order to perform more interesting quantum computing experiments such as implementing Shor's algorithm or quantum control schemes, the current photon source has to be upgraded to generate four photons. Since the scale up probability is not favorable for the case of adding two coherent states to the PDC-source, eventually, the four photons have to be emitted by two PDC-events. Basically, two different methods for collection of these

³Only the waveplates would have to be set to the appropriate angles to conduct the experiment.

photons can be employed. One can either collect one mode as done in our experiment and wait for two PDC events to happen at the same instance (so-called “double pair emission”), or alternatively, collect two different modes (four spots on the opening cone) which is not possible with the current collapsed cone operation. The disadvantage of the first scheme is that the double pairs are obviously emitted into the same mode (2x2 photons), so one has to employ 50/50 beamsplitters to probabilistically separate them into 4 distinct modes, losing 75 % of the 4-photon events on the way. Since the probability for 4-photon generation is the same in both cases, it is more favorable to collect two different modes, although certainly more challenging to achieve experimentally. However, other research groups have achieved 4-photon count rates as high as 1 s^{-1} utilizing the latter scheme.

7.2.1. Implementation of Shor’s Algorithm

One of the prime goals of experimental quantum computation is the implementation of Shor’s Algorithm [5]. Its ability to find the prime factors of an (large) integer in only a fraction of the time of a classical computer is very fascinating. Concatenating two CNOT-gates and using four photons it might be feasible to demonstrate the algorithm, although only a restricted set of problems could be solved with it [42]. This can be done by extending our current scheme to 4 photons and although the experimental realization is probably months away, it deserves to be mentioned here.

7.2.2. Quantum Control

Another very fascinating and currently emerging topic in the field of linear optics quantum computation is quantum control, which involves the already mentioned feed-forward. By utilizing , e.g. fast switching Pockels-cells, one can manipulate (i.e. rotate the polarization of) one or more photon(s) upon the result of a previous measurement of another photon. This makes the implementation of more sophisticated algorithms possible and eventually allows for deterministic quantum computing. A preliminary characterization of a fast feed-forward system is already underway in our laboratory.

8. Further Investigation

8.1. Motivation

In summary up to now, we have proposed and experimentally demonstrated a new architecture for an entangling optical gate. The key advantage of this new gate architecture is its simplicity and suitability for scaling since it requires only one nonclassical mode matching condition, and no classical interferometers. The performance of this gate is limited almost exclusively by mode matching, primarily spatial, making this gate a very promising candidate for micro-optic and integrated-fiber-optic implementations, where non-classical mode matching in excess of 99% can be expected [43]. Due to the less stringent (spatial) mode matching requirements in fiber optics, improved versions of these gates can, in principle, be expected within the next few years.

One of the last remaining problems will then be the temporal mode matching at the central PPBS, since good spectral mode matching is guaranteed by employing narrow bandwidth filters and the state of polarization can be very easily and accurately manipulated inside optical fibers.¹

The importance of temporal mode matching is by far not constrained to this particular experiment. Indeed it does presents a major challenge in almost every “real world” application of quantum communication (QC) protocols which require the experimental implementation of a so-called Bell-state measurement (BSM). This BSM was first suggested in Ref. [48] and subsequently realized by Mattle *et al.* [50] in a quantum dense coding experiment. Quantum teleportation [45, 52] and eventually a quantum repeater [47, 46, 49] furthermore rely on this specific measurement as will be discussed below.

Driven by the curiosity whether quantum repeaters can ever be implemented on a world wide scale (i.e. outside the perfect laboratory environment) and whether the performance of our CSIGN-gate will be limited by imperfect temporal mode matching, we have set up an experiment at the University of Vienna to study the performance of quantum teleportation dependent on the quality of the temporal mode (mis-)match. As a measure for the performance we examine the fidelity of the teleported state which itself depends on the temporal overlap of the photons and their general indistinguishability on a linear optics element, i.e., a beamsplitter. The mode matching is experimentally limited in “real world” long distance QC schemes due to polarization drifts and fluctuations in the length of optical fibers.

¹Very interestingly, in a recent publication [44], it has been shown that mode-mismatch that occurs in multiple degrees of freedom is completely equivalent to mode-mismatch in a single degree of freedom (e.g. temporal).

8.2. Quantum Teleportation

In 1993 Bennett, Brassard, Crépeau, Jozsa, Peres and Wootters [45] came up with a quantum teleportation scheme that is illustrated in Fig. 8.1.

The basic idea in quantum teleportation is the following: Suppose we have two parties, Alice and Bob. Say Alice wishes to transfer a certain quantum particle (a qubit, as in Eq. 1.1) to Bob, but cannot do so directly. According to the rules of quantum mechanics if she measured the qubit this action would destroy the quantum state of the particle without revealing her all the necessary information which she could then send to Bob to reconstruct the qubit. Still, if Alice would manage to have many identical copies of her particle to be teleported, she could, at least in principle, measure each of them and so, asymptotically, extract all the necessary information. Unfortunately, it is impossible to copy a unknown quantum state due to the so-called *No-cloning* theorem [51] that we will shortly describe in the following.

The No-cloning theorem

Very interestingly, as it will turn out, it is impossible to copy an unknown quantum state. Suppose we have a quantum copier with two slots labeled A and B , the *data slot* and the *output slot*, respectively. We start out by feeding the unknown but pure quantum state $|\Psi\rangle$ into the data slot, and we assume that the output slot is some standard² pure state $|p\rangle$, so that the initial state of the copier can be written as $|\Psi\rangle \otimes |p\rangle$. The copying procedure can be represented as some unitary evolution U , ideally,

$$|\Psi\rangle \otimes |p\rangle \xrightarrow{U} U(|\Psi\rangle \otimes |p\rangle) = |\Psi\rangle \otimes |\Psi\rangle. \quad (8.1)$$

Suppose now we want to copy two particular pure states, $|\Psi\rangle$ and $|\Phi\rangle$. Then the output of the copier should read like:

$$\begin{aligned} U(|\Psi\rangle \otimes |p\rangle) &= |\Psi\rangle \otimes |\Psi\rangle \\ U(|\Phi\rangle \otimes |p\rangle) &= |\Phi\rangle \otimes |\Phi\rangle \end{aligned} \quad (8.2)$$

Since this copying procedure is represented by an unitary transformation, it must preserve the inner product,

$$(\langle\Psi|\Phi\rangle) \otimes p = \langle\Psi \otimes p|\Phi \otimes p\rangle \xrightarrow{U} U(\langle\Psi \otimes p|\Phi \otimes p\rangle) = \langle\Psi \otimes \Psi|\Phi \otimes \Phi\rangle = \langle\Psi|\Phi\rangle\langle\Psi|\Phi\rangle, \quad (8.3)$$

so that we require,

$$\langle\Psi|\Phi\rangle = (\langle\Psi|\Phi\rangle)^2. \quad (8.4)$$

But this equation, $x = x^2$ has only two possible solution, $x = 0$ and $x = 1$, so either $|\Psi\rangle = |\Phi\rangle$ or $|\Psi\rangle$ and $|\Phi\rangle$ are orthogonal. Therefore the cloning apparatus can only clone or copy states which are orthogonal to one another! A quantum copier cannot, for example,

²much like blank paper sheets in a usual copier.

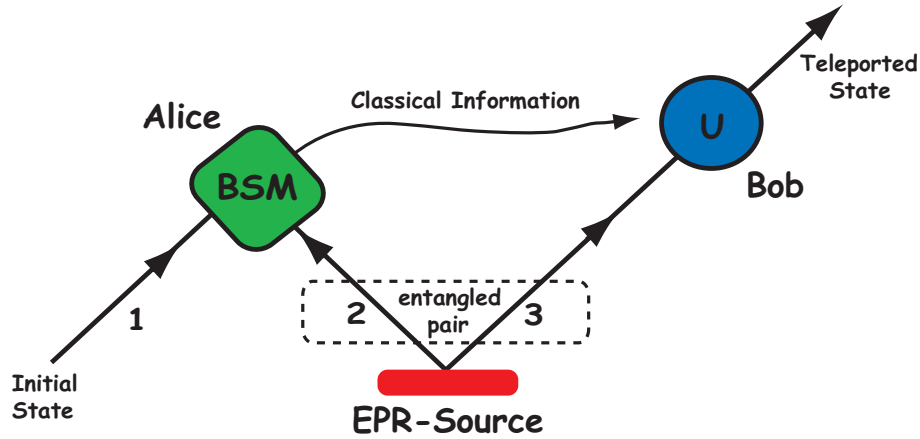


Figure 8.1.: Principle teleportation scheme of Bennett et al. [45]. According to the result of the Bell-state measurement (BSM), Bob performs a unitary transformation U to obtain the state of the initial particle/photon. More detailed discussion can be found in the text.

copy the qubit states $|\Psi\rangle = 0$ and $|\Phi\rangle = 1/\sqrt{2}$, since these states are not orthogonal and we have indeed shown that it is impossible to perfectly clone an unknown quantum state using unitary evolution. A more detailed and formal proof of this fact can be found in [51].

8.2.1. The Teleportation Protocol

But let us for now return to Alice and Bob and the question how Alice can provide Bob with her quantum particle. The solution is once again entanglement. By sharing a pair of entangled particles (EPR pair), Alice can *teleport* the unknown quantum state of her particle to Bob. The scheme of Bennett *et al.* [45] is applicable to all sorts of physical systems and degrees of freedom (i.e. arbitrary large Hilbert spaces), but we will from now on only consider two dimensional systems where the qubits are encoded in the polarization states of photons (i.e. H and V for the logic states 0 and 1).

As mentioned above, Alice and Bob share an entangled pair of particles (photons from now on), which, for the sake of simplicity, shall be in the singlet state,

$$|\Psi^-\rangle_{23} = \frac{1}{\sqrt{2}}(|H\rangle_2|V\rangle_3 - |V\rangle_2|H\rangle_3), \quad (8.5)$$

while the photon to be teleported is in an unknown superposition of H and V , $|\Psi_1\rangle = \alpha|H\rangle + \beta|V\rangle$. Recall from Section 1.1.4, that, as soon as one of the two entangled photons is measured (i.e. projected onto a certain state), the other photon has to be in the orthogonal state, independent of the chosen measurement basis.

In order to teleport her quantum bit, Alice now proceeds by performing a so-called Bell-state measurement (BSM) on photons 1 and 2. Although originally not entangled, the joint polarization state of photons 1 and 2 can always be expressed in terms of the four

Bell-states (Eq. 1.8), since these states form a complete orthogonal basis. In total, the state of the three photons can be written as

$$\begin{aligned} |\Psi\rangle_{123} &= |\Psi\rangle_1 \otimes |\Psi\rangle_{23} = \frac{1}{2} [|\Psi^-\rangle_{12} \cdot (-\alpha|H\rangle_3 - \beta|V\rangle_3) + |\Psi^+\rangle_{12} \cdot (-\alpha|H\rangle_3 + \beta|V\rangle_3) \\ &+ |\Phi^-\rangle_{12} \cdot (\beta|H\rangle_3 + \alpha|V\rangle_3) + |\Phi^+\rangle_{12} \cdot (\beta|H\rangle_3 - \alpha|V\rangle_3)]. \end{aligned} \quad (8.6)$$

Alice will randomly observe one of these 4 Bell-states, and as a result of Alice's measurement, Bob's photon 3 will be in one of the four corresponding states (see Eq. 8.6). So for example, if the result of Alice's joint measurement is the $|\Psi^+\rangle_{12}$ state, then Bob's photon will be found in the state $-\alpha|H\rangle_3 + \beta|V\rangle_3$. If Alice informs Bob on her measurement result (via a classical communication channel), then Bob can perform an appropriate unitary transformation U to obtain the initial state of photon 1, the particle to be teleported. Even more interestingly, if Alice observes the Bell-state $|\Psi^-\rangle_{12}$, then photon 3 on Bob's side is in the state $-(\alpha|H\rangle_3 + \beta|V\rangle_3)$, which is, except of an irrelevant global phase shift, already the initial quantum state of particle 1. The appropriate unitary transformations to the corresponding Bell-state measurements results are the following:

$$\begin{aligned} |\Psi^-\rangle_{12} &\longrightarrow \mathbb{I} \\ |\Psi^+\rangle_{12} &\longrightarrow \sigma_z \\ |\Phi^-\rangle_{12} &\longrightarrow \sigma_x \\ |\Phi^+\rangle_{12} &\longrightarrow i \cdot \sigma_y, \end{aligned} \quad (8.7)$$

with σ_x, σ_y and σ_z being single-qubit rotations as introduced in Section 1.2.1. The teleportation protocol still obeys the No-cloning theorem, since photon 1 loses its initial quantum state when it becomes entangled to photon 2 during the Bell-state measurement. If photon 1 itself belongs to an entangled pair, then this eventually leads to *entanglement swapping*. Both quantum teleportation and entanglement swapping have been experimentally realized in the past by various groups [52, 53, 54].

As we have seen in this section, the BSM plays an important role in the teleportation protocol, and indeed, in many other QC protocols such as dense coding and the quantum repeater. We will therefore now turn our attention to the device that experimentally performs this measurement, the Bell-state analyzer.

8.2.2. Experimental Bell State Analysis

The very essence of a Bell-state analyzer (BSA) is to perform a Bell-state measurement, i.e., to project the joint state of two particles onto the Bell basis. Unfortunately, it has been shown that a complete discrimination of all four Bell-states is not possible with linear optics alone [55], at least not for polarization encoded photons. Although a *non-deterministic* full BSA has been realized experimentally [56], we will only concentrate on the partial Bell-state analysis employed in this experiment. Note, however, that the ideal photonic BSA [57] is equivalent to the general CNOT-operation³ required for universal quantum computing.

³i.e. it can likewise entangle or disentangle qubits.

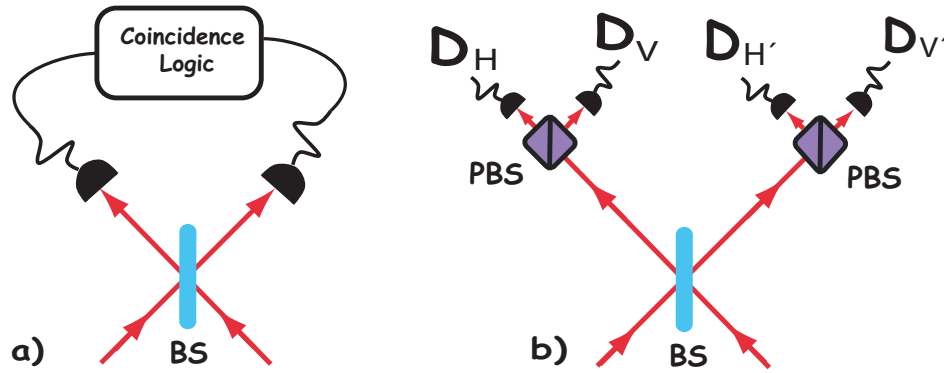


Figure 8.2.: Schematic of a Bell-state analyzer for photons. In **a)** coincidence detection leads to the discrimination of $|\Psi^-\rangle$ from the other Bell-states. In **b)** the schematic of a more complete Bell-state analyzer is shown. Coincidence between detectors D_H and $D_{V'}$ or between $D_{H'}$ and D_V indicates a $|\Psi^-\rangle$ state, while coincidence between detectors D_H and D_V or between $D_{H'}$ and $D_{V'}$ indicates projection onto a $|\Psi^+\rangle$ state.

In order to perform a successful projection onto the Bell basis, we have to superimpose the participating photons on a linear optics element. The most commonly used and by far most basic device therefore is the beamsplitter, which has been discussed in more detail in Section 2.2. As we have seen, the beamsplitter acts as a Hadamard gate on the photons, so that, if the two particles are indistinguishable with respect to all degrees of freedom, the photons will always exit together due to their bosonic nature (photon bunching, see Fig. 2.6). This is because for photons, the total state, which is comprised of the internal (polarization) state and the external (spatial) state, has to be symmetric⁴. Applying this rule to all four Bell-states we find

$$|\Psi^-\rangle_i|\Psi\rangle_a, \quad |\Psi^+\rangle_i|\Psi\rangle_s, \quad |\Phi^-\rangle_i|\Psi\rangle_s, \quad \text{and} \quad |\Phi^+\rangle_i|\Psi\rangle_s, \quad (8.8)$$

where the index i denotes the internal (Bell) state of the photons, while a and s indicate asymmetric and symmetric external (i.e. spatial) states. In other words, the antisymmetric $|\Psi^-\rangle$ state is the only one case in which the two photons emerge in different output modes after the beamsplitter and can therefore be detected by a coincidence measurement⁵. Applying this to the standard teleportation scheme above we immediately see that whenever we detect two spatially separated photons after the beamsplitter (in Fig. 8.2a)), photon 3 on Bob's side is immediately projected onto the initial state of photon 1 and no unitary transformation has to be performed by Bob. This has been the case in the Innsbruck experiment [52], but has the drawback that the teleportation only succeeds one fourth of the time. In our experiment, we employ the technique of *more complete* Bell-state analysis

⁴The total state of the photon is symmetric if and only if both the internal and external states of the photon are either symmetric or asymmetric.

⁵One can also argue that the spatially antisymmetric $|\Psi^-\rangle$ state is an eigenstate of the beamsplitter (Hadamard) operator, which can be shown by applying the operator on the external (spatial) state.

[50, 58], which is also the optimal efficiency that can be achieved using linear optics. The idea is that further distinction of the Bell-states is based on the fact that the two photons in the $|\Psi^+\rangle$ state carry opposite polarization in the H/V-Basis. By placing a PBS in each of the two output modes of a beamsplitter, one can post-select the $|\Psi^-\rangle$ and $|\Psi^+\rangle$ states upon a proper coincidence measurement after the PBS (see Fig. 8.2b)). While coincidence between detectors D_H and $D_{V'}$ or between $D_{H'}$ and D_V indicates a $|\Psi^-\rangle$ state, coincidence between detectors D_H and D_V or between $D_{H'}$ and $D_{V'}$ indicates projection onto a $|\Psi^+\rangle$ state.

9. The Teleportation Setup

In this Chapter I give a brief and basic outline of the experimental setup that was used to study the effect of temporal mode-mismatch on the fidelity of the teleportation protocol. As I have done in Chapter 3, I will divide the setup into its basic components and address them in more detail as we go along. In contrast to the previous CSIGN-gate experiment we now have to deal with 4-photons, whose simultaneous generation and detection require a more sophisticated experimental setup and additional electronics. A schematic representation of the setup is shown in Fig. 9.2.

9.1. Laser

As mentioned in the previous section, we are interested in the 2-photon interference behaviour of photons impinging on a beamsplitter which can act as a Bell-state analyzer. To allow for this quantum interference effect, the arrival time of the photons has to be chosen so that they mutually overlap on the beamsplitter. Therefore the path lengths have to be equal within their coherence time, which implies that we know the creation time of the photons. As can be seen in Fig. 9.2, the photons subject to the Bell-state measurement originate from different entangled pairs. As SPDC is a spontaneous process, we have to ensure that variations in the creation time of the photons are smaller than their coherence time. The best way to do so is by limiting the interaction time of the pump laser with the PDC-crystal (BBO), which can be achieved by pulsing the pump laser¹. Choosing the right pulse length is an important task. Long pulses lead to less tight time correlations of the photons, however, as the laser pulse length gets shorter, the broader its spectral bandwidth becomes, eventually resulting in a shorter coherence time² of the photons and less pump power per pulse.

In practice, experiments have shown that the ideal trade-off is somewhere between 100-200 fs, depending on the central wavelength. For our purposes, we employ a mode-locked Ti:Sapphire laser, named Mira900aBasic, and operate it at a center wavelength³ of 789 nm (FWHM \approx 7.5 nm) and a pulse length of 150 fs. The Mira900aBasic is pumped by a 10 W, 532 nm solid state laser and produces an average output power of 1.3 W at a repetition rate of \sim 76 MHz, which corresponds to a temporal separation of 13 ns in between subsequent pulses.

¹One could, in principle, also use very thin PDC-crystal (on the order of microns) to limit the interaction time, however, such crystals have inaccurate phase matching conditions, produce low count rates or get easily damaged by powerful pump lasers.

²The coherence time is defined as the standard deviation of the fourier-transformed light-spectrum,

$$t_c = \frac{l_c}{c} = \frac{\sqrt{2 \ln 2}}{\pi} \frac{\lambda^2}{c \Delta \lambda_{\text{FWHM}}}.$$

³This is due to the fact that single photon detectors show high detection efficiencies at this wavelength, as will be discussed later.

9.2. Entanglement Source

Similar to the previous CSIGN-gate experiment, the near-infrared output of the Mira laser has to be up-converted to half the wavelength in order to allow for parametric down-conversion of the right wavelength. This is done by focusing with a 40 mm lens onto a nonlinear LBO-crystal (2 mm, lithium borate, LiB_3O_5), which is cut for type-I collinear second-harmonic generation (SHG). SHG converts a small fraction⁴ of the incident light, resulting in approximately 450 mW of 394.5 nm blue light. Due to the birefringence of the LBO-crystal, the up-converted beam profile is elliptical, which can be accounted for with the help of two cylindrical lenses, mounted perpendicular to each other. A Gaussian beam profile is essential for high-efficiency down-conversion [25, 37], and the right geometry of the pump light at the PDC-crystal can be verified in situ by a CCD-camera [59]. Four subsequent dichroic mirrors⁵, placed at 45° off normal incidence, separate the remaining fundamental 789 nm light from the desired UV-light and direct the pump laser onto the PDC-crystal.

We employ the “railway-cross”-scheme in the same manner as D. Bouwmeester *et al.* [52], where the ultraviolet pump is back-reflected after the first passage through the crystal, to produce entangled photon pairs in forward modes 1 and 2 and backward modes 3 and 4, which are subsequently prepared to be in the $|\Psi^-\rangle$ state with the help of HWPs and compensation crystals as discussed in Section 2.1.1 and shown in Fig. 9.2.

9.3. More Complete Bell-State Analyzer

Once the photons are properly prepared by the HWPs and compensation crystals, we select the desired frequency geometrically with so-called single-mode fiber couplers. The small numerical aperture⁶ of a single-mode fiber in combination with an achromatic microscope lens ($f=14$ mm) assures that only photons within a small angular distribution emitted along the vertices of the cones (shown in Fig. 2.1) are accepted by the fiber. The single-mode fibers only allow propagation of the Gaussian TEM_{00} mode and therefore serve as spatial mode filters.

The heart of the more complete Bell-state analyzer is the central 50/50 beamsplitter (see Fig. 8.2) which is realized as a fiber beamsplitter in our experiment. Fiber beamsplitters can basically be described as two bare single-mode optical fibers fused together such that they effectively form a 50/50 beamsplitter, i.e. the optical power is distributed evenly between the two output modes for every input mode.

⁴The up-conversion efficiency in our experiment averaged 25-30 %.

⁵Dichroic mirrors consist of a dielectric layer which, when placed at the right angle, perfectly reflect UV-light while most of the remaining near-infrared light is transmitted. Due to imperfections of the mirrors some UV-light will still leak through, which, together with the near-infrared, is used for spectral measurements and adjustment of the laser system.

⁶Single-mode fibers at 790 nm have a core diameter of approximately 5 μm .

9.3.1. Prerequisites for Quantum Interference

As already discussed at several points before, quantum interference can only take place when the participating photons are indistinguishable in every degree of freedom. As in the CSIGN-gate experiment, we use narrow spectral bandwidth filters (3.2 nm) to select PDC-photons of equal wavelength and to further stretch their coherence length to approximately $170 \mu\text{m}$, effectively longer than the pump pulse length. This also renders both entangled photon pairs indistinguishable in time, which is an important criterion for interfering photons from independent down-conversion processes, as was pointed out in Ref. [63]. An increase in coherence length is also desired when matching the photon paths to equal length (see Sections 2.2.1 and 4.1.3). The temporal delay between the photons can be varied by a delay mirror mounted on a motorized translation stage and its use will be discussed below. Single-mode fibers offer the benefit that the photons remain in a perfectly defined spatial mode allowing high-fidelity interference, but one has to take heightened care to match photons of equal polarizations at the fiber coupler. Since stress-induced and, in general, randomly distributed birefringence in optical fibers leads to rotations of the photon's polarization, one has to compensate for this by using so-called Polarization Controllers⁷, which deliberately squeeze and twist the fibers in a controllable way such that the unwanted rotations can be undone. The PolarITE-controller implements a tunable wave plate via an actuator (e.g. screw), which presses the fiber and induces birefringence. The strength of the birefringence can be controlled by turning the screw in or out, and the axis of the birefringence is adjusted by rotating the screw mount.

Polarization Compensation

To compensate for any fiber induced polarization distinguishability, we proceed as follows (see Fig. 9.1). The light of an 788 nm adjustment laser is split up with an additional fiber beamsplitter, sent through polarizers in each arm and directed to the single mode fibers, so that the beams recombine at the fiber beamsplitter of the BSA. This way, we effectively realize a Mach-Zehnder-Interferometer, and due to a Phase Modulator⁸ in one arm (see Fig. 9.2), intensity fluctuations of the interfering beams can be observed and measured with a LabView program. For the actual compensation procedure, the polarizers are aligned orthogonal to each other and the interference fringes are tuned to a minimum with the Polarization Controller. Polarization compensation has to be performed for both the H/V- and +/- -Basis (i.e. polarizers at $0^\circ/90^\circ$ and $45^\circ/-45^\circ$). Successful compensation in one basis does not automatically imply that the qubits (photons) are indistinguishable, since any point on the Poincaré-Sphere⁹ is defined by two angles θ and φ , as has already been discussed in Section 1.1.2. The compensation in the +/- -Basis is performed independently from the H/V-Basis by rotating a HWP in front of a QWP oriented at 45° , again in a way that the interference fringes are minimized.

⁷We use in-line PolarITE-controllers manufactured by General Photonics.

⁸The Phase Modulator is a piezo-actuator that periodically (70 Hz) squeezes the optical fiber, inducing and varying the phase of the interferometer.

⁹One might think of this polarization compensation procedure as trying to match the respective Poincaré-Spheres of the qubits such that they become indistinguishable.

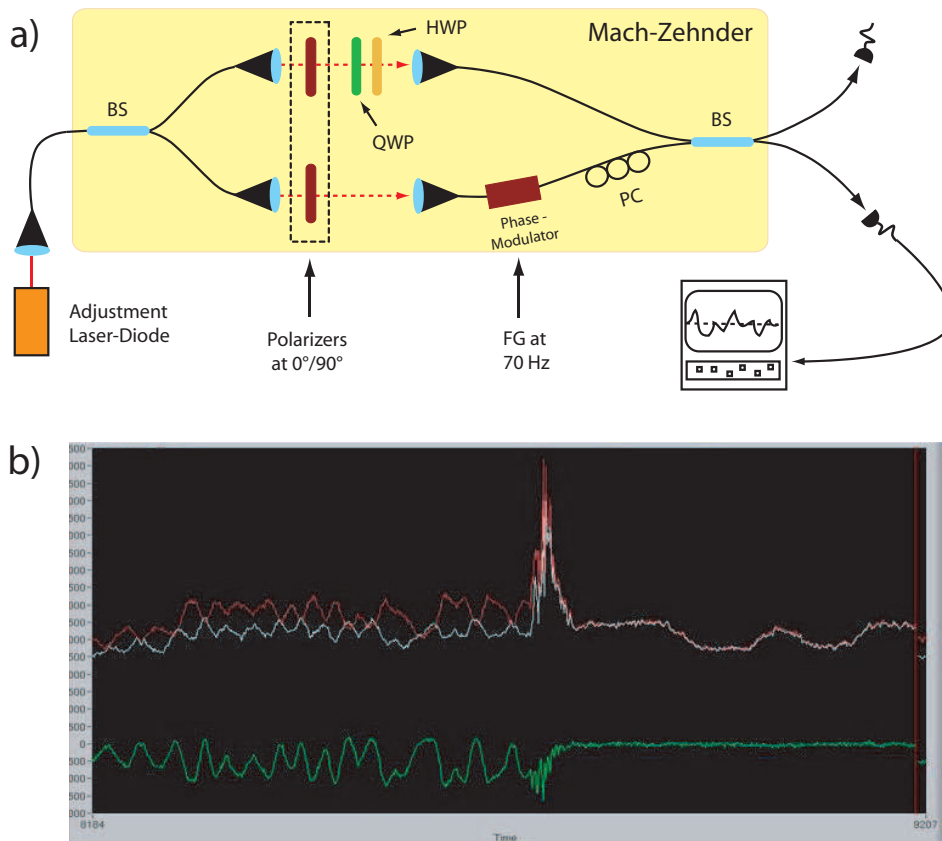


Figure 9.1.: Simplified scheme of the polarization compensation setup. The whole part left of the polarizers in **a)** can be removed from the actual setup since it serves for the compensation procedure only. The additional fiber BS realizes a Mach-Zehnder interferometer and the phase modulator allows the observation of interference fringes in one output detector. **b)** shows a typical fringe pattern of the procedure. The upper two lines give the actual count rates at the output-detectors while the lower line indicates the difference of these count rates. In the right part of the screen the interference fringes were optimized to a minimum using the polarization controller and crossed polarizers in front of the beamsplitter.

Eventually, the photons propagate to the more complete Bell-state analyzer (denoted Alice in Fig. 9.2), which consists of the (aforementioned) fiber beamsplitter and additional PBSs in the respective output modes. After the fiber beamsplitter, polarization drifts have to be compensated again to ensure that the photons are properly impinging on the Wollaston-PBS, which are of very high quality. These additional PBSs enable the further discrimination of the $|\Psi^+\rangle$ state, depending on proper coincidence detection, as has been described in the previous section (see Fig. 8.2).

9.4. Detection and Coincidence Logic

Silicon Avalanche Photo Diodes, or Si-APD for short, are most suitable for the detection of single photons at our selected wavelength of 789 nm because of their high quantum efficiency in this regime. When operated at -25 to -40°C, they achieve a typically overall detection efficiency of 40 %. The Si-APD very much resemble the detectors used in the CSIGN-gate experiment, but the single photon counting modules (SPCM) have been incorporated in self designed detector systems [60], which feature active quenching of the avalanche in the APD as well as air cooling in addition to the Peltier-cooling of the actual photo diode. The detector electronics of this APD directly deliver a 150 ns wide TTL pulse of 2.5 Volts height in a 50 Ω load. The detectors are fiber-coupled, have a dead time of about 200 ns and a quite low dark count rate of 200-500 cps.

In our experiment, the successful teleportation of a photon is indicated by, and conditioned on, a 4-fold coincidence measurement (participating photons 1-3 plus trigger), where the detectors at Alice determine the outcome of the Bell-state measurement as has been described in Section 8.2.2 and is illustrated in Fig. 8.2. For this task, a programmable coincidence logic has been designed by T. Jennewein [60], which is capable of detecting all possible coincidence patterns depending on the VHDL¹⁰ code written on the main logic chip (Xilinx CPLD¹¹ chip). The coincidence logic was realized as a very general and open hardware implementation of the CPLD in order to allow its use in several different experiments [60]. It has eight input BNC-connectors for detector signals, eight outputs delivering the desired coincidence pulses, two static selector signal inputs¹², and a clock signal input to synchronize the logic with the laser pulses.

Finally, the obtained coincidence signals are processed and counted by external counting cards and fed into a personal computer, where the measurement routines are realized as various LabView programs.

¹⁰VHDL = very high density hardware description language

¹¹CPLD = configurable programmable logic device

¹²The Selector allows to switch between different coincidence patterns, i.e. 4-folds, 2-folds and singles.

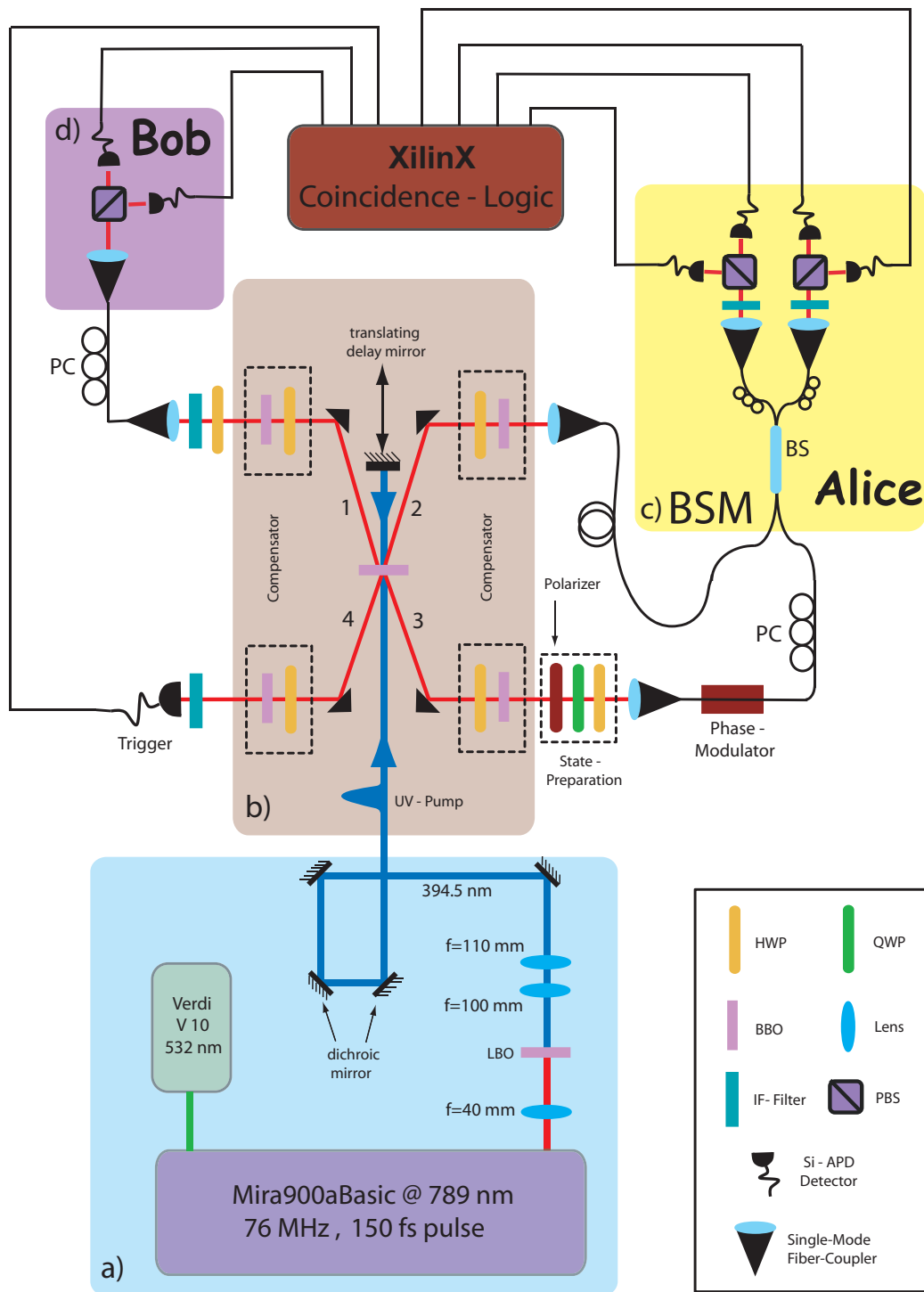


Figure 9.2.: Schematic drawing of the teleportation setup, which can be divided in three distinct parts. **a)** indicates the system that is pumping the PDC-crystal and includes the laser(s) and up-conversion process. **b)** represents the entanglement source, while boxes **c)** and **d)** display the communicating parties Alice and Bob, respectively. Photons 1 and 2 constitute the entangled pair that Alice and Bob share, while photon 3 indicates the particle to be teleported (photon 4 is the trigger). An more detailed description can be found in the respective sections.

10. The Mode-Mismatch Experiment

In this chapter I will explain the main realization of the presented experiment to study the effects of temporal mode-mismatch on the performance (i.e. fidelity) of a quantum teleportation experiment. We will accomplish this by deliberately moving the delay mirror during the teleportation, so that the overlap of the photon wavepackets at the relevant beamsplitter is non-ideal. This procedure also simulates fluctuations in fiber length, e.g. due to thermal expansion, as will occur in a real-world environment if these kind of configurations are about to be implemented in long-distance quantum communication schemes. Since we have already discussed the theoretical background of quantum teleportation and given a short outline of the experimental setup in the previous section, we can now focus on the experimental procedure. At the end of this chapter I will present the results and discuss their relevance.

10.1. Experimental Procedure

10.1.1. Optimizing the Entanglement Source

To be able to carry out the experiment in a reasonable way, we need an entangled photon source of high quality. While tweaking up the output power of the laser (without changing the wavelength) is a rather straight-forward task, obtaining good conversion- and collection-efficiencies of the parametric down-conversion as well as a high “entanglement visibility” is not. We are employing type-II SPDC [25] as already discussed in Section 2.1, so that we effectively create an entangled $|\Psi^-\rangle$ state in the forward and backward directions (i.e. modes 1/2 and 3/4, respectively) of the setup (Fig. 9.2). Walking the fiber couplers in the same manner as described in Section 4.1, we obtained coincidence rates as high as 12000 cps in the forward direction and 9000 cps in the backward direction, where

Polarizer Setting [°]	Forward Pair [CC/s]	Contrast	Backward Pair [CC/s]	Contrast
0/90	12000	200/1	9000	150/1
0/0	60		60	
45/-45	7000	35/1	6000	30/1
45/45	200		200	

Table 10.1.: Coincidence count rates per second ([CC/s]) of the forward and backward pair for various polarizer settings. The contrast gives a good estimate of the entanglement quality.

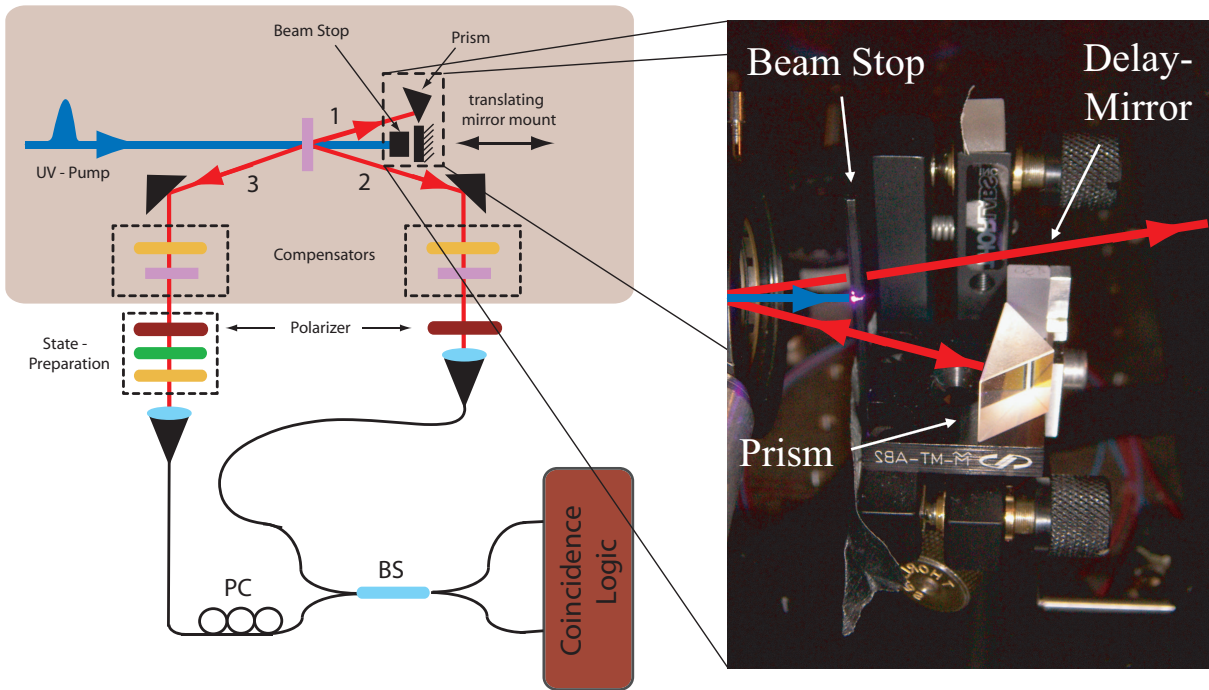


Figure 10.1.: Left: Scheme for equalizing the effective optical path lengths of photons 2 and 3. Right: Picture of the delay mirror mount. An additional prism is placed on the mount such that it back-reflects one of the forward DC-beams into mode 3. This way the correlated photons can be used to search for the optimal delay-mirror position where the path lengths of modes 2 and 3 become equal. This procedure is also known as *HOM-Dip* search and is further explained in the text.

those counts were measured in the H/V-Basis, i.e. with additional analyzing polarizers placed orthogonal to each other at $0/90^\circ$ in front of the fiber couplers. These counts decreased to values of 60 cps with parallel polarizers in front of the fiber couplers.

To obtain genuine entangled states, it is also necessary to achieve a good contrast in an orthogonal basis, such as the $+/-$ -Basis. By constantly checking those two visibilities and subsequently walking the fiber couplers, we were able to obtain fairly good contrasts, as can be seen in Table 10.1. It is important to note that the contrast in the complementary $+/-$ -Basis is always reduced due to the non-zero spectral width of the pump pulse¹, which leads to down-conversion photons of non-degenerate wavelength, as has been pointed out in Ref. [61, 62]. Calculations have shown that the optimum visibility in the complementary basis for our laser is approximately 97%.

¹This is due to the fact that the walk-off between the pump pulse and the down-conversion photons is never corrected for, which leads to a distinguishability of the pairs dependent on their production location in the crystal, which in turn reduces the interference and contrast between these different pairs.

10.1.2. HOM-Dip

In order to perform a successful Bell-state measurement, photons 2 and 3 have to be in the same spatial, spectral, polarization and temporal modes. Indistinguishability in the spectral and spatial mode is ensured by using fiber beam splitters and narrow (3.2 nm) interference filters (IF) in front of the detectors. To equalize the polarization of the photons before the BS, a polarization controller was employed, allowing for arbitrary polarization rotation of the qubit as has been explained in Section 9.3.1. Ultrashort laser pulses (150 fs) and narrow filtering stretch the coherence length of the photons to well above $300 \mu\text{m}$, effectively longer than the pump pulse duration [63]. Since we have to “erase” the identity of photons produced from independent DC-processes, this ensures indistinguishability of the respective creation times of the photons. In order to give rise to quantum interference at the BSA (i.e. the fiber beamsplitter), the two photons have to arrive simultaneously at the BS, i.e. well within their coherence time. By sufficiently delaying the pump pulse after the first passage through the non-linear crystal one can equalize the effective path lengths of photons 2 and 3 before they are superimposed on the fiber beamsplitter. In the actual teleportation experiment, these two photons originate from different and independent down-conversion processes. Unfortunately the event of a pump pulse generating two photon pairs, a so-called 4-fold-event, is rather unlikely (in the order of 1 Hz) so that the count rates remain too low for a straightforward teleportation scan. One has to previously narrow down on the region of perfect temporal overlap. This is done by blocking the pump laser shortly after it traverses the BBO-crystal, so that correlated photon pairs are only emitted in the forward direction (see Fig. 10.1). A prism mirror is then placed in the path of DC-photon 1, approximately at the height of the delay-mirror such that the down-converted light is back-reflected into mode 3 where it is fiber-coupled and directed to the fiber beamsplitter. Employing this method we achieve coincidence rates of up to 3500 cps, sufficient to perform a HOM-type experiment by slowly translating the delay mirror mount and simultaneously recording the coincidence rate between both outputs of the beamsplitter [29], as has been done in similar manner in Section 4.1.3. It is important to note at this point that we do not fiber-couple an entangled photon pair because of the polarizers².

The result of this preliminary scan can be seen in Fig. 10.2, where the Gaussian dip in coincidence rates at the output of the fiber beamsplitter clearly yields the ideal delay mirror position where the temporal mode match of the input photons is almost perfect. We observe a dip visibility³ of approximately 56 %. The full width-half maximum (FWHM) of the dip corresponds to the coherence length of the photons, in our case approximately $340 \mu\text{m}$ (twice the FWHM indicated in Fig. 10.2, since a mirror translation of x results in a actual path delay of $2x$). This preliminary HOM scan provides us with a good estimation of the region of teleportation. The imperfect dip visibility is probably due to non-ideal polarization compensation but not of further interest since we are just aiming for the ideal delay mirror position.

²An entangled $|\Psi^-\rangle$ state would not yield HOM dip, but rather a “HOM peak”!

³The *visibility* or “depth” of the dip is governed by the degree of indistinguishability between the photons and is therefore a good measure for the quality of the non-classical interference as outlined in Section 4.1.3.

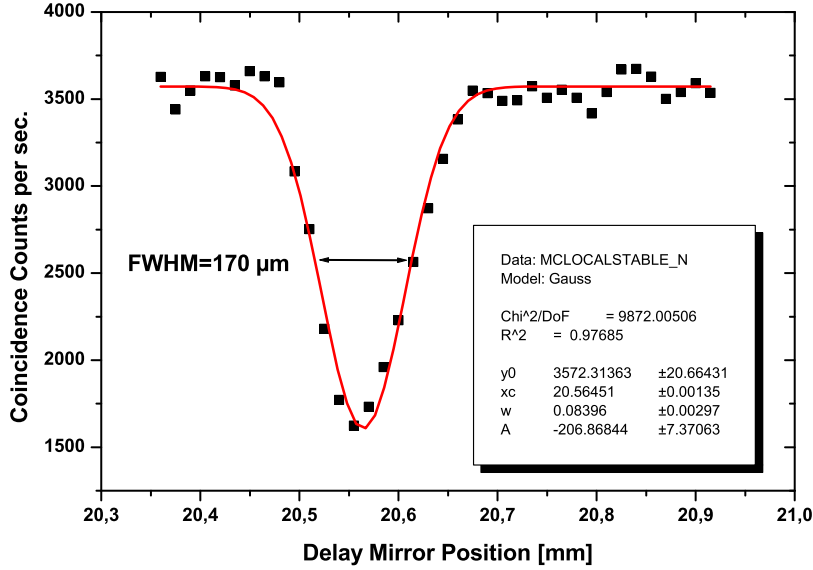


Figure 10.2.: Graphical plot of the HOM-Dip-Search. The significant dip in coincidence count rates indicates the position of ideal temporal overlap of the input photons at the beamsplitter. The dip is of Gaussian shape as indicated by the fit and yields a visibility of $56 \pm 3\%$.

10.2. Results

Theoretically, successful teleportation is indicated by a dip in threefold-coincidences, e.g. if we intend to teleport a $|+\rangle$ state, then the three-folds rate between the corresponding $|\Psi^-\rangle$ Bell-state detectors and the $|-\rangle$ analysis detector at Bob should decrease to zero, while the three-folds including the $|+\rangle$ analyzer remain constant when scanning over the region where the photons overlap coherently [52]. In the actual experiment, to eliminate the background of spurious counts, we also incorporate the trigger (photon 1) into our coincidence measurements. Furthermore, since we do not only detect the $|\Psi^-\rangle$, but also the $|\Psi^+\rangle$ state, we expect to observe a “peak” in coincidence rates for the $|+\rangle$ as well as for the appropriate $|-\rangle$ analyzer-three-folds. This is because outside the region of coherent photon overlap, the chance to observe one particular Bell-state decreases to $1/8$, compared to $1/4$ for ideal temporal overlap, resulting in the aforementioned relative peak of coincidence counts.

This can be seen in Fig. 10.3, where the coincidence rates are plotted as a function of the delay mirror position. We observe a visibility of $73 \pm 4\%$ and $79 \pm 3\%$ for the $|\Psi^-\rangle$ and $|\Psi^+\rangle$ state, respectively. In the region of the dip, the temporal delay between the arrival of photon 2 and 3 at Alice’s beamsplitter vanishes, resulting in quantum teleportation. To prove this for an arbitrary qubit, one has to demonstrate this for at

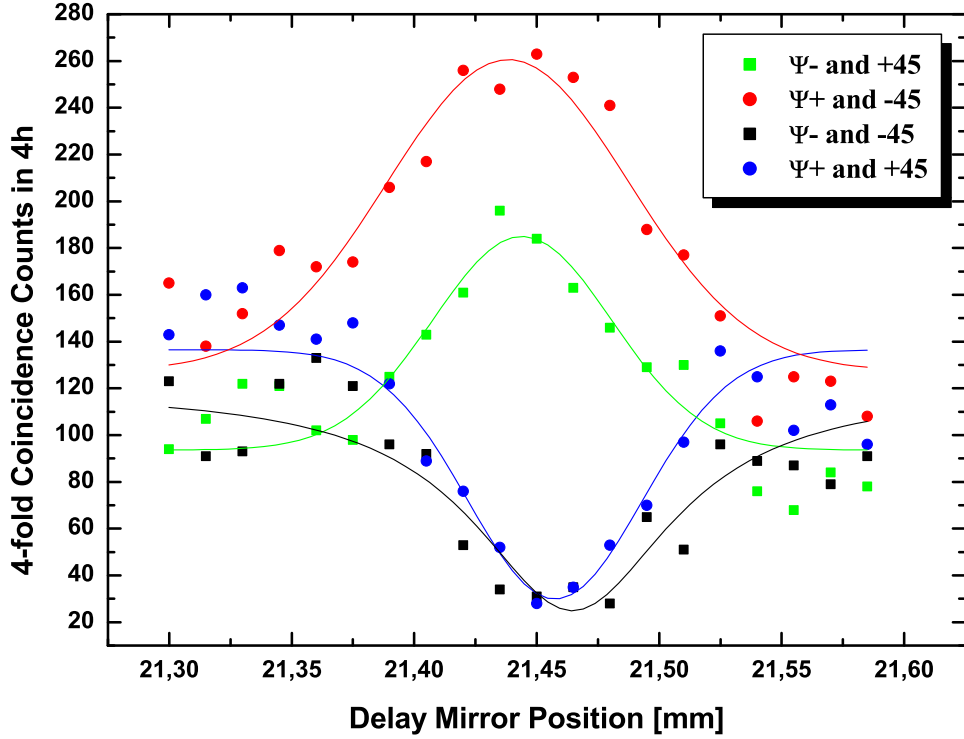


Figure 10.3.: *Experimental teleportation with a more complete Bell-state analyzer. The coincidence rates are plotted as function of the delay mirror position. We observe a Gaussian-fit visibility of $73 \pm 4\%$ and $79 \pm 3\%$ for the $|\Psi^-\rangle$ and $|\Psi^+\rangle$ state, respectively, which corresponds to a respective fidelity of $86 \pm 4\%$ and $90 \pm 3\%$.*

least two non-orthogonal states. Since we, however, are only interested in the impact of the temporal mode-mismatch on the teleportation fidelity, teleportation of other states has not been performed.

The fidelity F of the teleportation, which characterizes the overlap between the initial, to be teleported state, and the final, teleported state, is naturally affected by the (non-ideal) quality of the mode-match at the essential fiber-beamsplitter. By determining the visibility V of a full teleportation scan as shown in Fig. 10.3, we can easily compute the teleportation fidelity F via the following relation,

$$F = \frac{1 + V}{2}. \quad (10.1)$$

It has already been mentioned in the introductory part of Section 8.1, that variations⁴ in the length of optical fibers can easily lead to imperfect temporal mode matching

⁴e.g. due to temperature fluctuations, earth movements, etc.

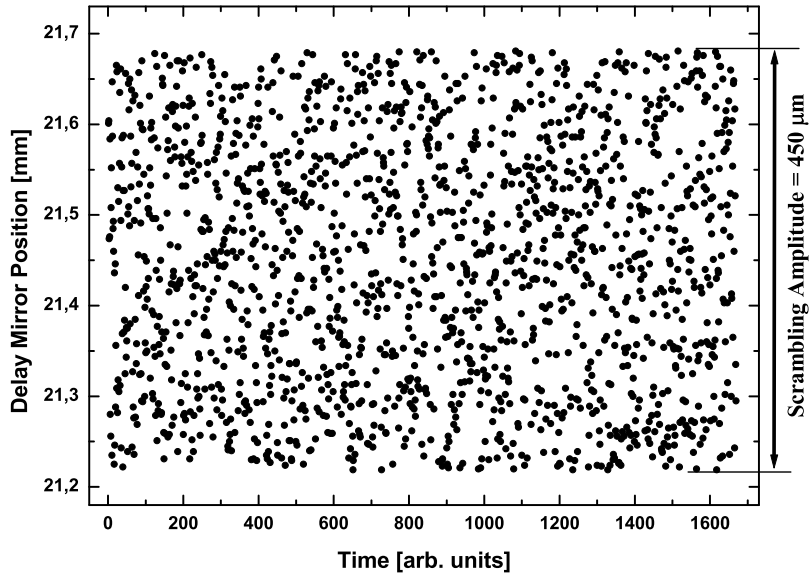


Figure 10.4.: Graphical representation of the delay mirror positions during a scrambling experiment, where the time scale is in arbitrary units. Obviously, the positions are rectangular and stochastically distributed over the full scrambling amplitude, which, in this particular case, was $450\ \mu\text{m}$. This plot indicates proper performance of the Random Number Generator.

conditions in quantum communication schemes, especially if the fibers are of several km length. To study effects of this sort in the laboratory, we chose to deliberately and randomly change the position of the delay mirror, delaying the arrival time of photon 3 which effectively simulates this temporal mismatch of the photons. Employing a LabView Random Number Generator to draw mirror positions uniformly from a preset (maximum) scrambling amplitude (see Fig. 10.4), we continuously translated the delay mirror during each measurement interval while performing a full teleportation scan. Repeating this procedure and increasing the maximum scrambling amplitude between each full scan, we were able to obtain plots as shown in Fig. 10.5, where the fidelity is plotted as a function of the maximum delay mirror movement (or scrambling) amplitude.

Fig. 10.5 shows the outcome of short and long range experiments, where the scrambling amplitude a has been chosen to vary in between 0 and 0.7 mm (left figure) and between 0 and 1.3 mm (right figure). The scrambling frequency was slightly above 1 Hz, which is the average expected 4-fold coincidence rate for our setup. To account for long-term power and alignment drifts of the pump laser, the 4-fold count rates have been divided by the according coincidence count rates of the more complete BSA. Furthermore, since we are only interested in the relationship between temporal mismatch and decrease in fidelity and actually do not care about the absolute values, the fidelity has been normalized to avoid possible misunderstandings.

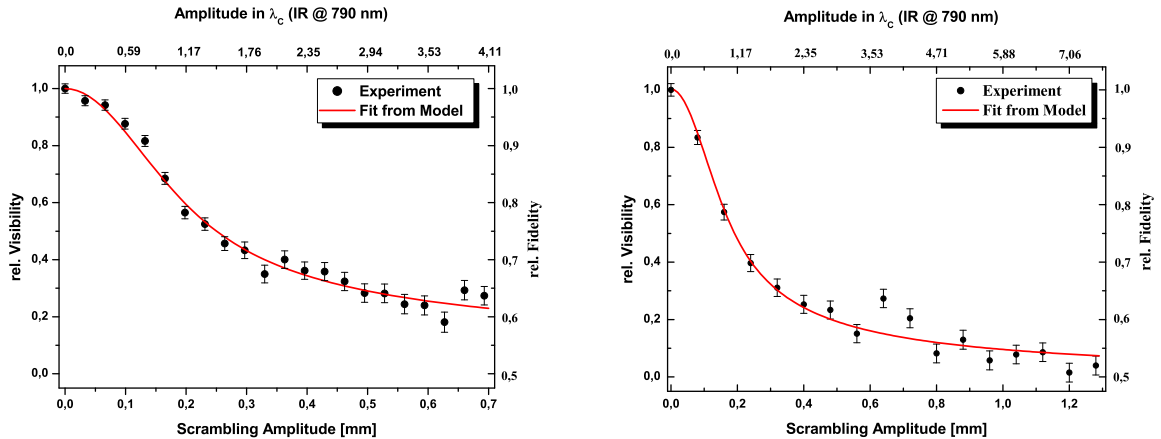


Figure 10.5.: The figures above show our experimental results plotting the teleportation fidelity as a function of the amplitude of the random delay mirror movement, in absolute values (mm) and also in units of the photon’s coherence length ($340/2=170\ \mu\text{m}$). The solid lines are fits developed from a theoretical model (see Section 10.3.1). Both, the short (left figure) and the long range (right figure) experiment show a very strong consistency with this model. Error bars have been calculated by Poissonian count statistics.

10.3. Discussion

The collected data of all experiments shows a characteristic Gaussian decrease in fidelity with increasing scrambling amplitude. But it is very interesting and well worth noting that mirror oscillations of up to $170\ \mu\text{m}$ amplitude still result in visibilities of roughly $\frac{2}{3}$, the quantum-classical threshold in teleportation [64]. This is equal to a temporal mode-mismatch of exactly the coherence length $\lambda_c=340\ \mu\text{m}$ of the photon (roughly 1.1 ps), which is proof of the fact that the participating photons have to overlap ONLY within their coherence length to give rise to quantum interference effects⁵. It also very dramatically shows that “phase coherence” between the photons originating from different PDC-events is not required for successful teleportation. This phase coherence is mandatory if one thinks of successful teleportation as just some Mach-Zehnder-type interference effect, where the interferometer is realized by the PDC-crystal and the BSA-beamsplitter. Since we frequently and randomly translate the delay mirror by well more than $500\ \lambda$ in the course of a measurement, we successfully disprove this argument.

It further has to be stated at this point that we employed two different types of delay-mirror-movements. One set of data was taken while continuously moving the mirror from one random position to the other, which also served the purpose to investigate the effects of temporal mismatch and to simulate temperature-induced fiber length fluctuations. Fol-

⁵This is also known as fourth-order interference, where it is said that each two-photon state interferes with itself, contrary to second-order interference, as realized in a typical Mach-Zehnder-interferometer, where it is said that each photon interferes with itself. Second-order interference therefore exhibits phase sensitivity, while in general, fourth-order interference does not [29].

lowing another approach and employing the highest motor velocity, we translated the mirror continuously in between the maximum scrambling positions. Moving the mirror mount as fast as possible ($\gg 200 \mu\text{m/s}$), we did not observe, on average, any deviations of the experimental results shown in Fig. 10.5.

In summary, this results, quite surprisingly, soften the requirements for future "real-world"-quantum repeaters or similar long-distance quantum communication schemes. Since polarization drifts in fibers are negligible over small timescales and can easily compensated for in the long run, these are very promising results for future engineers and possible commercial applications. The results further imply that temporal mode mis-match in the CSIGN-gate experiment is probably not to blame for imperfect gate performance, since relative fiber-length-drifts in this experiment are most likely in the sub-micron regime. If the criteria of spatial mode matching would be met with special partial polarizing fiber beamsplitters, gate performances with fidelities well above 99% could, in principle, be expected [65].

10.3.1. A Simple Theoretical Model

Additionally, in order to get a better theoretical comprehension, we developed a simple model which describes the Gaussian decrease in fidelity as a function of the temporal mis-match of the two interfering photons at the beamsplitter.

First of all, we assume the teleportation fidelity F to be a Gaussian function of the mirror position x with center $x_c = 0$ as indicated by experimental results and shown in Fig. 10.6.

$$F(x) = 0.5 + \frac{C}{w\sqrt{\pi/2}} \exp\left(-\frac{x^2}{2w^2}\right), \quad (10.2)$$

where C is a constant and w the width of the Gaussian. Since the actual position of the mirror is not constant during one measurement because of the deliberate random movements, one expects an average fidelity $\bar{F} = \frac{A(a)}{a}$, where a is the range of the fluctuations and $A(a)$ the integral

$$A(a) = \int_{-a/2}^{a/2} \frac{C}{w\sqrt{\pi/2}} \exp\left(-\frac{x^2}{2w^2}\right) dx, \quad (10.3)$$

which is also indicated in Fig. 10.6. This integral can be solved analytically to

$$A(a) = 2C \cdot \text{erf}\left(\frac{a}{2\sqrt{2}w}\right), \quad (10.4)$$

where $\text{erf}(z)$ denotes the error function

$$\text{erf}(z) = \frac{2}{\sqrt{\pi}} \int_0^z e^{-t^2} dt. \quad (10.5)$$

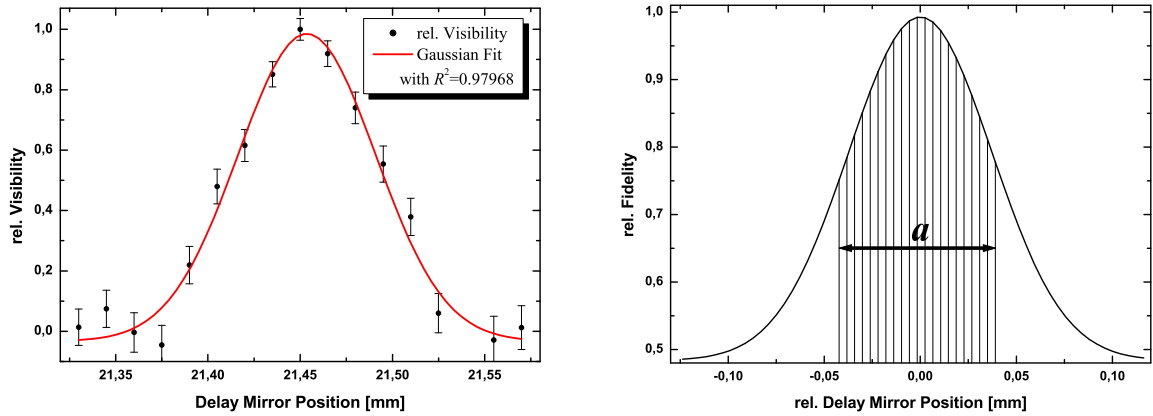


Figure 10.6.: Left figure: The dependence of the teleportation fidelity as a function of the unscrambled motor position. The fit indicates that the curve can be described by a Gaussian function with the FWHM ($170 \cdot 2 = 340 \mu\text{m}$) indicating the coherence length of the photons, in perfect agreement with the experimental results. We stress at this point that the width of the Gaussian was not a fit parameter.

Right figure: Calculating the expected, average teleportation fidelity in our experiment. a denotes the scrambling amplitude of the delay mirror, simulating the fiber-length-fluctuations.

The error function $\text{erf}(z)$ can be used whenever the results of a series of measurements are described by a normal distribution with standard deviation σ . Then $\text{erf}(z/(\sigma\sqrt{2}))$ is the probability that the error of a single measurement is in between $-z$ and $+z$. Eventually, the expected fidelity $\bar{F}(a)$ results to

$$A(a) = 2C \cdot \frac{\text{erf}\left(\frac{a}{2\sqrt{2}w}\right)}{a}. \quad (10.6)$$

But the parameters C and w describing the origin dependence of the Fidelity F from the mirror position x are in most cases unknown and $\bar{F}(a)$ must be fitted to the data set. To fit this function to a measurement series, one might use the following parametric fit function

$$\bar{F}(a) = P_1 \cdot \frac{P_2 \cdot \text{erf}(P_3 \cdot a)}{a}. \quad (10.7)$$

Here the parameter P_1 denotes the base level $\bar{F}(a)_{a \rightarrow +\infty}$, which in our case is 0.5. The parameter P_2 and P_3 depend on the constants C and w respectively, where C corresponds to the absolute maximum teleportation fidelity and w to the FWHM of the interference filters.

Collected data of all experiments agrees very well with this model, showing a Gaussian decrease in fidelity. The Gaussian fit in Fig. 10.5 is in fact not fitted to the data points but adapted and scaled from the model derived above. This parametric fit function is very well suited for mode-mismatch estimations in quantum communication schemes. If the constants C and w , i.e. initial fidelity and IF-filter specifications, are known, one can infer the sensitivity of the setup/configuration on temporal mode-mismatch.

11. Conclusion

In this concluding chapter I will briefly summarize the contents of this thesis and give a short overview of the experimental progress that has been achieved during my research activities.

I have given a somewhat extensive but self-contained introduction into the theoretical aspects regarding Quantum Information, starting with a short outline of quantum physics and linear optics quantum computation. This follows more detailed and advanced theory relevant for the experiments, such as phase-matching for parametric down-conversion and Gaussian beam propagation for the calculation of mode-matching and optimal fiber-coupling. Furthermore, the action of a simplified CSIGN-gate architecture for the generation of a 3-photon cluster state has been shown theoretically, while proper characterization of the gate's performance in the form of quantum state and quantum process tomography has also been explained.

In the main part of this thesis I have briefly described the experimental setup including the measurement equipment before proceeding to the experimental procedure, starting with the adjustment of the down-conversion source to generate correlated photons, to fiber-coupling the down-converted light and aligning and calibrating the linear optics elements employed in the setup. Last but not least, the quantum state and process tomography of the simplified CSIGN-gate has been performed, observing an average gate fidelity of $F_{avg} = 0.84 \pm 0.1$. I discuss this and other relevant results in detail and infer that mode-mismatch is primarily responsible for the gate's imperfect operation. At this point I want to stress again that the demonstration of this new architecture of an entangling optical gate is the simplest realization to date. Although unfortunately at the time being, the extension of the current setup to generate a 3-photon cluster state is not feasible due to low coincidence count rates, this problem has been addressed and various different solutions have been discussed. Necessary equipment therefore has been ordered and I believe that the generation of a 3-photon cluster state can be realized in the near future. A brief outlook on future experiments and their technical requirements is also given at this stage.

Since it turns out that mode-mismatch is the prime limitation on the performance of the CSIGN-gate, another experiment has been conducted that studies temporal mismatch of photons in a quantum teleportation configuration. After a brief introduction into quantum teleportation and more complete Bell-state analysis, I have described and explained the experimental setup and procedure. Results are presented and their relevance to various quantum communication schemes has been discussed. At the end

11. Conclusion

a simple theoretical model has been developed that fits very well to the experimental results, explaining the Gaussian decrease in teleportation fidelity with increasing temporal mode-mismatch of the photons at the essential Bell-state analyzer.

A. Published Work of this Thesis

The CSIGN-gate tomography, which has been presented in this thesis, was summarized as a publications and is given on the following pages. It has been recently published in Physical Review Letters and can also be accessed as an e-print on the **ArXiv** server: <http://arxiv.org/abs/quant-ph/0506262> .

Demonstration of a Simple Entangling Optical Gate and Its Use in Bell-State Analysis

N. K. Langford,^{1,2} T. J. Weinhold,^{1,2} R. Prevedel,^{1,2,3} K. J. Resch,² A. Gilchrist,^{1,2}
J. L. O’Brien,^{1,2} G. J. Pryde,^{1,2} and A. G. White^{1,2}

¹Centre for Quantum Computer Technology, University of Queensland, Brisbane QLD 4072, Australia

²Department of Physics, University of Queensland, Brisbane QLD 4072, Australia

³Institut für Experimentalphysik, Universität Wien, Boltzmannngasse 5, 1090 Vienna, Austria

(Received 30 June 2005; published 18 November 2005)

We demonstrate a new architecture for an optical entangling gate that is significantly simpler than previous realizations, using partially polarizing beam splitters so that only a *single* optical mode-matching condition is required. We demonstrate operation of a controlled-Z gate in both continuous-wave and pulsed regimes of operation, fully characterizing it in each case using quantum process tomography. We also demonstrate a fully resolving, nondeterministic optical Bell-state analyzer based on this controlled-Z gate. This new architecture is ideally suited to guided optics implementations of optical gates.

DOI: 10.1103/PhysRevLett.95.210504

PACS numbers: 03.67.Lx, 03.65.Wj, 03.67.Mn, 42.50.Dv

A key resource for using entanglement in quantum information protocols is gates that are capable of entangling or disentangling qubits [1]. Entangling gates lie at the heart of quantum computation protocols, for example, and disentangling gates used in Bell-state analyzers are required for quantum teleportation. Conceptually, the simplest such two-qubit gate is the controlled-Z (CZ) gate, which in the logical basis produces a π phase shift on the $|11\rangle$ term, (i.e., $|00\rangle \rightarrow |00\rangle$; $|01\rangle \rightarrow |01\rangle$; $|10\rangle \rightarrow |10\rangle$; $|11\rangle \rightarrow -|11\rangle$). This is a maximally entangling gate which, when coupled with single-qubit rotations, is universal for quantum computing [2].

In 2001, Knill, Laflamme, and Milburn proposed a scheme for linear optical quantum computing which used measurement to nondeterministically realize the optical nonlinearity required for two-qubit entangling gates [3]. They also showed that deterministic versions of these gates could be achieved using teleportation [4], which requires Bell-state measurement. Since then, there have been a number of demonstrations of quantum logic gates derived from this concept [5–9] and further theoretical development of linear-optics schemes [10–14]. In particular, there is a recent suggestion to use nondeterministic CZ gates to construct cluster states for demonstrating optical cluster-state quantum computation [15].

Here we report an experimental demonstration of a nondeterministic linear-optics CZ gate and its application as a Bell-state analyzer. This CZ gate is the simplest entangling (or disentangling) linear-optics gate realized to date, requiring only three partially polarizing beam splitters (PPBSs), two half-wave plates, no classical interferometers, and no ancilla photons. It is nondeterministic, and success is heralded by detection of a single photon in each of the outputs. We demonstrate the operation of this type of gate using photons generated both by continuous-wave (cw) and by femtosecond-pulsed parametric down-conversion—we find that temporal mode mismatch was not a significant factor in the gate’s performance. We fully characterize the operation in both regimes using quantum

process tomography, and we also demonstrate the use of this kind of gate for fully resolving Bell measurements. This simple entangling optical gate is promising for micro-optics or guided optics implementations where extremely good nonclassical interference is realizable.

The best performing entangling gate implementations to date have been interferometric: A conceptual schematic of an interferometric optical CZ gate, composed of three partially reflecting beam splitters with reflectivity $\eta = 1/3$, is shown in Fig. 1(a). Each polarization qubit input to the gate is split into two longitudinal spatial modes via a polarizing beam splitter. The horizontally polarized modes meet at a $1/3$ beam splitter, and nonclassical interference means that, for an arbitrary input state, the entire circuit performs

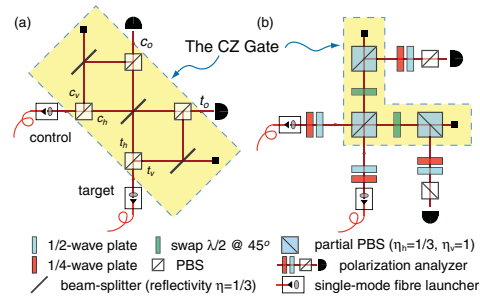


FIG. 1 (color). (a) Interferometric CZ gate based on the approach of Refs. [13,14]. Gate operation is enabled by transforming each qubit from polarization to spatial encoding and back again. This requires high interferometric stability and spatiotemporal mode matching for correct operation. (b) Partially polarizing beam splitter gate. The qubits can remain polarization encoded, since the vertically polarized modes are completely reflected by the first PPBS and do not interact. Nonclassical interference occurs between the horizontally polarized modes, with $\eta = 1/3$. The subsequent PPBSs give the required losses in the c_v and t_v modes as shown in (a).

the transformation: $\alpha|HH\rangle + \beta|HV\rangle + \gamma|VH\rangle + \delta|VV\rangle \rightarrow \frac{1}{3}[-\alpha|HH\rangle + \beta|HV\rangle + \gamma|VH\rangle + \delta|VV\rangle] + \dots$, where H and V refer to horizontal and vertical polarization, respectively, and the terms not shown correspond to the failure mode of the gate (i.e., the control and target output ports do not each contain one photon). With probability $1/9$, the circuit performs the CZ operation (using the logic-basis definitions $0 \equiv V$ and $1 \equiv H$). After the network of $1/3$ beam splitters, the two spatial modes of the control and target must be recombined to return to polarization-encoded qubits. Since the phase relationship between the logical modes must be maintained throughout this operation, interferometric stability is required between the control and target modes. Inherently stable interferometers have previously been used [6,7] to achieve this—however, these may not be suitable for scaling to large numbers in micro- or integrated-optical realizations. Here we take an alternative approach which does not require interferometric stability.

The experimental setup for the CZ gate we have developed is shown schematically in Fig. 1(b). We use PPBSs with reflectivities of $1/3$ and 1 for horizontally and vertically polarized light, respectively [16]. As in Fig. 1(a), only the H modes interfere nonclassically at the first PPBS. The V inputs are then flipped to H by half-wave plates—single-qubit X gates—and are attenuated by the remaining two PPBSs to balance the losses. The circuit of Fig. 1(b) therefore performs a CZ gate with additional X gates on the control and target qubits. These X gates could be corrected with wave plates in the outputs or by relabeling the logical states of the outputs—here we chose to relabel. The key advantage of the PPBS gate is that the polarization modes are never spatially separated and recombined, and, consequently, no classical interference conditions are required. A single nonclassical interference at the first PPBS is, therefore, the gate's sole mode-matching condition.

To test multiqubit circuits, multiphoton sources are required. The current gold standard for generating two or more photons is pulsed parametric down-conversion: Pump power densities far greater than those possible with cw sources lead to significantly higher probabilities of multiphoton events. Down-converted photons from short pump pulses can display more complex interference effects with reduced visibility. Thus, any new gate architecture should be shown to be compatible with both cw and pulsed sources. We tested the PPBS architecture with both cw and

femtosecond-pulsed sources, which produce pairs of energy degenerate single photons via spontaneous parametric down-conversion in a β -barium-borate crystal (Table I). The photon pairs were collected into single mode optical fibers to improve the spatial mode and injected into the CZ gate [Fig. 1(b)]. In the pulsed case, mode-matching was also improved by collecting the gate output into single mode fibers. A pair of half- and quarter-wave plates at the output of each fiber was used for input state preparation. A coincidence window of ~ 5 ns was used, and no correction for accidental counts was made. The gates were completely characterized via quantum process tomography [7,18].

A convenient representation of the measured process is the χ matrix, which is a complete and unique description of the process relative to a given basis of operators. The χ matrix for ideal CZ gate operation in the Pauli basis is shown in Fig. 2(a) (all the components are real). The experimental results for the cw gate are shown in Fig. 2(b), those for the pulsed gate in Fig. 2(c). By using the method of Ref. [7], we are guaranteed physical χ matrices requiring no extra normalization. In the cw case, the Π term is 0.36 instead of the expected 0.25 due to imperfect nonclassical interference resulting from mode mismatch.

Gate performances can be quantified by calculating the process fidelity $F_p = \text{Tr}[\chi_{\text{meas}}\chi_{\text{ideal}}]$ or the average gate fidelity, which is the fidelity between expected and actual output states, averaged over all pure inputs, $\bar{F} = (4F_p + 1)/5$ [7,19]. The cw and pulsed gates have process fidelities of $74.6 \pm 0.3\%$ and $84.0 \pm 0.1\%$, respectively, and average gate fidelities of $79.7 \pm 0.2\%$ and $87.2 \pm 0.1\%$, respectively [20]. Despite more stringent temporal mode-matching requirements in the pulsed regime, the extra spatial filtering led to better gate operation, equivalent to the previous best demonstration [7].

In our experiment, we observed systematic, fixed polarization rotations, probably due to birefringent effects in nonideal PPBSs. In practice, these have no effect on gate quality and, if necessary, could be compensated for with appropriate wave plates. To demonstrate this, we modeled their effect numerically, identifying single-qubit unitary corrections which increased the cw and pulsed process fidelities to $77.0 \pm 0.3\%$ and $86.6 \pm 0.2\%$, respectively, and average gate fidelities to $81.6 \pm 0.2\%$ and $89.3 \pm 0.1\%$, respectively.

A potential drawback of the PPBS architecture is that the beam splitting ratios are fixed at manufacture—in contrast to schemes where the setting of a half-wave plate determines the effective beam splitter reflectivity [6,7]. While the PPBSs for the cw gate (optimized for 702.2 nm) were measured to be within ± 0.01 of the required reflectivities, for the pulsed gate (820 nm), the values for the three PPBSs were $\eta = 0.28, 0.28, \text{ and } 0.29 (\pm 0.01)$; normalized to output power). Modeling a gate using 0.28 reflectivities, we find the optimum process fidelity that can be obtained is $F_p^{0.28} = 96\%$ —near ideal. As originally shown in

TABLE I. Photon source parameters.

Parameter	cw	Pulsed
Pump source	Ar ⁺	Doubled Ti:Sa
Pump wavelength	351.1 nm	410 nm
Crystal arrangement	Type I sandwich [17]	Type I single
Photon wavelength	702.2 nm	820 nm
Interference filters	± 0.18 nm	± 1.5 nm
Output state	Separable \leftrightarrow entangled	Separable

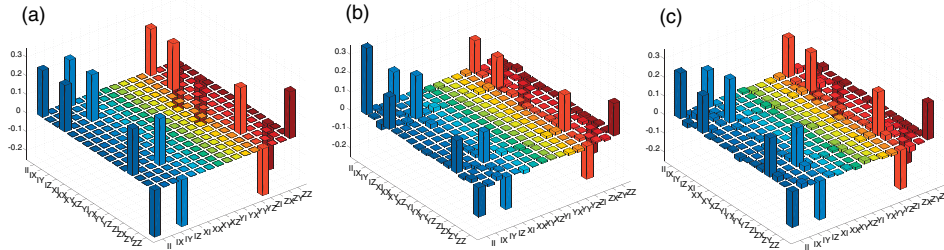


FIG. 2 (color). Quantum process tomography of the CZ gate. Real components of the χ matrix for the: (a) ideal, (b) cw, and (c) pulsed CZ gates. The imaginary components of the experimental matrices are not shown: A few elements are on the order of 0.05; the average is ~ 0.005 .

Ref. [13], the CZ gate is relatively forgiving of the exact splitting ratios, making it an eminently suitable gate to be realized with a PPBS architecture. Performance of the PPBS gates is limited almost exclusively by mode matching, primarily spatial, making these gates promising candidates for micro- or integrated-optical implementations, where nonclassical mode matching in excess of 99% can be expected [21].

We further test the CZ gate by operating it as a Bell-state analyzer of the entangled continuous-wave input states [17]. Because of the geometry of the source, and birefringence and geometric effects in the single mode fibers, the near-maximally entangled state produced is of the form $|HH\rangle + e^{i\varphi}|VV\rangle$. We use quantum state tomography

[22,23] to characterize the source state [Fig. 3(a)]. The tangle $T = 0.93 \pm 0.01$ and linear entropy $S_L = 0.05 \pm 0.01$ show that this state is highly entangled and highly pure; the fidelity with a maximally entangled state is $F = 98.0 \pm 0.4\%$. We determine that $\varphi = -2.094$ radians, and, by using the input wave plates [Fig. 1(b)] to perform appropriate single-qubit unitaries on each qubit, we can transform the state of Fig. 3(a) to any desired maximally entangled state of linear polarization. In Fig. 3(b), we have produced the state $|HH\rangle + |VV\rangle$ with fidelity $F_{\phi^+} = 96.1 \pm 0.2\%$; $T = 0.96 \pm 0.01$ and $S_L = 0.02 \pm 0.01$.

To quantify the performance of the CZ gate as a Bell-state analyzer, we produced the four maximally entangled states: $|\psi^{l\pm}\rangle = |HA\rangle \pm |VD\rangle$; $|\phi^{l\pm}\rangle = |HD\rangle \pm |VA\rangle$,

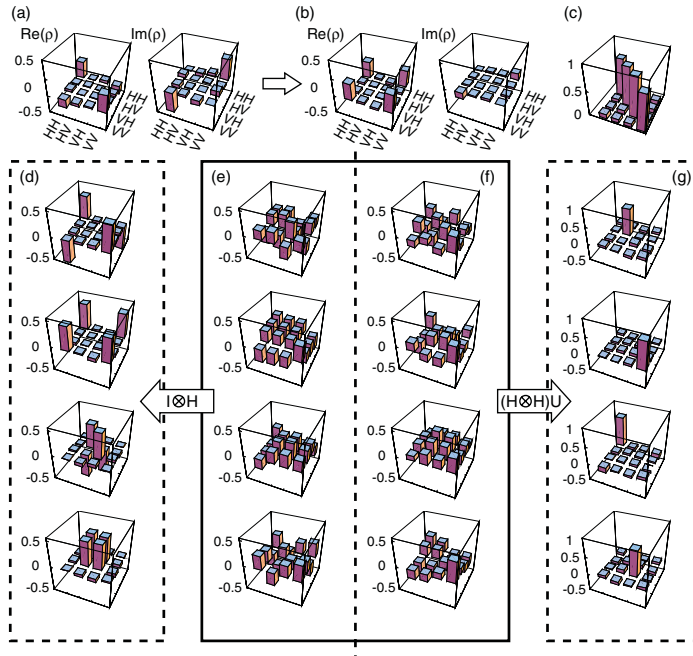


FIG. 3 (color). The CZ gate operating as a Bell-state analyzer. (a) The two-qubit entangled state at the output of the fibers and (b) transformed to the ϕ^+ Bell state. (c) The measured truth table: The average probability of success is 0.78 ± 0.03 . (d)–(g) Transformation of near-maximally entangled states to near-separable states by a CZ gate Bell-state analyzer. (d) The input Bell states determined from (e) the measured input states with the second qubit rotated by a Hadamard. (f) The measured output states, (g) transformed by applying local rotations to each qubit (see text).

where $D \equiv (|H\rangle + |V\rangle)/\sqrt{2}$ and $A \equiv (|H\rangle - |V\rangle)/\sqrt{2}$. These are just the usual four Bell states, with the second qubit rotated by a Hadamard so that they can be discriminated by the CZ gate. The four experimentally produced density matrices are shown in Fig. 3(e): The average of their fidelities is $\bar{F} = 95.8 \pm 0.7\%$; the average of the tangles and linear entropies are $\bar{T} = 0.94 \pm 0.02$ and $\bar{S}_L = 0.04 \pm 0.01$, respectively. For ease of visualization, we have numerically rotated these states into the more familiar form by applying a Hadamard gate to the second qubit [Fig. 3(d)].

An ideal CZ gate would take the four maximally entangled states $|\psi^{\pm}\rangle$, $|\phi^{\pm}\rangle$ to the four separable orthogonal states: $|DD\rangle$, $|AD\rangle$, $|DA\rangle$, and $|AA\rangle$, respectively. For the four input states in Fig. 3(e), the measured output density matrices are shown in Fig. 3(f). In fact, they are close to the four orthogonal separable states $(|H\rangle \pm e^{i\varphi_1}|V\rangle) \otimes (|H\rangle \pm e^{i\varphi_2}|V\rangle)$, where $\varphi_1 = -3.07$ and $\varphi_2 = 0.32$ as determined by a best fit. For ease of visualization, we have rotated these states into the logical basis in Fig. 3(g). The average of the fidelities between all combinations of the measured output states is $24 \pm 5\%$ (ideally zero), demonstrating that the states are close to orthogonal. Their average tangle $\bar{T} = 0.04 \pm 0.05$ and linear entropy $\bar{S}_L = 0.42 \pm 0.07$ indicate that they are unentangled, albeit somewhat mixed. This circuit is working quite well as a Bell-state analyzer.

The average fidelity of the measured output states with the above separable states is $F = 79 \pm 3\%$. If we analyzed the output of the circuit in this rotated basis, we would correctly identify the Bell state with a probability of 79%. More directly, we can measure each of the separable states for each Bell-state input by explicitly analyzing in the rotated basis, which gives the directly measured truth table for the CZ gate when operated as a Bell-state analyzer. The results are shown in Fig. 3(c), and the average probability of success is $78 \pm 3\%$, in agreement with the tomography results.

It is interesting to note that, whenever a postselected event occurs, the Bell measurement has effectively discriminated one of four input wave plate settings applied to a single input qubit. That is to say, 2 bits of classical information (representing the four wave plate settings) have been encoded into a single qubit. This is reminiscent of quantum dense coding [24–26], although, because the Bell measurement is nondeterministic, a protocol using this gate would be less efficient than ordinary classical communication. Nevertheless, this still demonstrates the power of entanglement for dense coding given a deterministic Bell analyzer, such as can be constructed, in principle, using measurement-induced nonlinearity.

In summary, we have proposed and demonstrated a new architecture for entangling optical gates. The key advantage of this new gate architecture is its simplicity and suitability for scaling—it requires only one nonclassical mode-matching condition and no classical interferometers. This is very promising for micro-optic and integrated-optic

realizations of this gate, where extremely good mode matching can be expected. Finally, we have demonstrated the operation of this gate as a Bell-state analyzer which has the advantage of higher success probability and no ancilla compared to alternative recent demonstrations [9,27].

This work was supported by the Australian Research Council (ARC), the Queensland Government, and the U.S. Advanced Research and Development Agency (ARDA). R.P. acknowledges support from the Austrian Science Foundation (FWF). We acknowledge Rohan Dalton for valuable discussions.

- [1] M.A. Nielsen and I.L. Chuang, *Quantum Computation and Quantum Information* (Cambridge University Press, Cambridge, England, 2000).
- [2] The more familiar CNOT gate is formed by applying a Hadamard gate H to the target qubit before and after a CZ gate.
- [3] E. Knill, R. Laflamme, and G.J. Milburn, *Nature (London)* **409**, 46 (2001).
- [4] D. Gottesman and I.L. Chuang, *Nature (London)* **402**, 390 (1999).
- [5] T.B. Pittman *et al.*, *Phys. Rev. A* **68**, 032316 (2003).
- [6] J.L. O'Brien *et al.*, *Nature (London)* **426**, 264 (2003).
- [7] J.L. O'Brien *et al.*, *Phys. Rev. Lett.* **93**, 080502 (2004).
- [8] S. Gasparoni *et al.*, *Phys. Rev. Lett.* **93**, 020504 (2004).
- [9] Z. Zhao *et al.*, *Phys. Rev. Lett.* **94**, 030501 (2005).
- [10] T.C. Ralph *et al.*, *Phys. Rev. A* **65**, 012314 (2002).
- [11] E. Knill, *Phys. Rev. A* **66**, 052306 (2002).
- [12] T.B. Pittman, B.C. Jacobs, and J.D. Franson, *Phys. Rev. Lett.* **88**, 257902 (2002).
- [13] T.C. Ralph *et al.*, *Phys. Rev. A* **65**, 062324 (2002).
- [14] H.F. Hofmann and S. Takeuchi, *Phys. Rev. A* **66**, 024308 (2002).
- [15] M.A. Nielsen, *Phys. Rev. Lett.* **93**, 040503 (2004).
- [16] The PPBSs are cube beam splitters with appropriately specified multilayered dielectric stacks purchased from Asahi Spectra (702.2 nm) and Special Optics (820 nm).
- [17] P.G. Kwiat *et al.*, *Phys. Rev. A* **60**, R773 (1999).
- [18] This involves inputting identical ensembles of 16 separable states into the circuit and performing a set of 36 measurements for each—36 measurements form an overcomplete set which increases accuracy.
- [19] A. Gilchrist, N.K. Langford, and M.A. Nielsen, *Phys. Rev. A* **71**, 062310 (2005).
- [20] The errors were estimated by doing a 1000 run Monte Carlo simulation of the whole process tomography analysis, with Poissonian noise added to the count statistics in each run.
- [21] T.B. Pittman and J.D. Franson, *Phys. Rev. Lett.* **90**, 240401 (2003).
- [22] A.G. White *et al.*, *Phys. Rev. Lett.* **83**, 3103 (1999).
- [23] D.F.V. James *et al.*, *Phys. Rev. A* **64**, 052312 (2001).
- [24] C.H. Bennett and S.J. Wiesner, *Phys. Rev. Lett.* **69**, 2881 (1992).
- [25] T. Schaetz *et al.*, *Phys. Rev. Lett.* **93**, 040505 (2004).
- [26] K. Mattle *et al.*, *Phys. Rev. Lett.* **76**, 4656 (1996).
- [27] P. Walther and A. Zeilinger, *Phys. Rev. A* **72**, 010302(R) (2005).

Bibliography

- [1] D. Bouwmeester, A. Ekert, A. Zeilinger (Eds.), “*The Physics of Quantum Information*”, Springer (2000) [1](#)
- [2] M.A. Nielsen and I.L. Chuang, “*Quantum Computation and Quantum Information*”, Cambridge University Press (2000) [1](#), [5](#), [13](#)
- [3] E. Schrödinger, “*Die gegenwärtige Situation in der Quantenmechanik*”, Naturwissenschaften **23**, 807, 823, 844 (1935) [3](#)
- [4] L.K. Grover, “*Quantum mechanics help in searching for a needle in the haystack*”, Phys. Rev. Lett. **79**, 325 (1997) [1](#), [13](#)
- [5] P.W. Shor, “*Algorithms for quantum computation: Discrete logarithms and factoring*”, Proc. 35th Annu. Symp. Foundations of Computer Science, IEEE Computer Society, Los Alamitos, CA, 1994, 124-134, Ed. S. Goldwasser [1](#), [13](#), [63](#)
- [6] E. Knill, R. LaFlamme and G.J. Milburn, “*A scheme for efficient quantum computation with linear optics*”, Nature **409**, 46 (2001) [1](#)
- [7] E. Knill, “*Quantum gates using linear optics and postselection*”, Phys. Rev. A **66**, 52306 (2002) [1](#)
- [8] T.C. Ralph, A.G. White, W.J. Munro and G.J. Milburn, “*Simple scheme for efficient linear optics quantum gates*”, Phys. Rev. A **65**, 12314 (2001) [1](#)
- [9] J.L. O’Brien, G.J. Pryde, A.G. White, T.C. Ralph and D. Branning, “*Demonstration of a all-optical quantum controlled-NOT gate*”, Nature **426**, 264 (2003) [1](#), [11](#), [28](#)
- [10] S. Gasparoni, J.-W. Pan, P. Walther, T. Rudolph and A. Zeilinger, “*Realization of a photonic controlled-NOT gate sufficient for quantum computation*”, Phys. Rev. Lett. **93**, 20504 (2004) [1](#), [11](#)
- [11] T.B. Pittman, B.C. Jacobs and J.D. Franson, “*Demonstration of nondeterministic quantum logic operations using linear optical elements*”, Phys. Rev. Lett. **88**, 257902 (2002) [1](#)
- [12] R. Raussendorf and H.J. Briegel, “*A one way quantum computer*”, Phys. Rev. Lett. **86**, 5188 (2001) [1](#), [12](#), [14](#)

- [13] P. Walther, K.J. Resch, T. Rudolph, E. Schenk, H. Weinfurter, V. Vedral, M. Aspelmeyer and A. Zeilinger, “*Experimental one way quantum computing*”, Nature **434**, 169 (2005) [2](#), [13](#), [14](#), [15](#)
- [14] T.C. Ralph, N.K. Langford, T.B. Bell and A.G. White, “*Linear optical controlled-NOT gate in the coincidence basis*”, Phys. Rev. A **65**, 62324 (2002) [i](#), [2](#), [61](#)
- [15] H.F. Hofmann and S. Takeuchi, “*Quantum phase gate for photonic qubits using only beam splitters and postselection*”, Phys. Rev. A **66**, 024308 (2002) [i](#), [2](#)
- [16] D. Greenberger, M. Horne and A. Zeilinger, in “*Bell’s Theorem, Quantum Theory, and Concepts of the Universe*”, editd by M. Kafetsios (Kluwer, 1989) [i](#), [2](#), [12](#), [29](#)
- [17] A.G. White, D.F.V. James, W.J. Munro and P.G. Kwiat, “*Exploring Hilbert space: Accurate characterization of quantum information*”, Phys. Rev. A **65**, 012301 (2001) [7](#)
- [18] W.K. Wootters, “*Entanglement of Formation of an arbitrary state of two qubits*”, Phys. Rev. Lett. **80**, 2245 (1998) [7](#)
- [19] T.C. Ralph, “*Scaling of multiple postselected quantum gates in optics*”, Phys. Rev. A **70**, 12312 (2004) [30](#)
- [20] A. Einstein, B. Podolsky and N. Rosen, “*Can quantum mechanical description of reality be considered complete?*”, Phys. Rev. **47**, 777 (1935) [6](#)
- [21] J.S. Bell, “*On the Einstein-Podolsky-Rosen paradox*”, Physics (Long Island City, N.Y.) **1**, 195 (1964) [6](#), [51](#)
- [22] S. Gulde *et al.*, “*Implementation of the Deutsch-Jozsa algorithm on an ion-trap quantum computer*”, Nature **421**, 48 (2003) [14](#)
- [23] L.M.K. Vandersypen *et al.*, “*Experimental realization of Shor’s quantum factoring algorithm using nuclear magnetic resonance*”, Nature **414**, 883 (2001) [13](#)
- [24] F. Schmidt-Kaler *et al.*, “*Realization of the Cirac-Zoller controlled-NOT quantum gate*”, Nature **422**, 408 (2003) [11](#)
- [25] P.G. Kwiat, K. Mattle, H. Weinfurter and A. Zeilinger, “*New high-intensity source of polarization-entangled photon pairs*”, Phys. Rev. Lett. **75**, 4337 (1995) [17](#), [20](#), [72](#), [77](#)
- [26] G. Weihs, “*Ein Experiment zum Test der Bellschen Ungleichung unter Einsteinscher Lokalität*”, PhD Thesis, University of Vienna (1998) [20](#)
- [27] E. Hecht and A. Zajac, “*Optics*”, Addison-Wesley (1974) [19](#)
- [28] A. Zeilinger, “*General properties of lossless beamsplitters in interferometry*”, Am. J. Phys. **49**, 882 (1981) [23](#)

-
- [29] C.K. Hong, Z.Y. Ou and L. Mandel, “*Measurement of subpicosecond time intervals between photons by interference*”, Phys. Rev. Lett. **59**, 2044 (1987) [24](#), [79](#), [83](#)
- [30] K. Sanaka, T. Jennewein, J.-W. Pan, K.J. Resch and A. Zeilinger, “*Experimental nonlinear sign shift for linear optics quantum computation*”, Phys. Rev. Lett. **92**, 17902 (2004) [28](#)
- [31] T.C. Ralph, IEEE J. Sel. Top. Quantum Electron. **9**, 1495 (2003) [30](#)
- [32] G.G. Stokes, Trans. Cambridge Philos. Soc. **9**, 399 (1852) [30](#), [48](#)
- [33] D.F.V. James, P.G. Kwiat, W.J. Munro and A.G. White, “*Measurements of qubits*”, Phys. Rev. A **64**, 52312 (2001) [31](#), [32](#), [51](#)
- [34] A.G. White, A. Gilchrist, G.J. Pryde, J.L. O’Brien, M.J. Bremner and N.K. Langford, “*Measuring controlled-NOT and two-qubit operation*”, [ArXiv:quant-ph/0308115](#) (2003) [33](#), [46](#), [51](#)
- [35] J.L. O’Brien, G.J. Pryde, A. Gilchrist, D.F.V. James, N.K. Langford, T.C. Ralph and A.G. White, “*Quantum process tomography of a controlled-NOT gate*”, Phys. Rev. Lett. **93**, 80502 (2004) [33](#), [44](#)
- [36] A.C. Doherty and A. Gilchrist, “*Quantum tomography using convex optimization*”, in preparation [33](#), [44](#), [51](#)
- [37] C. Kurtsiefer, M. Oberparleitner and H. Weinfurter, “*High-efficiency entangled photon pair collection in type-II parametric fluorescence*”, Phys. Rev. A **64**, 23802 (2001) [37](#), [39](#), [72](#)
- [38] C. Kurtsiefer, M. Oberparleitner and H. Weinfurter, “*Generation of correlated photon pairs in type-II parametric down conversion-revisited*”, J. Mod. Optics **48**, 1997 (2001) [20](#)
- [39] J. Emerson, Y.S. Weinstein, M. Saraceno, S. Lloyd and D.G. Cory, “*Pseudo-random unitary operators for quantum information processing*”, Science **302**, 2098 (2003) [54](#)
- [40] G. Svetlichny, “*Distinguishing three-body from two-body nonseparability by a Bell-like inequality*”, Phys. Rev. D **35**, 3036 (1987) [62](#)
- [41] P. Mitchell, S. Popescu and D. Roberts, “*Conditions for the confirmation for three-particle non-locality*”, Phys. Rev. A **70**, 060101 (2004) [62](#)
- [42] A.G. White, private communication (2005) [63](#)
- [43] T.B. Pittman and J.D. Franson, “*Violation of Bell’s inequality with photons from independent sources*”, Phys. Rev. Lett. **90**, 240401 (2003) [65](#)
- [44] P.P. Rohde, G.J. Pryde, J.L. O’Brien and T.C. Ralph, “*Quantum-gate characterization in an extended Hilbert space*”, Phys. Rev. A **72**, 032306 (2005) [65](#)

- [45] C.H. Bennett, G. Brassard, C. Crépeau, R. Jozsa, A. Peres and W.K. Wootters, “Teleporting an unknown quantum state via dual classical and Einstein-Podolsky-Rosen channels”, Phys. Rev. Lett. **70**, 1895 (1993) [2](#), [65](#), [66](#), [67](#)
- [46] P. Kok, C.P. Williams and J.P. Dowling, “Construction of a quantum repeater with linear optics”, Phys. Rev. A. **68**, 022301 (2003) [2](#), [65](#)
- [47] H.-J. Briegel, W. Dür, J.I. Cirac and P. Zoller, “Quantum Repeaters: The role of imperfect local operations in quantum communication”, Phys. Rev. Lett. **81**, 5932 (1998) [2](#), [65](#)
- [48] M. Zukowski, A. Zeilinger, M.A. Horne and A.K. Ekert, ““Event-ready-detectors” Bell experiment via entanglement swapping”, Phys. Rev. Lett. **71**, 4287 (1993) [65](#)
- [49] Z. Zhao, T. Yang, Y.-A. Zhen, A.-N. Zang and J.-W. Pan, “Experimental realization of entanglement concentration and a quantum repeater”, Phys. Rev. Lett. **90**, 207901 (2003) [2](#), [65](#)
- [50] K. Mattle, H. Weinfurter, P.G. Kwiat and A. Zeilinger, “Dense coding in experimental quantum communication”, Phys. Rev. Lett. **76**, 4656 (1996) [2](#), [65](#), [70](#)
- [51] W.K. Zurek and W.H. Wootters, “A single quantum cannot be cloned”, Nature **299**, 802 (1982) [66](#), [67](#)
- [52] D. Bouwmeester, J.-W. Pan, K. Mattle, M. Eibl, H. Weinfurter and A. Zeilinger, “Experimental quantum teleportation”, Nature **390**, 575 (1997) [2](#), [65](#), [68](#), [69](#), [72](#), [80](#)
- [53] J.-W. Pan, D. Bouwmeester, H. Weinfurter and A. Zeilinger, “Experimental entanglement swapping: entangling photons that never interacted”, Phys. Rev. Lett. **80**, 3891 (1998) [68](#)
- [54] D. Boschi, S. Branca, F. DeMartini, L. Hardy and S. Popescu, “Experimental realization of teleporting an unknown pure quantum state via dual classical and Einstein-Podolsky-Rosen channels”, Phys. Rev. Lett. **80**, 1121 (1998) [68](#)
- [55] J. Calsamiglia and N. Luetkenhaus, “Maximum efficiency of a linear-optical Bell-state analyzer”, Applied Physics B **72**,, 67 (2001) [68](#)
- [56] Y.-H. Kim, S.P. Kulik and Y. Shih, “Teleportation of a polarization state with a complete Bell-state measurement”, Phys. Rev. Lett. **86**, 1370 (2001) [68](#)
- [57] P. Walther and A. Zeilinger, “Experimental realization of a photonic Bell-state analyzer”, Phys. Rev. A **72**, 010302 (2005) [68](#)
- [58] R. Ursin, T. Jennewein, M. Aspelmeyer, R. Kaltenbaek, M. Lindenthal and A. Zeilinger, “Quantum teleportation link across the Danube”, Nature **430**, 849 (2004) [70](#)

-
- [59] R. Ursin, “*Quantenteleportation über lange Distanzen*”, PhD Thesis, University of Vienna (2005) [72](#)
- [60] T. Jennewein, “*Quantum communication and teleportation experiments using entangled photon pairs*”, PhD Thesis, University of Vienna (2002) [75](#)
- [61] K. Mattle, “*Nichtklassische Lichtzustände zur optischen Nachrichtenübertragung*”, PhD Thesis, University of Innsbruck (1997) [78](#)
- [62] G. Czeija, “*Verschränkung von Photonen aus intensiven Laserpulsen*”, Diploma Thesis, University of Vienna, (2001) [78](#)
- [63] M. Zukowski, A. Zeilinger and H. Weinfurter, “*Entangling photons radiated by independent pulsed sources*”, Annals of the N.Y. Acad. of Sciences **755**, 91 (1995) [73](#), [79](#)
- [64] S. Popescu, “*Bell’s inequalities versus teleportation: What is nonlocality?*”, Phys. Rev. Lett. **72**, 797 (1994) [83](#)
- [65] N.K. Langford, T.J. Weinhold, R. Prevedel, K.J. Resch, A. Gilchrist, J.L. O’Brien, G.J. Pryde and A.G. White, “*Demonstration of a simple entangling optical gate and its use in Bell-state analysis*”, Phys. Rev. Lett. **95**, 210504 (2005) [84](#)

Acknowledgements

Experimental physics is teamwork. This thesis would not have been possible without the help of many people. I guess this is the right time and place to express my acknowledgements to all those wonderful people who assisted and helped me in so many different ways during my time as a diploma candidate.

First of all, I would like to thank my supervisor in Vienna, Prof. Anton Zeilinger, not only for giving me the chance to write my diploma thesis in his group but also for his encouragement and generous support during my research stay in Australia.

I am also greatly indebted to my supervisor at the University of Queensland, Prof. Andrew White, for giving me the opportunity to come downunder to work and study in his very dynamic and modern research group.

Big thanks are also due to my co-workers Rupert Ursin and Felix Tiefenbacher, who introduced me into the Quantum Optics World and fortunately always kept my moral up and the “Schmäh” going in the lab.

I am also very thankful to Kevin Resch, who has been a very patient teacher when it came to explaining me the theoretical aspects of quantum computation, and with whom I thoroughly enjoyed working.

Till Weinhold, on whose experiment I have been working on in Brisbane, shall be thanked for good company in the lab and not to forget Nathan Langford and Alexei Gilchrist for the computational evaluation of the process tomography data. Geoff Pryde as well as Jeremy O’Brien, Philip Walther, Markus Arndt, Markus Aspelmeyer and Thomas Jennewein have contributed with helpful discussions and/or careful reading of the manuscript.

But most of all I am very grateful to my loving parents, Helmut and Waltraud, for their support, encouragement and for simply always being there for me. At this point, my sister Eva shall not be missed, and I like to thank her for always cheering me up and providing me with generous advice in all aspects of my life.

Finally, I want to thank my girlfriend Evi for her love, understanding and patience during so many hours at the University and especially during my research stay in Australia.

Robert Prevedel